General Disclaimer

One or more of the Following Statements may affect this Document

- This document has been reproduced from the best copy furnished by the organizational source. It is being released in the interest of making available as much information as possible.

- This document may contain data, which exceeds the sheet parameters. It was furnished in this condition by the organizational source and is the best copy available.

- This document may contain tone-on-tone or color graphs, charts and/or pictures, which have been reproduced in black and white.

- This document is paginated as submitted by the original source.

- Portions of this document are not fully legible due to the historical nature of some of the material. However, it is the best reproduction available from the original submission.

Produced by the NASA Center for Aerospace Information (CASI)

NASA Grant NSG-1391

A HIGH ORDER ACCURATE FINITE ELEMENT ALGORITHM FOR HIGH REYNOLDS NUMBER FLOW PREDICTION

(NASA-CR-157309) A HIGH ORDER ACCURATE FINITE ELEMENT ALGORITHM FOR HIGH REYNOLDS NUMBER FLOW PREDICTION Final Technical Report (Tennessee Univ.) 106 p HC A06/MF A01 CSCL 20D G3/34

N78-27368

Unclas 25889

FINAL TECHNICAL REPORT

PREPARED FOR

NATIONAL AERONAUTICS AND SPACE ADMINISTRATION

LANGLEY RESEARCH CENTER
HAMPTON, VIRGINIA 23665

BY

UNIVERSITY OF TENNESSEE

DEPARTMENT OF ENGINEERING SCIENCE AND MECHANICS
KNOXVILLE, TENNESSEE 37916

AUG 1978
RECEIVED
NASA STI FACILITY

June 16, 1978

Dr. Allen J. Baker
Principal Investigator

ABSTRACT

A Galerkin-Weighted Residuals formulation is employed to establish an implicit finite element solution algorithm for generally non-linear initial-boundary value problems. Solution accuracy, and convergence rate with discretization refinement, are quantized in several error norms, by a systematic study of numerical solutions to several non-linear parabolic and a hyperbolic partial differential equation characteristic of the equations governing fluid flows. Solutions are generated using selective linear, quadratic and cubic basis functions. Richardson extrapolation is employed to generate a higher-order accurate solution to facilitate isolation of truncation error in all norms. Extension of the mathematical theory underlying accuracy and convergence concepts for linear elliptic equations is predicted for equations characteristic of laminar and turbulent fluid flows at non-modest Reynolds number. The non-diagonal initial-value matrix structure introduced by the finite element theory is determined intrinsic to improved solution accuracy and convergence. As an alternative to the conventional multi-dimensional finite element algorithm, a factored Jacobian iteration algorithm is derived and evaluated to yield a consequential reduction in both computer storage and execution CPU requirements while retaining solution accuracy. The developed hypermatrix statement of the solution algorithm reduces storage requirements and facilitates direct inclusion of parameter variations. The results of the research conducted under the Grant and reported herein document an accurate and versatile algorithm potentially applicable to solution of a wide range of practical problem classes in aerodynamics and fluid mechanics.

INTRODUCTION AND SUMMARY

The primary objective of this research project is to assess prediction of extension of the mathematical theory governing accuracy and convergence character of finite element solution of linear elliptic partial differential equations, to the progressively more complex hyperbolic and non-linear parabolic partial differential equations characteristic of fluid mechanics. The results for the non-linear laminar and turbulent flow cases, considered and reported herein, predict that extension of the linear equation theory is valid for the finite element solution algorithm using linear, quadratic and cubic elements. Comparison tests between the finite element and a finite difference (Crank-Nicholson) algorithm have quantized for the first time the differences in numerical accuracy attainable. These comparison results generally confirm that the linear finite element solution algorithm is consistently superior to the equal order accurate Crank-Nicholson algorithm in terms of accuracy and convergence, while maintaining comparable solution economy, for the non-linear parabolic equations considered. The reported results of the tightly controlled numerical experiments confirm viability of the energy norm as the intrinsic measure for accuracy and convergence determination in laminar and turbulent parabolic-type flowfield prediction. This is in significant distinction to the variability in convergence measured in the various common engineering norms.

A range of practically useful finite element discretizations for parabolic flow prediction has been observed. Solutions employing coarse grid linear finite element discretizations generally display accuracy superior to those predicted by strict adherence to the convergence curve. Conversely, those solutions obtained with quadratic finite elements typically

display coarse grid inaccuracy. On the other hand, on progressively refined discretizations, sources of error other than that associated with finite element discretization serve to obliterate the refined solution accuracy theoretically obtainable. The absolute error associated with solutions obtained employing quadratic elements is, however, uniformly smaller than that associated with linear element solutions on sufficiently refined grids. The accuracy obtainable using a non-uniform grid within the finite element algorithm was found to be superior to use of uniform grids for the parabolic problems studied. This is not uniformly true, however, for the finite difference algorithm evaluated. Furthermore, while non-uniform discretizations display better absolute error for both the linear and quadratic finite element algorithms, the presence of an optimum-accuracy grid was detected for linear element solutions, but was absent for quadratic element solutions.

The use of non-zero pressure gradients for the laminar parabolic flows did not measurably alter the level of accuracy or convergence character, measured in the energy norm, of the linear finite element algorithm. This was not the case, however, for the quadratic finite element algorithm, where the fourth order accuracy of the algorithm for zero pressure gradient was degraded to second order for the cases involving non-zero pressure gradient. This may be due in part to the alteration in the convergence character, from oscillatory for zero pressure gradient, to monotonic for the non-zero pressure gradient cases. Computation of the transverse velocity distribution, using generally second order finite difference formulae, yields a significant source of error in actual computations on fine grids, which adversely affects the accuracy attainable using higher order accurate finite element interpolations. The level of error, capable of quantization, increased from 10^{-5} to about 10^{-6}, when the non-linearly induced error, stemming from the transverse velocity solution methodology, was removed. Hence, while transverse velocity

constitutes data within the theoretical framework of the algorithm, a uniformly fourth-order accurate algorithm would be required to increase solution accuracy beyond about 10^{-5}. The results of the turbulent boundary layer solutions indicate that a strictly-accurate evaluation of the Jacobian, within the Newton iteration algorithm, is not necessary to achieve an adequately-accurate engineering solution. Significant solution economics can result, therefore, in terms of computer core and CPU, by taking advantage of the versatility embedded within the developed modified Newton iteration algorithm for multiple dependent variable systems.

The transient continuity equation solutions confirmed that, on all comparison bases, the performance of the implicit finite element algorithmic solution form for a dominantly hyperbolic equation, is superior to the equivalent-complexity finite difference form with no additional computational effort. The primary objective with the conducted numerical experiments was to evaluate economy measures applicable to the basic finite element formulation, and to assess their influence on determined accuracy and convergence. The developed factored Jacobian integration algorithm displayed considerable economy in terms of computer storage and CPU, in comparison to the conventional multi-dimensional finite element algorithm, with no measurable loss in accuracy. Accuracy and convergence properties of the factored algorithm have been quantized, and the several numerical solutions obtained for a variety of velocity fields document accuracy and computational aspects and illustrate its versatility.

THEORETICAL ANALYSIS

Accuracy and Convergence

In finite element analysis, error estimates and convergence properties are typically expressed in an energy norm, cf. Strang and Fix (1973).

Alternatively, for finite differences, a stability analysis is employed to ascertain that the method is convergent, and a local truncation error analysis determines order-of-accuracy by means of a Taylor series expansion. Error and convergence may also be measured in other norms including the familiar engineering parameters. For the case of boundary layer solutions, for example, these could include the integral parameters of boundary layer displacement and momentum thickness, shape factor, and skin friction coefficient.

The primary focus of this reported analysis is numerical determination of the accuracy and convergence character of a finite element numerical solution algorithm for representative initial-value problems associated with high Reynolds number laminar, turbulent, and inviscid flows. A companion focus is evaluation of error measurement norms that facilitate estimation of contributing factors to solution inaccuracy, hence solution economy. The question of accuracy of a finite element (or any other numerical) solution requires quantization with reference to acceptable (usable and efficient) interpolation functions and mesh size distributions. The mathematical theory of finite elements, which examines these details in thoroughness, is generally limited to linear partial differential equations. The present requirement is to recall the fundamental theoretical concepts as applied to elliptic equations, and to present the extension to accuracy and convergence measure for the hyperbolic and non-linear parabolic equations of interest.

The point of departure, cf. Strang and Fix (1973), is the linear differential equation on one dimensional space R^1

$$L(q) = \nu \frac{\partial^{2m} q}{\partial x^{2m}} + g = 0 \qquad (1)$$

where ν is a general (constant) diffusion coefficient, and g is a source

term. The boundary conditions are typically assumed homogeneous as

$$q(\bar{x},t) = 0 \tag{2}$$

To establish the error measure for the finite element solution of equation (1) for $m=1$, which corresponds to elliptic, the fundamental requirement is determination of how close the finite element solution q^*

$$q^* \equiv \sum_{e=1}^{M} q_e = \sum_{e=1}^{M} \{N_k(x)\}^T \{Q\}_e \tag{3}$$

is to the true solution $q(x)$. The fundamental theorem states that the finite element solution lies as close as possible to the exact solution, in the sense that the energy in the error, ε

$$\varepsilon \equiv q - q^* \tag{4}$$

is minimized. The minimum energy functional that is the equivalent to minimization of the variational statement for equations (1)-(2) is

$$I(q,q) = \int_{R^1} \left[\frac{1}{2}\nu \left(\frac{\partial q}{\partial x}\right)^2 - gq\right] dx \tag{5}$$

The energy inner product for equation (1) is defined as

$$E(q,q) = \int_{R^1} \frac{1}{2}\nu \left(\frac{\partial q}{\partial x}\right)^2 dx \tag{6}$$

The proof of the fundamental theorem, cf. Strang and Fix (1973), pp. 39-41, assures that the energy in the error is minimized by the finite element solution of equation (1) obtained using equation (3). Hence, the error in the energy inner product, equation (6), for the finite element solution, equation (3), satisfies the inequality

$$E(\varepsilon,\varepsilon) \equiv \|q-q_e, q-q_e\| \leq C_1 \Delta_e^{2(k+1-m)} \|q\|_\alpha^2 \tag{7}$$

where C_1 is a constant independent of Δ_e, the measure of the largest finite element on R^1, the exponent of Δ_e is a function of the largest complete polynomial degree k in equation (3), $2m = 2$ is the order of the elliptic operator, equation (1), and $\alpha = k + 1$ is related to the required smoothness of the solution.

Equation (7) states that the error in the energy inner product of the finite element algorithm, using a linear interpolation polynomial for example, goes to zero as the order Δ_e^2 (or more conventionally in finite difference terminology, h^2, i.e., the method is second-order accurate). The error bound in equation (7) can be refined, for $m = 1$ and $k = 1$ for example, as

$$\begin{aligned} E(\varepsilon,\varepsilon) &\leq C_2 \Delta_e^2 \|q^{\sim}\|^2 \\ &\leq C_3 \Delta_e^2 \|F\|^2 \end{aligned} \tag{8}$$

where C_2 and C_3 are constants, Δ_e is the measure of the largest finite element, and $\|F\|$ is the L_2 norm of the data of the problem specification, i.e.,

$$\|F\| = \left[\int g^2 dx\right]^{\frac{1}{2}} \tag{9}$$

Equation (9) states that the error in the energy of the linear finite element approximation to the true solution q decreases in proportion to the square of the measure of the largest finite element, and that the error depends continuously on the data of the problem specification. Hence, as a consequence of the fundamental theorem, the finite element solution converges in the energy norm as

$$E(\varepsilon,\varepsilon) \rightarrow 0 \quad \text{as} \quad \Delta_e \rightarrow 0 \tag{10}$$

For the class of time-dependent and/or initial-value problems of interest, extension of equation (1) to a linear, elliptic, initial-value equation statement yields

$$L(q) = \frac{\partial}{\partial t} q(x,t) + \nu \frac{\partial^{2m}}{\partial x^{2m}} q(x,t) + g(x,t) = 0 \tag{11}$$

with boundary conditions

$$q(\bar{x},t) = 0 \tag{12}$$

and an initial condition

$$q(x,0) = q_0(x) \tag{13}$$

Oden and Reddy (1976) develop error estimates for fully discrete Galerkin approximation of an equation of the form (11). The components of the approximate solution scheme are defined as: $q(x,t)$, the exact solution of equation (11); $Q(x,t)$, the solution to the semidiscrete (continuous dependence on time, t, is still assumed) Galerkin approximation; and $q^*(x)$, the solution to the finite-difference Galerkin approximation at time $t = n\Delta t$. The following definitions for error are then introduced:

$$\begin{aligned} \varepsilon(x,n\Delta t) &= q(x,n\Delta t) - q^*(x) && = \text{approximation error} \\ \sigma(x,n\Delta t) &= q(x,n\Delta t) - Q(x,n\Delta t) && = \text{semidiscrete approximation error} \\ \tau(x,n\Delta t) &= Q(x,n\Delta t) - q^*(x) && = \text{temporal approximation error} \end{aligned} \tag{14}$$

For any choice of norm

$$\|\varepsilon(t)\| = \|\sigma + \tau\| \leq \|\sigma\| + \|\tau\| \tag{15}$$

For use of a forward difference integration algorithm, Oden and Reddy (1976) prove that if the components of the error are given by equation (14), then for a linear, elliptic, initial-value equation, the error satisfies the inequality

$$\|\varepsilon(n\Delta t)\| \leq C_1\Delta_e^{2(k+1-m)}\|q(n\Delta t)\| + C_5\Delta t\|Q^0\|_m \tag{16}$$

Here, the first term on the right hand side of equation (16) is the right hand side in the inequality (7). Furthermore, C_5 is a constant, Δt is the time step, and $\|Q^0\|_m$ is the norm of the initial data.

For the second case of interest, consider a first order hyperbolic problem statement of the form

$$L(q) = \frac{\partial q}{\partial t} + \nu\frac{\partial q}{\partial x} = 0 \tag{17}$$

with initial condition

$$q(0) = q_o \tag{18}$$

Here again, for use of a forward difference integration algorithm, Oden and Reddy (1976) prove that if the components of the error are given by equation (14), then for a linear hyperbolic equation, the error satisfies the inequality

$$\|\varepsilon(n\Delta t)\| \leq C_1\Delta_e^{k+1}\|q\|_{k+1} + C_5\Delta t\|Q^0\| + C_6\Delta_e\int_0^{n\Delta t}\|q\|_{k+1}dt \tag{19}$$

where C_6 is another constant. Unfortunately, no similar analyses for an initial-value, non-linear problem exists, which prompts the numerical experiment approach taken herein to study the convergence character of finite element solution of non-linear initial-value problems.

Error Analysis

The main emphasis in this analysis is assessment of the discretization error associated with use of the finite element solution procedure for non-linear problems. For such problems, the approach taken is evaluation of absolute accuracy as determined by computed solution comparisons, for

progressively refined discretizations, in the energy norm, to establish the convergence rate exponent on Δ_e. Since the fluid mechanics equations to be solved correspond to statements of conservation, correspondingly defined norms are also useful, in particular

$$p_1 = \sum_e \int_{R_e^n} q_e d\tau \tag{20}$$

$$p_2 = \frac{1}{2} \sum_e \int_{R_e^n} q_e^2 d\tau \tag{21}$$

The familiar engineering parameters useful for quantizing flow phenomena can typically be constructed from the energy and p-norms. For example, in boundary layer flow, shape factor and skin friction are parameters of great engineering significance in assessing solution acceptability, i.e., accuracy. Shape factor H is defined as

$$H \equiv \delta^* \theta^{-1} \tag{22}$$

where δ^* is the boundary layer displacement thickness and θ is the momentum thickness defined as

$$\delta^* \equiv \int_\delta [1 - \tilde{u} u_I^{-1}] dx_2 \tag{23}$$

$$\theta \equiv \int_\delta \tilde{u}_1 u_I^{-1} [1 - \tilde{u}_1 u_I^{-1}] dx_2 \tag{24}$$

where u_I is the local inviscid freestream velocity, and $\tilde{u}$ is the (time-averaged) boundary layer velocity distribution. Assuming $\tilde{u}$ non-dimensionalized by u_I, and for δ spanning $\cup R_e^1 = R^1$, using equations (20)-(21) in the discrete approximation to equations (23)-(24) yields

$$\delta^* = \delta - p_1 \tag{25}$$

$$\theta = p_1 - 2p_2 \tag{26}$$

Skin friction is an engineering measure of drag, hence the viscosity induced shear stress, and is defined as

$$C_f \equiv \tau_w \left[\frac{1}{2}\rho_I \, u_I^2\right]^{-1/2} \tag{27}$$

Equation (27) is also evaluable using the defined p_i.

DISCUSSION AND RESULTS

Presented herein are the results of the numerical evaluation of solutions of the selected non-linear parabolic and hyperbolic partial differential equations. Primary emphasis is on quantization of solution accuracy and convergence with discretization refinement. Test cases used are the steady two-dimensional incompressible laminar and turbulent boundary layer flow and laminar and turbulent parabolic flow in a duct. For turbulent flows, a comparison between the mixing length closure and the turbulent kinetic energy model has been established. Additional results are presented of the numerical solution of the transient continuity equation, with primary emphasis on solution economy, accuracy and convergence of the developed split-Jacobian finite element algorithm.

Parabolic Equation Solutions

Problem Statement

It is required to establish the two-dimensional velocity and pressure distributions, $\vec{u}(x,y)$ and $p(x,y)$, where

$$\vec{\tilde{u}}(x,y) \equiv u(x,y)\hat{i} + v(x,y)\hat{j} \tag{28}$$

Using the boundary layer order of magnitude analysis for large Reynolds number, cf. Schlichting (1968), the parent time-averaged steady flow Navier-Stokes equations in non-dimensional form are

$$L(\rho) = \frac{\partial \tilde{u}}{\partial x} + \frac{\partial \tilde{v}}{\partial y} = 0 \tag{29}$$

$$L(\tilde{u}) = \tilde{u}\frac{\partial \tilde{u}}{\partial x} + \tilde{v}\frac{\partial \tilde{u}}{\partial y} - \frac{\partial}{\partial y}\left\{\nu\frac{\partial \tilde{u}}{\partial y} - \overline{u'v'}\right\} + \frac{1}{\rho}\frac{d\bar{p}}{dx} = 0 \tag{30}$$

At the edge of the boundary layer, the viscous terms are zero, and the x-momentum equation (30) with the continuity equation (29) reduces to

$$U_I\frac{\partial U_I}{\partial x} = -\frac{1}{\rho}\frac{\partial \bar{p}}{\partial x} \tag{31}$$

where U_I is the inviscid flow velocity at the edge of the boundary layer. The x-axis is assumed aligned with the direction of predominant flow, and y is the coordinate traversing the thickness of the boundary layer, see Figure 1. Under the large Reynolds number assumption, the transverse momentum equation is identically satisfied by a pressure distribution impressed uniformly across the boundary layer thickness, i.e., $p(x,y) = p_I(x)$.

Closure of equations (2)-(4) requires a relationship be established for laminar viscosity ν and the dominant Reynolds stress shear component $\overline{u'v'}$. Kinematic viscosity ν is a property of the fluid constituting the boundary layer, and a constant for isoenergetic subsonic flows. Closure for the Reynolds stress $\overline{u'v'}$ is accomplished in the elementary form by assumption of an "effective" viscosity coefficient ν^e defined as

$$\nu^e \equiv \frac{\nu}{Re} + \nu^t \tag{32}$$

where ν^t is the "turbulent kinematic viscosity" correlation coefficient

$$-\overline{u'v'} \equiv \nu^t \frac{\partial \tilde{u}}{\partial y} \tag{33}$$

Hence, the parabolic equation (30) of primary interest in this investigation takes the form

$$L(\tilde{u}) = \tilde{u}\frac{\partial \tilde{u}}{\partial x} + \tilde{v}\frac{\partial \tilde{u}}{\partial y} - \frac{\partial}{\partial y}\left[\nu^e \frac{\partial \tilde{u}}{\partial y}\right] + \frac{1}{\rho}\frac{d\bar{p}}{dx} = 0 \tag{34}$$

Two closure models are used in this analysis. Prandtl mixing length theory (MLT) establishes an algebraic relation for ν^t (cf. Schlichting, 1968; Cebeci and Smith, 1974). Using a dimensional analysis, ν^t involves the product of a scale velocity and a scale length. Using the mean velocity gradient for the former, and Prandtl's mixing length ℓ for the latter, yields

$$\nu^t \equiv \omega^2 \ell^2 \left|\frac{\partial \tilde{u}}{\partial y}\right| \gamma \tag{35}$$

The mixing length ℓ is defined as

$$\ell \equiv \begin{cases} \kappa y & 0 \leq y \leq \lambda\delta/\kappa \\ \lambda\delta & y > \lambda\delta/\kappa \end{cases} \tag{36}$$

The Van Driest function ω accounts for the damping influence of a wall on the velocity fluctuations $\vec{u}'$. Following a rigorous analysis (cf. Cebeci and Smith, 1974), the damping function form is

$$\omega \equiv 1 - \exp(-y/A) \tag{37}$$

In equation (36), y is the coordinate normal to the surface, δ is the boundary layer thickness, and λ and κ are constants (typically 0.09 and 0.435 respectively). In equation (37), A is a complicated function of many factors influencing flow phenomena near the surface including axial pressure gradient and normal mass flow. The form of Cebeci and Smith (1974) serves to unify the many formulations as

$$A \equiv A^{+}\nu N^{-1}\left(\frac{\tau_w}{\rho_w}\right)^{-1/2}\left(\frac{\rho}{\rho_w}\right)^{1/2} \tag{38}$$

where

$$N^2 \equiv \frac{\nu}{\nu_I}\left(\frac{\rho_I}{\rho_w}\right)^2 \frac{p^+}{v^+}\left[1 - \exp\left(11.8\frac{\nu_w}{\nu}v^+\right)\right] + \exp\left[11.8\frac{\nu_w}{\nu}v^+\right] \tag{39}$$

All variables are time-averaged steady components, subscripts I and w refer to inviscid freestream and wall values respectively, A^+ is a constant (25.3), p^+ and v^+ are functions accounting for axial pressure gradient and mass addition respectively, cf. Cebeci and Smith (1974). In equation (38), τ_w is the wall shear stress defined as

$$\tau_w \equiv \rho_w \nu_w \left.\frac{\partial \tilde{u}}{\partial y}\right|_w \tag{40}$$

In this analysis the wall shear stress is evaluated from the Ludwieg-Tillman equation for skin friction

$$C_f \equiv \frac{\tau_w}{\frac{1}{2}\rho_e u_e^2} \equiv 0.246 \times 10^{-0.678H} Re_\theta^{-0.268} \tag{41}$$

In equation (31), H is the shape factor and Re_θ is the Reynold's number based on the momentum thickness θ. Since the freestream outside the boundary layer is assumed free of turbulence, the intermittency factor γ in equation (35) is

$$\gamma = \left[1 + (y/\delta)^9\right]^{-1} \qquad y > \delta \tag{42}$$

which serves to provide a rapid decrease of ν^t at the freestream edge of $\delta(x)$.

An alternative formulation to Prandtl's mixing length model that yields a differential equation statement is the turbulent kinetic energy (TKE) two-equation model. For this, the scale velocity is selected as the kinetic

energy k of the velocity fluctuations

$$k \equiv \frac{1}{2}\overline{\vec{u}' \cdot \vec{u}'} \tag{43}$$

The length scale is defined as ℓ_d, the scale length of isotropic dissipation of a fluctuating velocity eddy, cf. Tennekes and Lumley (1974). Hence, for the TKE closure equation (35) is replaced as

$$\nu^t \equiv k^{1/2}\ell_d \tag{44}$$

The dissipation length scale may be expressed in terms of the isotropic dissipation rate of turbulence ε, cf. Hanjalić and Launder (1972), defined as

$$\ell_d \equiv C_\nu k^{3/2}/\varepsilon \tag{45}$$

where C_ν is the correlation constant. Combining equations (44)-(45) yields

$$\nu^t = C_\nu k^2/\varepsilon \tag{46}$$

which corresponds to the two-equation TKE model definition for turbulent effective viscosity.

A partial differential equation system for the determination of the turbulent kinetic energy k and the dissipation rate of turbulence ε is required. For turbulent incompressible boundary layer flow, the appropriate system is (Cebeci and Smith, 1974)

$$L(k) = \tilde{u}\frac{\partial k}{\partial x} + \tilde{v}\frac{\partial k}{\partial y} - \frac{\partial}{\partial y}\left[\frac{\nu^e}{C_k}\frac{\partial k}{\partial y}\right] - \nu^e\left(\frac{\partial \tilde{u}}{\partial y}\right)^2 + \varepsilon = 0 \tag{47}$$

$$L(\varepsilon) = \tilde{u}\frac{\partial \varepsilon}{\partial x} + \tilde{v}\frac{\partial \varepsilon}{\partial y} - \frac{\partial}{\partial y}\left[\frac{\nu^e}{C_\varepsilon}\frac{\partial \varepsilon}{\partial y}\right] - C_\varepsilon^1 \varepsilon k^{-1}\nu^e\left(\frac{\partial \tilde{u}}{\partial y}\right)^2 + C_\varepsilon^2 \varepsilon^2 k^{-1} = 0 \tag{48}$$

The various C_α^β are correlation constants of the model. Table 1 lists values used in this analysis, as recommended by Hanjalic′ and Launder (1972) for two-dimensional shear flows.

TABLE 1
CORRELATION COEFFICIENTS IN TKE CLOSURE MODEL

Variable	Equation	
ν^t	(46)	$C_\nu = 0.09$
k	(47)	$C_k = 1.0$
ε	(48)	$C_\varepsilon = 1.3$, $C_\varepsilon^1 = 1.44$, $C_\varepsilon^2 = 1.92$

Closure of equations (29)-(30) also requires establishment of appropriate boundary and initial conditions. The boundary conditions for solution of equations (29)-(30) are determined by inspection. At the surface $y = 0$, no-slip and no injection is assumed yielding

$$u(x,0) = v(x,0) = 0 \tag{49}$$

At the freestream, $y > \delta(x)$, from equations (30) and (31)

$$\frac{\partial \tilde{u}(x, y > \delta)}{\partial y} = 0 \tag{50}$$

The boundary conditions for k and ε are vanishing at both the inviscid freestream edge and at the solid surface. For the latter location, it is also necessary to enforce the wall damping influence on the velocity fluctuations, in the manner of the Van Driest damping function ω for the MLT closure.

Since equations (34), (47) and (48) also display initial-value character, an appropriate specification is required to initiate a solution.

Any arbitrary profile for $\tilde{u}$ is admissable that also satisfies equations (49)-(50). For k and ε in boundary layer type flows, cf. Launder and Spalding (1972), the length scale ℓ_d is proportional to y in the immediate vicinity of a wall. From an exact analysis, hence

$$\ell_d = C_D^{1/4}\kappa y, \quad 0 \leq y \leq C_D\delta \tag{51}$$

where $C_D = 0.09$ and κ is von Karman's constant (0.435). Away from the wall, ℓ_d eventually becomes independent of y and levels off at a value about equal to $C_D\delta$, where δ is the local boundary layer thickness. Assuming a continuous distribution of ℓ_d between these extrema, and using the MLT model to compute ν^t, an initial distribution of both k and ε can be determined using equations (45), (46), and (51).

An added complication of the problem specification is that δ, the boundary value solution domain to be spanned by the finite element discretization, is variable with x, see Figure 2. A transverse coordinate stretching transformation can efficiently compensate for boundary layer thickness growth. Referring to Figure 3, a useful transformation is

$$\bar{\xi} \equiv x$$

$$\eta \equiv \frac{y - f_1(x)}{\left[f_2(x) - f_1(x)\right]/f} \tag{52}$$

where η is the normalized coordinate lying between two piecewise continuous surfaces, $f_1(x)$ and $f_2(x) > f_1$, that bound the solution domain R^1, and where f is a normalizing factor. For the boundary layer flow, f_1 typically corresponds to a surface and is a constant, while f_2 is appropriately specified. The chain rule for differentiation yields

$$\frac{\partial}{\partial x} = \frac{\partial}{\partial \xi}\frac{d\xi}{dx} + \frac{\partial}{\partial \eta}\frac{d\eta}{dx}$$

$$= \frac{\partial}{\partial \xi} - \left[\frac{f_1'}{\left(f_2 - f_1\right)/f} + \eta\frac{f_2' - f_1'}{f_2 - f_1}\right]\frac{\partial}{\partial \eta} \tag{53}$$

where superscript prime denotes the ordinary derivative. The resultant form of the three initial-valued equations (34), (47), and (48), and the continuity equation (29), is

$$L(\tilde{v}) = \left[\frac{\partial}{\partial \xi} - (h_2 + \eta h_3)\frac{\partial}{\partial \eta}\right]\tilde{u} + \frac{\partial \tilde{v}}{\partial \eta} = 0 \tag{54}$$

$$L(u) = \tilde{u}\left[\frac{\partial}{\partial \xi} - (h_2 + \eta h_3)\frac{\partial}{\partial \eta}\right]\tilde{u} + \tilde{v}\frac{\partial \tilde{u}}{\partial \eta} - \frac{\partial}{\partial \eta}\left[\nu^e h_1 \frac{\partial \tilde{u}}{\partial \eta}\right] + \frac{1}{\rho}\frac{dp_I}{d\xi} = 0 \tag{55}$$

$$L(k) = \tilde{u}\left[\frac{\partial}{\partial \xi} - (h_2 + \eta h_3)\frac{\partial}{\partial \eta}\right]k + \tilde{v}\frac{\partial k}{\partial \eta}$$
$$- \frac{\partial}{\partial \eta}\left[\frac{\nu^e h_1}{C_k}\frac{\partial k}{\partial \eta}\right] - \nu^e\left(\frac{\partial \tilde{u}}{\partial \eta}\right)^2 + \varepsilon = 0 \tag{56}$$

$$L(\varepsilon) = \tilde{u}\left[\frac{\partial}{\partial \xi} - (h_2 + \eta h_3)\frac{\partial}{\partial \eta}\right]\varepsilon + \tilde{v}\frac{\partial \varepsilon}{\partial \eta}$$
$$- \frac{\partial}{\partial \eta}\left[\frac{\nu^e h_1}{C_\varepsilon}\frac{\partial \varepsilon}{\partial \eta}\right] - C_\varepsilon^1 \varepsilon k^{-1}\nu^e\left(\frac{\partial \tilde{u}}{\partial \eta}\right)^2 + C_\varepsilon^2 \varepsilon^2 k^{-1} = 0 \tag{57}$$

The functions h_i, $1 \le i \le 3$, are related to the metric of the coordinate transformation and defined as

$$h_i \equiv \begin{Bmatrix} f(f_2 - f_1)^{-1} \\ f_1' h_1 \\ f^{-1}(f_2' - f_1')h_1 \end{Bmatrix} \tag{58}$$

The superscript prime denotes ordinary differentiation with respect to x, and the h_i are at most a function of x or ξ.

Finite Element Solution Algorithm

The finite element solution is established assuming all dependent variables and parameters are interpolated on disjoint interior subdomains $\Omega_e \equiv R_e \times \chi$, where χ is a generalized initial-value coordinate. Defining the numerically determined finite element approximation to the true solution as q*, then

$$q^*(y,x) \equiv \sum_{e=1}^{M} q_e(y,x) \tag{59}$$

where M is the total number of finite element domains R_e^1 spanning R^1. On each domain Ω_e, then

$$q_e(y,x) = q_e(x_1,\chi) \equiv \{N_k(x_1)\}^T\{Q(\chi)\}_e \tag{60}$$

where the union of Ω_e forms the solution domain $\Omega \equiv R^1 \times \chi \in y \times x$. Furthermore, the elements of $\{N_k\}$ are interpolation polynomials complete to degree k, while the elements of $\{Q\}_e$ are the to-be-determined expansion coefficients. Using the familiar Galerkin-Weighted Residuals formulation, cf. Baker and Soliman (1977), and for the dependent variable q identified with u(x,y), the elementary form of the finite element solution algorithm for equation (34) becomes, cf. Baker (1978)

$$\underset{e}{S}\left[\{U\}_e^T \int_{R_e^1} \{N_k\}\{N_k\}\{N_k\}^T dx_1 \{U\}_e + \{XNUEFF\}_e^T \int_{R_e^1} \{N_k\} \frac{d}{dx_1}\{N_k\} \frac{d}{dx_1}\{N_k\}^T dx_1 \{U\}_e \right.$$

$$\left. + \int_{R_e^1} \{N_k\}\{N_k\}^T\{V\}_e \frac{d}{dx_1}\{N_k\}^T dx_1 \{U\}_e + \frac{1}{\rho}\frac{dp_I}{dx} \int_{R_e^1} \{N_k\} dx_1 \right] \equiv \{0\} \tag{61}$$

where $\underset{e}{S}$ is the finite element assembly operator. In hypermatrix form, cf. Baker and Soliman (1978), equation (61) for the case of no grid stretching becomes

$$\underset{e}{S}\Big[\Delta_e\{U\}_e^T[A3000]\{U\}_e'$$

$$+\ \Delta_e\Big(\{XNUEFF\}_e^T[A3011] + \{V\}_e^T[A3001]\Big)\{U\}_e$$

$$+\ \Delta_e p_I'\{A10\}\Big] \equiv \{0\} \tag{62}$$

In equation (62), the matrix elements of $\{XNUEFF\}_e$ are the nodal values of the effective viscosity ν^e, equation (32), on R_e. Completion of the solution specification is achieved as

$$\{U(x_o)\} \Longleftrightarrow \tilde{u}(x_o,y) \tag{63}$$

which corresponds to a mapping of the initial condition for $\tilde{u}$ onto the nodal coordinates of $\sum_e u_e$. The rank of the global matrix system equation (62) is one less than its order, to account for the no-slip boundary condition $\tilde{u}(x,0) = 0$. Hence, application of the finite element algorithm to equation (34) has yielded a system of ordinary differential equations (62) with initial conditions equation (63) for solution of the node point distribution of the discretized velocity, $\tilde{u}$, i.e. $\{U\} \equiv \sum_e\{U\}_e$.

Solution of equation (62) requires determination of the discretized equivalent transverse velocity distribution $\{V\}$, hence $\{V\}_e$. The x dependence in $\tilde{v}(x,y)$ is parameterized, resulting in an ordinary differential equation specification in the form

$$\frac{\partial\tilde{v}(x,y)}{\partial y} \longrightarrow \left.\frac{dV(y)}{dy}\right|_x \equiv V'(x) = f(x,y) \tag{64}$$

$$f(x,y) \longrightarrow -\{U(x)\}' \tag{65}$$

Hence, the y-dependence in f(x,y) is discretely determined at node points of the finite element discretization of R^1, and equations (64)-(65) express solution for transverse velocity in the standard form of an ordinary differential equation with x as a parameter. The trapezoidal rule numerical integration algorithm was employed for the present solutions yielding

$$V(x)_{n+1} = V_n(x) + \frac{\Delta y}{2}\left[f(x)_{n+1} + f_n(x)\right] \tag{66}$$

In equatin (66), $\Delta y \equiv (y_{n+1} - y_n)$ is the integration step-size for equation (66), which lies in the domain R^1 spanned by the finite element discretization of equation (62). A second order accurate backwards difference formula for f(x) was employed to evaluate the vector $\{U\}'$ as

$$\{U(x_p)\}' = \frac{1}{h_p h_{p-1}(h_p + h_{p-1})}\Big[h_{p-1}(2h_p + h_{p-1})\{U\}_p - (h_p + h_{p-1})^2\{U\}_{p-1} + (h_p)^2\{U\}_{p-2}\Big] \tag{67}$$

In equation (67), h_p and h_{p-1} are the current and immediate past Δx integration step-sizes used for the solution of equation (62).

Restatement of the finite element algorithm, now using the coordinate transformation equation (52), is obtained by simply letting q_e represent each of $\tilde{u}_e$, k_e, and ε_e in equation (60), yielding

$$\underset{e}{S}\Big[\Delta_e\{U\}_e^T[A3000]\{Q\}_e' - \Delta_e\{U\}_e^T\Big[h_2[A3000] + \Big(h_3\{ETA\}_e^T - \{V\}_e^T\Big)[A40001]\Big]\{Q\}_e + \Delta_e h_1\{XNUEFF\}_e^T[A3011]\{Q\}_e + \Delta_e\{SORCQ\}_e\Big] \equiv \{0\} \tag{68}$$

The elements of the column matrix $\{ETA\}_e$ are the (stationary) nodal coordinates of the finite element discretization of R^1. In equation (68), $\{SORCQ\}_e$ is the source/sink term, distinctive for each identification of q. From equation (61), for $q = \tilde{u}$

$$\{SORCU\}_e = p_I'\{A10\} \tag{69}$$

which is independent of e since p_I' is element independent. For $q = k$, referring to equation (56)

$$\int_{R_e^1} \nu^e \left(\frac{\partial \tilde{u}}{\partial \eta}\right)^2 d\eta = \{XNUEFF\}_e^T \int_{R_e^1} \{N_k\}\{U\}_e^T\{N_k\}'\{N_k\}'\{U\}_e\{N_k\}d\eta$$

$$= \Delta_e\left(\{XNUEFF\}^T[A40011]\{U\}_e\right)\{U\}_e \tag{70}$$

In equation (70), [A40011] is a hypermatrix of order k+2, where k is the complete degree of the finite element interpolation polynomial, equation (60), and each matrix element of [A40011] is similarly a square matrix of the same order. Hence, the source term for k can be expressed as

$$\{SORCK\}_e = -\left(\{XNUEFF\}_e^T[A40011]\{U\}_e\right)\{U\}_e + [A200]\{EPS\}_e \tag{71}$$

where the braces have been added to emphasize that the inner matrix product must be performed first.

The source term for ε in equation (57) involves the irrational function ε/k. Since both ε and k are interpolated over R_e^1 using equation (60), and as an alternative to an exact handling ε/k, an element average is employed as

$$\frac{\varepsilon_e}{k_e} = \frac{\{A10\}^T\{EPS\}}{\{A10\}^T\{K\}} \equiv \overline{\varepsilon/k_e} \tag{72}$$

To within a scalar factor, $\{SORCEP\}_e$ then becomes identical to $\{SORCK\}_e$ as

$$\{SORCEP\}_e \equiv -C_\varepsilon^1 \overline{\varepsilon/k}_e \left(\{XNUEFF\}_e^T [A40011]\{U\}_e\right)\{U\}_e + C_\varepsilon^2 \overline{\varepsilon/k}\, [A200]\{EPS\}_e \tag{73}$$

The energy inner product, equation (6), for the boundary layer equation system is required established to evaluate convergence in the energy norm. The discrete solution energy norm is

$$E_k^{(M)}(u^*,u^*) = \sum_{e=1}^{M} \frac{1}{2}\int_{R_e^1} \frac{\nu}{Re}(u_{,y}^*)^2 dy$$

$$= \frac{1}{2}\frac{1}{Re}\sum_{e=1}^{M} \Delta_e \left[\{U\}_e^T \left(\{XNUEFF\}_e^T [A3011]\right)\{U\}_e\right] \tag{74}$$

Convergence properties of solely the finite element discrete solution are determinable as, see equations (34), (8), and (9)

$$E_k^{(M)}\left(\varepsilon(x),\varepsilon(x)\right) \leq C_2 \Delta_e^{2(k+1-m)} \|u\|_{k+1}^2 \tag{75}$$

where

$$\|u\|_{k+1}^2 \equiv \int_{R^1} \left(\frac{\partial^{k+1} u}{\partial y^{k+1}}\right)^2 dy < \infty \tag{76}$$

For the boundary layer problem, 2m is the order of equation (34), hence $m = 1$, and k is the degree of the highest complete polynomial in the approximation to $u(x,y)$.

Error and convergence are also measured in terms of the boundary layer integral parameters. As discussed, boundary layer displacement (δ^*) and momentum (θ) thickness are variables of primary interest in engineering evaluation and evaluable in terms of the p-norms. For the discrete solutions,

$$\delta^*(x) \equiv \int_0^\infty \left[1 - \frac{u(x,y)}{u_I(x)}\right] dy = \sum_{e=1}^{M} \left[\{A10\}^T \{1 - U/U_I\}_e\right] \tag{77}$$

$$\theta(x) \equiv \int_0^\infty \frac{u(x,y)}{u_I(x)}\left[1 - \frac{u(x,y)}{u_I(x)}\right] dy = \sum_{e=1}^{M} \left[\{U/U_I\}_e^T [A200] \{1 - U/U_I\}_e\right] \tag{78}$$

These norms are herein used primarily to assess solution accuracy in terms of the shape factor H,

$$H \equiv \delta^*/\theta \tag{79}$$

and the skin friction coefficient C_f

$$C_f \equiv \frac{\tau_w}{\frac{1}{2}\rho_I u_I^2} \equiv \left(\frac{1}{2}\rho_I u_I^2\right)^{-1} \rho_w \mu_w \left.\frac{\partial u}{\partial y}\right|_w \tag{80}$$

Specifically, equation (80) is evaluated using the Ludwieg-Tillman formula, equation (41).

A Laminar Parabolic Flow

The fundamental requirement is to assess the convergence character of the finite element solution algorithm applied to the non-linear parabolic equation (30). The elementary case accrues for laminar flow, hence $\overline{u'v'} \equiv 0$. A further simplification is to assume that the transverse velocity component v is everywhere constant, specifically zero. This assumption violates the physics of the flow, except in the case u(x,y) u(y), wherein the continuity equation (54) is also satisfied. However, since the initial-value solution is of prime interest, for the first case the continuity equation was discarded and v set to zero. For non-vanishing pressure gradient, equation (55) then reduces to

$$L(\tilde{u}) = \tilde{u}\frac{\partial \tilde{u}}{\partial x} - \frac{\partial}{\partial y}\left(\nu \frac{\partial \tilde{u}}{\partial y}\right) + \frac{1}{\rho}\frac{d\bar{p}}{dx} = 0 \tag{81}$$

which is the most elementary model form for the developed equation system that displays the essential required non-linearity. The boundary conditions for solution of equation (81) remain expressed by equations (49)-(50), where δ is now assumed a symmetry plane, and the initial condition is the slug profile illustrated in Figure 4. Following an extensive numerical test program (Soliman, 1978), this initialization for $\tilde{u}$ was found mandatory to eliminate the initial data as the primary error source in the energy error norm, equation (74). Selecting the distribution illustrated provided a uniform initial energy for all k, $1 \leq k \leq 3$, on both uniform and non-uniform discretizations of Δ, the span of R^1. The particular data set selected was $U_\infty = 300$ ft/sec, $Re = 0.7 \times 10^6$/ft and $\Delta p = 1.458 \times 10^{-6}$. Following experimentation, quantization of convergence was determined facilitated after marching the solution downstream for an axial distance of approximately 0.5 ft; therefore, all data presented were measured at $\Delta x = 0.8$ ft.

Figure 5 presents computed solution error in the energy norm as a function of uniform discretization refinement for linear, quadratic, and cubic finite element interpolations. The numerical results confirm the prediction of the linear theory, equation (74), for $k = 1$ and 2. Specifically, convergence is exactly quadratic for the linear finite element solution, and essentially fourth-order for the quadratic elements. In contrast to theory, convergence is also fourth-order for the solutions obtained with cubic finite elements. Note that the level of error capable of quantization is of the order of 10^{-6}, which has been confirmed as the upper bound on accuracy for the equation solved, which is non-linear. As will be documented throughout this test program, the coarse grid linear finite element solutions display accuracy superior to that predicted by strict adherence to the convergence curve.

Conversely, those solutions obtained with quadratic finite elements display coarse grid inaccuracy. The finest grid case reported for a quadratic finite element solution ($M=40$) also displays a somewhat larger error than predicted by the fourth-order convergence rate, which is further confirmation of the accuracy level attainable in actual practice. As noted in the header of Figure 5, convergence is monotonic and from above for the linear and cubic element solutions, while the quadratic element solution displays oscillatory convergence.

Figures 6-7 present computed accuracy and convergence in the engineering norms of shape factor and skin friction, equations (77)-(80), for $k=1$, 2 and 3. Convergence is quadratic for the linear finite element solution, and from above in the case of the shape factor and from below for skin friction. Fourth-order accuracy is displayed by the quadratic finite elements, and in contrast with the energy norm, the coarse grid solution demonstrates a super-accuracy. The slope of a straight line drawn between the two data points for the cubic element solution is 5.8, which is in close agreement to the six that is predicted by the linear theory, equation (7), or specifically $k=3$ and $m=1$ in equation (75). The next consistent cubic element discretization requires $M=54$, the results for which far exceed the quantizable error of 10^{-6} for this problem. Hence, the cubic element formulation becomes essentially impractical for equations of this type in fluid mechanics.

The influence of employing a non-uniform finite element discretization of R^1, on the computed error in the energy norm, was determined and results are presented in Figure 8 for $k=1$ and 2. The abscissa for this curve is now the largest finite element Δ_e^{max} on R^1. The non-uniform discretization increases by up to a factor of two the level of absolute error in the energy norm for the linear element solution, $k=1$. Alternatively, for the quadratic, the error level is less than that associated with the uniform discretization, with an

indication that an optimum grid exists for which an essential minimum exists for energy. Figures 9-10 provide the comparison on the basis of error in H and C_f. In these norms, a favorable effect is accorded use of non-uniform discretization. The absolute error is substantially decreased using a non-uniform discretization for $k = 1$, and there is an optimum grid associated with an absolute error minimum in both shape factor and skin friction. The levels of absolute error are uniformly decreased for the $k = 2$ solutions, as well, although no optimum discretization is evident. The non-uniform discretization results display an essential fourth-order accuracy in shape factor norm, while a nominal third-order accuracy is evidenced for skin friction. In all cases then, the use of a non-uniform discretization is not contraindicated, and subsequent results for a physically meaningful equation statement will confirm this indication.

Laminar Boundary Layer Flow

The second and physically meaningful test case corresponds to incompressible laminar boundary layer flow impinging on a sharp leading edge with pressure gradient. The nominal freestream velocity remains $U_\infty = 300$ ft/sec and $Re = 0.7 \times 10^6$/ft. The slug-profile for u, Figure 4, remains initial condition for the stream-wise velocity, while the transverse velocity v is assumed zero at solution initiation. The transverse velocity remains zero until sufficient solution information has been generated to facilitate evaluation of the backwards difference formula, equation (66). To maintain a uniform evaluation of the initial data energy norm, equation (74), for all k and all initial-value matrix assembly operators S_α, the node at the knee of the initial slug profile for the streamwise velocity is kept at the same position (0.2Δ) for all grid refinements. To facilitate the required comparison with a popular finite difference solution algorithm, numerical results are also obtained using the equivalent of the

ORIGINAL PAGE IS
OF POOR QUALITY

familiar Crank-Nicholson algorithm for equation (62). This is achieved by rendering diagonal the initial value matrix [A3000], within the linear finite element formulation. The specific matrix equivalent for the initial-value matrix $[A3000]_3$ associated with Crank-Nicholson is

$$\underset{e}{S}\left[\Delta_e\{U\}_e^T[A3000]_3\{U\}_e^{\prime}\right] \doteq \underset{e}{S}\left[\Delta_e\{U\}_e^T\,\frac{1}{2}\begin{bmatrix}\begin{Bmatrix}1\\0\end{Bmatrix} & \begin{Bmatrix}0\\0\end{Bmatrix}\\ \begin{Bmatrix}0\\0\end{Bmatrix} & \begin{Bmatrix}0\\1\end{Bmatrix}\end{bmatrix}\{U\}_e^{\prime}\right] \tag{82}$$

For illustration, upon completing the assembly operation, defined as $S_\alpha \equiv 3$ herein, equation (62) can be reexpressed on a uniform grid in the (finite difference) recursion form

$$u_j u_j^{\prime} + \frac{1}{\Delta_e^2}\left[\nu_{j+1}u_{j+1} - 2\nu_j u_j + \nu_{j-1}u_{j-1}\right] + \frac{v_j}{2\Delta_e}\left[u_{j+1} - u_{j-1}\right] + P_I^{\prime} = 0 \tag{83}$$

Upon application of the trapezoidal integration formula for $u_j^{\prime}$, the resultant algebraic equation system is identical with the Crank-Nicholson algorithm, cf. Roache (1972).

Accuracy and convergence evaluations were again obtained at an axial displacement of 0.8 ft downstream from the leading edge of the plate. For linear finite element functions, $k = 1$ equation (60), convergence with discretization refinement in the energy norm is computed uniformly quadratic, for initial-value matrix structures $S = 0$, 2, and 3, see Figure 11, and with negligible data scatter. Herein, $S = 0$ corresponds to the exact finite element formulation, while $S = 2$ corresponds to the diagonalized structure previously employed by Baker and Manhardt (1977, 1978). (The operation $S = 1$ is another diagonalizing operator that is consistent only for linear element formulations, and thus relegated to history.) The errors are calculated with respect to an

estimated exact value of the energy norm, based on the assumption that the $S=0$ fine grid solutions do indeed converge quadratically. The lowest error in the energy norm is accorded the finite element solution algorithm, $S=0$, and the convergence is from below. Convergence is from above for the alternative diagonalized formulations $S = 2,3$. This confirms prediction of extension of the theoretical convergence theorem, equation (16), to this practical non-linear problem, and the finite element solution indeed minimizes the error in the energy. Note also that the error for the coarse grid finite element solution ($M=10$) falls below strict adherence to the convergence curve, confirming and firmly quantizing existence of coarse grid accuracy as previously predicted by Popinski and Baker (1976). Convergence in the engineering norms of H and C_f is also firmly quadratic for all $S = 0$, 2, and 3, see Figures 12-13, with the finite element solution over-predicting shape factor and under-predicting skin friction. This trend is again reversed for $S = 2$ and 3 solutions. The difference in level of error is much less pronounced in these norms, although the $S=0$ error is uniformly minimum, and coarse grid accuracy remains evident in the engineering norms.

Accuracy and convergence evaluation for linear, quadratic and cubic elements, $1 \leq k \leq 3$, for the same test case, and as measured in the energy norm for the consistent finite element initial-value matrix $S=0$, are presented in Figure 14. The solid curves are of nearest integer slope, and the demonstrated convergence rate for $k=1$, and the coarser grid solutions for $k=2$, predicts extension of the linear theory for both k to this non-linear equation. The cubic finite element results, $k=3$, and the finer grid solutions for the quadratic functions, $k=2$, fail to adhere to the convergence curves for error in the solution less than about 10^{-5}. This further confirms existence of a practical bound on actual performance of high order accurate numerical solution algorithms for non-linear equations of the boundary layer type. Furthermore,

the performance of the cubic element formulation is truly dismal. By comparison, absolute numerical accuracy for solution of linear parabolic equations was reported better than 10^{-12}, see Baker and Soliman (1978). Only for linear elements is convergence monotonic and from below. For the $k=2$ and $k=3$ cases, convergence is oscillatory and starts from below.

As a measure of solution economy, Figure 15 presents the error in the energy norm as a function of discretization refinement now expressed as the number of nodes on the solution domain. The abscissa is equivalently the rank of the Jacobian associated with solution of equation (62), and represents the amount of computational work required to obtain the solution. For all cases tested, except perhaps for the coarsest grid, the quadratic element solutions demonstrate a definitely superior economy and accuracy in the energy norm. The cubic element formulation is even less favorable on this comparison basis.

Figures 16-17 present computed convergence in the engineering norms for the finite element solutions obtained for $k = 1$, 2, and 3. Except for the coarse grid solutions obtained using the quadratic elements, convergence is generally quadratic for all k. The exception is the coarse grid solutions obtained with quadratic elements, wherein the $M=10$ solution is super-accurate, exceeding even 4th order convergence as indicated. This is most probably the direct consequence of the convergence being oscillatory. Note that the degraded convergence performance for $2 \leq k \leq 3$ occurs at error levels less than 10^{-5}. As was determined in the energy norm comparisons, a practical upper bound on attainable solution accuracy definitely exists for this non-linear parabolic equation, and appears to be of the order 10^{-5}. The overall superiority of the quadratic element formulation remains apparent, with the associated error roughly an order of magnitude less than that of the linear element solutions for approximately the same amount of computational work (same number of nodes).

These laminar flow results were obtained using uniform finite element discretizations of R^1. It is necessary to investigate the important effects of a non-uniform discretization, which is a key feature required for efficient and accurate turbulent flow computations. A smooth progression of non-uniformity of the finite element discretization is desired, and is attainable using a geometric progression to locate nodal coordinates on R^1 as

$$y_{e+1} = y_e + \frac{R^1}{\sum_{j=1}^{M} \rho^{j-1}} \rho^{(e-1)} \qquad 1 \leq e \leq M \tag{84}$$

In equation (84), y_{e+1} is the extremum nodal coordinate of R_e^1, y_e is the coordinate of the first node of R_e^1, ρ is the geometric progression ratio, and M is the total number of finite elements R_e^1 spanning the domain R^1.

The M = 80 linear element discretization was chosen as the base case for comparison of all non-uniform discretization results. The node at the knee of the streamwise velocity slug initial profile was maintained at a constant coordinate (20% of the domain), such that the initial data energy norm evaluation was uniformly a constant for all non-uniform discretizations. Figure 18 present computed accuracy and convergence in the energy norm for the linear finite element algorithm for a range of pressure gradients that yielded a zero and a ±50% change in solution energy compared to the initial data evaluation. The non-uniform discretization solutions are represented by partially shaded symbols, and the sign next to the symbol indicates that the sign of the norm changed with respect to the estimated correct value in comparison to the uniform discretization results. The computational advantage of using a non-uniform discretization is clearly demonstrated; the error in the energy norm is minimum for any number of elements spanning the solution domain using any non-uniform discretization. Furthermore, the non-uniform convergence curve, shown as a dashed line, passes through a minimum (zero) which indicates existence of an optimum grid ($M \approx 27$, $\rho \approx 1.2$) for this particular problem.

In the engineering norms, the effect of pressure gradient on the error is more apparent. Referring to Figures 19-20, the increase in level of error in the shape factor and skin friction is approximately five for the intermediate pressure gradient and ten for the extremal pressure gradient plotted. The beneficial effect of use of a non-uniform discretrization on error in the engineering norms decreases as the pressure gradient increases, and the discretization which extremizes the energy does not necessarily yield the lowest error in the engineering norms. However, in all cases, the accuracy attainable using a non-uniform grid is universally superior in any norm. A non-uniform grid containing approximately 25 elements will always yield accuracy comparable or superior to the 80 element uniform grid case at a factor of 3 reduction in computer CPU. Since the data collapse to an essential single curve, Figure 18, the energy norm appears the superior mathematical measure of accuracy for this non-linear parabolic equation system.

The comparison is required established for the alternative initial-value matrix operators, $S = 2$ and 3. Figure 21 presents computed convergence in the energy norm for the selected range of pressure gradients for solutions obtained employing the diagonalized initial-value matrix $S = 2$. Contrary to the numerical experience with the consistent form $S = 0$, see Figure 18, the absolute error in the energy norm decreases with the increase in pressure gradient level. The convergence rate remains essentially quadratic for uniform discretization solutions, but there is select data scatter and some evidenced coarse grid inaccuracy. Only in the case of zero pressure gradient is the error in the energy norm consistently reduced using a non-uniform discretization. The absolute level of improvement is drastically reduced in comparison with the consistent assembly results. The use of a non-uniform discretization modestly increases the error in the energy norm for the intermediate pressure gradient, $\Delta p = 1.525 \times 10^{-6}$, while converging from above. A select modest improvement, coupled with

convergence from below, is accorded the extreme pressure gradient solution, $\Delta p = 3.056 \times 10^{-6}$, for non-uniform grid comparison.

Convergence with discretization refinement, in the engineering norms for the diagonal matrix $S = 2$, is presented in Figures 19-20. Quadratic convergence is confirmed in all cases for the uniform discretization results, with negligible data scatter, and the absolute error in the norm now increases with the increase in pressure gradient, in accord with the results obtained for $S = 0$. In distinction, however, note that use of a non-uniform grid for zero-pressure gradient exerts no consequential effect on solution accuracy in either engineering norm or in energy. In contrast with error in the energy norm, Figures 21, non-uniform discretization can reduce error in both the shape factor and skin friction for non-zero pressure gradients. The absolute level of error in all three norms, comparing the $S = 0$ and $S = 2$ results, is approximately comparable to the uniform grid results. However, the $S = 0$ results are clearly superior in all norms for the case of zero pressure gradient.

The accuracy and convergence performance of the Crank-Nicholson finite difference initial-value equivalent, $S = 3$, is not consequently distinct from the $S = 2$ results. Figures 24-26 present the corresponding computed error in the solution norms as a function of the discretization refinement. Convergence is again essentially quadratic, with only modest data scatter for uniform discretization, with the absolute error higher than that associated with the finite element solution ($S = 0$) for zero pressure gradient and almost the same for non-zero pressure gradients. Somewhat improved accuracy accrues to use of non-uniform discretizations, in contrast with the diagonalized matrix ($S = 2$) results for zero pressure gradient. Non-zero pressure gradient performance is nominally identical. In terms of error in shape factor and skin friction, the $S = 3$ and $S = 2$ results do not differ. Interestingly, the use of non-uniform discretizations for zero pressure gradient again does not improve solution accuracy in either engineering norm.

Based upon these results, the consistent finite element initial-value matrix ($S = 0$) form for the linear ($k = 1$) solution algorithm demonstrates consistently superior solution behavior in terms of accuracy, convergence and economy for this practical non-linear parabolic equation system. Previous results (Baker and Soliman, 1978) indicate this to hold as well for use of higher degree ($k > 1$) finite element polynomials for a linear parabolic equation. Hence, numerical evaluation of accuracy and convergence obtained using higher-degree finite element functions is conducted for $S = 0$ only. Shown in Figure 27 is the computed solution error in the energy norm as a function of discretization refinement. The fourth order accuracy of the algorithm, which was documented earlier for zero pressure gradient (Figure 14), is now degraded to second-order for the cases involving non-zero pressure gradient. A plausible explanation for this is that the oscillatory convergence in the energy norm, associated with the zero pressure gradient solutions, changed to monotonic convergence from below upon applying a pressure gradient. Furthermore, coarse grid inaccuracy is now evidenced for non-zero pressure gradients, since the corresponding data points lie above the convergence curve. The absolute level of error for the non-zero pressure gradient case is five times smaller than that associated with the linear finite element solution for the finer grids (see Figure 18). This improvement over the linear element solution degenerates, however, as the grid progresses to coarse. The error for the $M = 5$ quadratic element solution is basically identical to that for the $M = 10$ linear element grid. Use of a non-uniform discretization, selecting the $M = 40$ element grid as the base case, consequentially reduces the absolute error level for all pressure gradient including zero, in agreement with the $k = 1$ solutions. In clear distinction, however, an optimum grid that extremizes the energy cannot be detected.

Figures 28-29 present the corresponding data on quadratic element solution error measured in the engineering norms. Convergence is essentially

quadratic for uniform discretization, with coarse grids displaying fourth-order convergence for all pressure gradients. Oscillatory convergence is the general trend for all the cases, except for skin friction with zero pressure gradient. The quadratic finite element solution is relatively favorable for the cases with pressure gradient, since the error in the shape factor is two orders of magnitude smaller than the solution error obtained with linear finite elements. This compares to only one order of magnitude difference for the zero pressure gradient case. Non-uniform discretizations display improved absolute error level for all cases, and there is no indication of an optimum grid. These solution convergence trends are unchanged when measured in the skin friction norm, except that the error now decreases with an increase of pressure gradient. Use of non-uniform discretization again decreases the absolute level of error with no indication of an optimum grid.

A Turbulent Boundary Layer Flow

Acceptable resolution of near wall damping phenomena is an essential key feature of turbulent flow computations. Since use of a uniform discretization would require an impractically large number of elements to span the solution domain, a non-uniform finite element discretization is required in all instances to obtain satisfactory computational efficiency in concert with acceptable solution accuracy. Baker and Manhardt (1977b) have determined that linear element solution speed and accuracy, using an explicit integration algorithm and $S = 2$, both accrue using a finite element discretization with nodal coordinates determined according to the geometric progression equation (84). Based upon the laminar flow results discussed, and assuming the linear equation theory extensible to the more non-linear turbulent flow equations, the linear finite element algorithm should yield a quadratically-convergent procedure. Similarly, by extension, the use of quadratic elements should yield a fourth-order convergent algorithm in energy.

ORIGINAL PAGE IS
OF POOR QUALITY

The first requirement in this analysis is to confirm indeed that the developed finite element algorithm is capable of accurate prediction of turbulent flow for which comparison results exist. This is provided solely by experimental data, and a particularly challenging configuration corresponds to the IDENT 2400 data, reported in the proceedings of the AFOSR-IFP-Stanford Conference on Computations of Turbulent Boundary Layers (1968). IDENT 2400 is the Bradshaw relaxing flow data set, which corresponds to evolution of a non-equilibrium subsonic boundary layer induced by abrupt removal of a moderately adverse pressure gradient from an initially equilibrium flow. Nominal freestream velocity (U_∞) is 33.5 m/s, wind tunnel background turbulence level was less than 0.1%, and the reference unit Reynolds number is 2.38×10^7 m^{-1}. The test case is considerably demanding since non-equilibrium phenomena are involved in the relaxation process. The base case results were generated using the linear element ($k = 1$) algorithm and a non-uniform discretization. Following considerable numerical experimentation, an adequate resolution of the wall region damping was determined captured using $M = 30$ linear elements spanning approximately 1.5δ, and a geometric progression ratio of $\rho = 1.222$, see equation (84). Turbulence closure for the base case was accomplished using mixing length theory (MLT), with the parameters κ and λ equated to their standard values of 0.435 and 0.09 respectively. For boundary conditions, both $\tilde{u}$ and $\tilde{v}$ vanish identically at the plate surface, and $\partial\tilde{u}/\partial\tilde{y}$ vanishes for $y > \delta$. The first member of IDENT 2400 data set was interpolated at the nodes of $\sum_e R_e^1$ to generate the initial distribution for $\tilde{u}$, and $\tilde{v}$ was assumed zero until sufficient data was generated to initialize the continuity equation solution, see equations (64)-(67). Shown in Figure 30 are comparisons between data and the computed solutions, for the important boundary layer parameters, and as obtained using the three initial-value matrix structures, $S = 0$, 2, and 3. The computed results were matched with the data at the

second experimental profile, as recommended in the Proceedings. These solutions were generated from equations (54)-(55) using the transformed coordinate system with 20% grid growth over the solution range of 1.3 m. Agreement with data is generally good, indicating the basic algorithm capable of accurate resolution of the physical problem. The correct trends and local extrema in δ^* are predicted; however, the overall level of the solution curve is somewhat high. The level of the curve for the standard finite element structure, $S=0$, is closer to the data than that predicted by $S=2$ and 3. The computed extremum of ν^e/ν, equation (32), for this case was 900, which indicates a high level of turbulence.

Shown in Figure 31 is a comparison of the computed energy norms for $S=0$, 2, and 3. Note that the energy norm is minimized by the finite element solution $S=0$ tnroughout the solution range, which generally predicts extension of the linear theory, equation (16), to this highly non-linear problem class. Figure 32 presents comparison between select computed velocity profiles and data at three downstream stations, and agreement is generally excellent.

To investigate the influence of discretization refinement on solution accuracy, the number of linear elements was doubled to $M=60$ while retaining the first node off the wall at the same physical location, to preserve satisfactory resolution of near-wall damping. The resulting progression ratio ρ for this non-uniform discretization was 1.089. Shown in Figure 33 are comparisons between data and computed solutions using the standard $M=30$ linear element discretization and the $M=60$ element discretization for the two different ratios of grid nodal progression. There is essential overall agreement between the two solutions obtained using 20% grid growth. The $M=60$ element discretization with 50% grid growth is in slightly better agreement with data at the further downstream stations except for a tendency to over-predict θ and δ^*. The computed energy norms for these three solutions are presented in

Figure 34. Note that the energy is minimized by the M = 60 element discretization in the near field part of the curve. Thereafter, the knee in the curve is associated primarily with the inclusion of an extra element in the solution domain due to the boundary layer growth. Using 50% grid growth to keep the boundary layer edge within the same element throughout the solution range resulted in the higher overall level for the energy norm associated with correspondingly larger element spans.

Figure 35 presents comparison between computed solutions obtained using the M = 60 linear element discretization and a M = 30 quadratic element discretization. The first node off the wall was maintained at the same physical location for both cases, which results in a progression ratio of 1.188 for the M = 30 quadratic element discretization. Note that using a non-uniform discretization for the quadratic element case results in placing the element vertex nodes in the geometric progression while the interior nodes remain located at the mid-span of an element. The grid growth was 20% for the linear and 30% for the quadratic element solutions. In comparison with the experimental data, the solution using quadratic finite elements yields generally more accurate estimates for the boundary layer parameters than that obtained with linear finite elements. This cannot be directly confirmed, however, from noting the results presented in Figure 36. The energy norm calculated using quadratic finite elements has a higher level than that calculated using linear finite elements throughout the solution range except for a small portion at the beginning. This is in part a direct result of a higher estimate of the boundary layer thickness δ, for the quadratic element solution, which yields correspondingly higher values of the effective viscosity ν^e/ν. The computed extremum of ν^e/ν for quadratic element solution was 937 compared to 891 for the linear finite element solution.

All results discussed were obtained at a fixed integration step size $x = 0.05$ ft, with reevaluation of the Jacobian every twelve integration steps. The solutions were assumed converged when the change in the dependent variable (streamwise veloc y $\tilde{u}/U_\infty$) was uniformly less than the convergence criteria $\varepsilon = 10^{-6}$. Additional tests using ε as small as 10^{-9} did not alter the signification digit in the solution norms. Table 2 summarizes the results of numerical experiments carried out to assess the efficiency of the algorithm for the Bradshaw relaxing flow test case as obtained with the $M = 30$ linear element non-uniform discretization with progression ratio $\rho = 1.222$. The tabulated results correspond to the final solutions at $\Delta x = 1.3$ m. The results tabulated for the energy norm, shape factor and skin friction show the significant place of the integration truncation error, as confirmed by a higher-order accurate solution obtained using Richardson extrapolation. The slash isolates the significant digit in each norm, with the upper result corresponding to the more accurate one obtained using half the regular integration step size (the Richardson step).

The reference solution in this comparison (case 1) was obtained using a fixed uniform integration step size $\Delta x = 0.05$ ft with reevaluation of the Jacobian every twelve integration steps, which required evaluation of the Jacobian 66 times throughout the solution range. Using twice the integration step size and reevaluating the Jacobian every 12 steps, case 2, yielded identical values for the norms while reducing the number of passes and accordingly the CPU by 33%. The effect of utilizing the coordinate transformation equation is documented by case 3, wherein the solution domain was allowed to grow linearly in the streamwise direction in such a fashion that the span of the solution domain at the final integration station was 20% larger than at solution initiation. This solution minimized the energy norm while the computed difference in the shape factor is 0.6% and in skin friction is 2.5%.

TABLE 2

EFFICIENCY OF THE LINEAR FINITE ELEMENT ALGORITHM - BRADSHAW RELAXING FLOW (MLT)

Case No.	Grid Growth %	Integration Step Size Δx ft	Convergence Criteria ε	CPU*	Number of Passes	Number of Jacobian Reevaluations	Percent Increase in Step Size	E (10^{-3})	H	C_f (10^{-3})
1	0	.005	10^{-6}	1.00	2341	66	0	.572/35 44	1.389/39 40	.1784/91 80
2	0	.010	10^{-6}	.67	1704	33	0	.572/05 13	1.3896/49 58	.17836/48 26
3	20	.005	10^{-6}	1.42	2418	66	0	.529/52 60	1.3805/04 15	.18293/30 51
4	0	.005	10^{-6}	1.03	2473	0	0	.572/36 47	1.3894/02 11	.17848/87 56
5	0	.005	10^{-4}	.53	905	66	0	.572/31 40	1.3893/54 66	.17850/20 00
6	20	.005	10^{-6}	.92	1438	27	10	.517/37 40	1.3721/86 90	.18421/68 70

*Normalized on case number 1.

Case 4 is identical to case 1 except that the initial Jacobian was retained throughout the solution range. The difference in the energy norm and both engineering norms between these two cases is beyond the significant digit based on Richardson extrapolation. Retaining the initial Jacobian resulted, however, in a 3% increase in the number of passes and CPU.

The influence of a relaxed convergence criteria ε is documented in case 5. Reducing ε by two orders of magnitude to 10^{-4} resulted in reducing the number of passes by 60% and a 47% saving in CPU. With this favorable economy feature, the change in the energy norm and the engineering norms from the reference case is again beyond the acceptable significant digit. In test case 6, the integration time step Δx was increased by 10% every time the Jacobian was reevaluated. This procedure reduced the number of passes by 38% and the number of Jacobian reevaluations by 60%. The energy norm was minimized while the change in the shape factor was 1% and that in the skin friction was 3%.

The results of an assessment of accuracy and convergence trends for linear element solutions are presented in Table 3. These results were obtained employing the finite element matrix $S = 0$ with a convergence criteria ε of 10^{-6}. The span of the first element Δ_1 was 0.27×10^{-3} ft, for the $M = 30$ element and the first $M = 60$ element discretization, while for the second $M = 60$ element and the $M = 120$ element discretizations, Δ_1 was 0.21×10^{-3} ft. The larger negative value for the change in the energy norm, normalized by the initial energy ($\Delta E/E$), indicates a greater minimization of the energy, since the energy norm decreases as the solution is marched downstream. On this basis, solution accuracy increases with discretization refinement. Note also that the normalized change in the shape factor ($\Delta H/H$) is not affected by discretization refinement, and thus could not be used to assess convergence.

ORIGINAL PAGE IS
OF POOR QUALITY

TABLE 3

ACCURACY AND CONVERGENCE OF THE LINEAR FINITE ELEMENT ALGORITHM - BRADSHAW RELAXING FLOW (MLT)

Number of Elements	Progression Ratio	Δ_1/Δ_e^{max}	Δ_e^{max}/δ	CPU*	Number of Passes	$\Delta E/E$	$\Delta H/H$
30	1.222	.0054	.20	1.00	635	-.167	-.036
60	1.089	.013	.085	1.98	638	-.201	-.036
60	1.095	.094	.094	2.02	655	-.204	-.038
120	1.039	.039	.039	4.74	847	-.219	-.038

*Normalized on 30 linear element grid.

Summarized in Table 4 is the corresponding assessment of accuracy and convergence trends for the quadratic element solutions for the same test case. The span of the first element Δ_1 was chosen to be twice that of the corresponding linear element discretization, with twice the toal number of elements in the solution domain. This procedure resulted in placing the first node off the wall in the same physical location for the linear and quadratic element cases, in an attempt to maintain consistent resolution of the near-wall damping. The CPU time is approximately the same for the corresponding linear and quadratic discretizations. The solutions employing quadratic elements display convergence in the energy norm with discretization refinement, as evidenced by a superior minimization of the energy norm. As for the linear element solutions, the normalized change in the shape factor was not affected by discretization. Comparing results in Tables 3-4 shows that the $M = 15$ and $M = 60$ quadratic element discretizations yield a superior energy minimization than the corresponding $M = 30$ and 120 linear element discretizations. This is not valid, however, when comparing the $M = 30$ quadratic element discretization to the $M = 60$ linear element discretization results. The influence of the progression ratio used to define the non-uniform discretization, on finite element solution accuracy, is shown in Table 5. The progression ratios which yield the largest negative value of $\Delta E/E$, i.e., extremum minimization of the energy norm, are also those which required the least number of passes. The computed effective viscosity at the first node off the wall (ν^e/ν) increases as the span of the first element Δ_1 increases, and the best results were obtained when ν^e/ν was approximately equal to 2. The normalized change in the shape factor decreases monotonically as the progression ratio decreases; hence, it could not be used to indicate the preference of any progression ratio over the others.

TABLE 4

ACCURACY AND CONVERGENCE OF THE QUADRATIC FINITE ELEMENT ALGORITHM - BRADSHAW RELAXING FLOW (MLT)

Number of Elements	Progression Ratio	Δ_1/Δ_e^{max}	Δ_e^{max}/δ	CPU*	Number of Passes	$\Delta E/E$	$\Delta H/H$
15	1.506	.0049	.45	1.00	608	-.178	-.038
30	1.188	.014	.16	1.96	614	-.198	-.038
30	1.200	.0087	.20	2.01	638	-.193	-.037
60	1.079	.023	.076	4.85	649	-.229	-.038

*Normalized on 30 linear element grid (Table 3).

TABLE 5

INFLUENCE OF PROGRESSION RATIO ON LINEAR FINITE ELEMENT SOLUTION ACCURACY - BRADSHAW RELAXING FLOW (MLT)

Progression Ratio	Δ_1/Δ_e^{max}	Δ_e^{max}/δ	Number of Passes	ν_1^e/ν	$\Delta E/E$	$\Delta H/H$
1.222	.0054	.20	635	1.151	-.167	-.036
1.211	.0069	.20	617	1.313	-.183	-.034
1.200	.0088	.20	605	.1629	-.220	-.034
1.189	.013	.16	606	2.205	-.220	-.033
1.178	.017	.16	610	3.181	-.163	-.027
1.167	.021	.15	623	4.799	-.163	-.020
1.155	.027	.15	646	7.387	-.187	-.014

Accuracy and Convergence for Turbulent Boundary Layer Flow

The presented results document viability of the finite element algorithm and the discretization philosophy for acceptably accurate turbulent boundary layer flow prediction. A tightly controlled numerical test case, analogous to that employed for the laminar flow analysis, is required to quantize accuracy level and convergence with discretization refinement. The case corresponds essentially to transition to turbulent flow of the laminar slug start in zero pressure gradient. The test conditions were selected identical to the Wieghardt data set (IDENT 1400, Proceedings of the Stanford Conference (1968)) with constant freestream velocity ($U_\infty = u_I = 33$ m/s) yielding a unit Reynolds number of 2.19×10^6 per meter. Five different non-uniform discretizations were used to study accuracy and convergence with discretization refinement. The total number of elements M spanning the solution domain R^1 and the corresponding node progression ratios ρ are listed in Table 6 for the linear and quadratic finite element solutions. All computed solutions were initialized essentially identical to the experiment, wherein a turbulence-free uniform flow impinged upon the plate leading edge, using the slug start profile shown in Figure 4.

TABLE 6

DISCRETIZATION DATA - TURBULENT FLAT PLATE FLOW

k = 1	M	12	24	36	48	60
	ρ	1.627	1.222	1.125	1.083	1.061
k = 2	M	6	12	18	24	30
	ρ	2.814	1.510	1.271	1.176	1.110

As before, the first node off the plate was held at the same physical position for all discretizations. The number of elements between the plate and the knee of the velocity profile was always one-sixth the total number of elements spanning the solution domain. No turbulence transition model was employed; instead computational transition from laminar to turbulent flow was specified to occur when shape factor H achieved 90% of the fully developed laminar flow value.

Figure 37 summarizes computed solution error obtained with the linear element algorithm as a function of discretization refinement. Convergence in the energy norm is essentially quadratic for the three initial-value matrix structures, $S = 0$, 2, and 3, with the finite element algorithm $S = 0$ again yielding the smallest level of error for any M. Note in all cases that convergence is from above. As in the laminar flow results, the finite element algorithm displays accuracy for the coarse grid that is superior to strict adherence to the convergence curve. Convergence in shape factor, Figure 38, is essentially quadratic and from below for the diagonalized ($S = 2$) and Crank-Nicholson algorithm ($S = 3$). The finite element results do not display a convergence trend in shape factor. Specifically, the error is uniformly constant and smaller than that for either the $S = 2$ or 3 results. Since shape factor is the ratio of δ^* and θ, see equations (77)-(79), their convergence properties were measured. As shown in Figure 39, convergence in both δ^* and θ is quadratic on coarse grids and nearly fourth order for finer discretizations. Since the curves are parallel, the error in the shape factor remains essentially constant as determined. Figure 40 shows that convergence measured in skin friction is essentially quadratic for all three forms $S = 0$, 2, and 3, with the finite element solution yielding the smallest error level for any M.

Based upon the experience with laminar flows, a fourth order accurate algorithm is anticipated to result from use of quadratic finite elements

assuming the linear theory holds. It is of particular importance to ascertain this, since the energy norm is now complexly related to level of turbulence within the flow (evolution) through the eddy viscosity. Recalling the energy definition, equation (6), and that eddy viscosity involves $\tilde{u}$ shear, the specific form of the energy norm is

$$E(q_e^*, q_e^*) \equiv \frac{1}{2} \sum_{e=1}^{M} \int_{R_e^1} \frac{\partial \tilde{u}_e^*}{\partial y} \left[\nu + \omega^2 \ell^2 \left| \frac{\partial u_e^*}{\partial y} \right| \right] \frac{\partial \tilde{u}_e^*}{\partial y} dy \tag{85}$$

From the Bradshaw test results, recall that ν^e/ν ranged to 10^3. Since the effective diffusion coefficient itself is strictly dependent upon the computed evolution of $\tilde{u}$, the non-linearity of the subject equation system will exert a profound impact on the convergence evaluations.

Figure 41 presents the error computed in the energy norm as a function of discretization refinement for the linear and quadratic element algorithms. Convergence is from below and of generally fourth degree for the quadratic element solution, which predicts extension of the linear theory. However, the results for the finest discretization show a significantly larger absolute error than predicted by the convergence curve. This is interpreted again as an indication of the limit of practically useful discretizations. The accuracy of the quadratic element solutions can be a factor of up to 50 improvement over the corresponding linear element results. Figures 42-43 present error in the engineering norms as a function of discretization refinement. Convergence is oscillatory in both norms for quadratic elements, as experienced in the case of laminar flow, and of essentially fourth degree to the attainable limit of accuracy. The absolute error in the engineering norms for the finer discretizations is considerably larger than predicted by the convergence curve, confirming the experience in the energy norm.

Accuracy Evaluation Using the TKE Closure

As a summary computational study, the turbulent kinetic energy two-equation closure model was evaluated using the finite element algorithm, with primary emphasis on solution economy. The test case corresponds to the Bradshaw data set discussed previously. Details on solution initiation are given by Soliman (1978), and consistent accuracy and convergence trends were computed using the TKE closure model for both the linear and quadratic element algorithms.

The efficiency of the solution algorithm employing the TKE closure model can be appreciably improved by using one Jacobian for the three dependent variables, resulting in a considerable reduction in required memory storage. Table 7 summarizes comparisons between different methods of handling the Jacobian. The reference solution (case 1) was obtained using the correct Jacobian for each of the three dependent variables $\tilde{u}$, k, and ε. Employing the $\tilde{u}$ Jacobian for each dependent variable solution resulted in deterioration of accuracy, as evidenced by the larger value of $\Delta E/E$, and an overall 8% increase in CPU. The third solution was obtained using the k Jacobian for each of the three dependent variables. This shows an improvement in accuracy over the three Jacobian reference case, as evidenced by a minimum $\Delta E/E$ and a 9% saving in computer CPU. No specific trends were indicated in $\Delta H/H$. To investigate influence on solution accuracy, of the accuracy of the turbulent viscosity evaluations within the Jacobian, ν^t was deliberately under-evaluated and convergence of the matrix iteration evaluated. Case 4 corresponds to using one-half the value of the turbulent viscosity ν^t calculated from the TKE model in the k Jacobian, which was used for all three dependent variables. The matrix iteration was convergent, but the Jacobian distortion resulted in a 13% increase in CPU over reference case 1 and 24% increase in CPU over case 4. However, solution accuracy was not consequentially affected, as evidenced by

TABLE 7

INFLUENCE OF THE JACOBIAN ON LINEAR FINITE ELEMENT SOLUTION - BRADSHAW RELAXING FLOW (TKE)

Case No.	Type of Jacobian	CPU*	Number of Passes	Number of Iterations for First Pass	$\Delta E/E$	$\Delta H/H$
1	3 Jacobians	1.00	1291	14	.137	-.059
2	$\tilde{u}$ Jacobian	1.08	1456	14	.151	-.060
3	k Jacobian	.91	1236	8	.111	-.058
4	$0.5\nu^t$	1.13	1531	12	.116	-.059
5	$0.1\nu^t$	--	--	>30	--	--

*Normalized on case number 1.

comparing the normalized change in the energy norm for cases 3 and 4. Test case 5 corresponds to using only one-tenth the calculated turbulent viscosity within the Jacobian. This proved to be too inaccurate an evaluation, and convergence could not be achieved after iterating 30 times at the first integration step. Hence, a completely accurate evaluation of the Jacobian is not necessary to achieve an adequately-accurate engineering solution, and significant solution economies can result from taking advantage of the versatility embedded within the Newton iteration algorithm.

Hyperbolic Equation Solution

Equations Solved

In Cartesian coordinates, the partial differential equation system governing transport of a scalar field, for example the transient continuity equation, is

$$L(q) = \frac{\partial q}{\partial t} + \vec{U} \cdot \nabla q = 0 \tag{86}$$

with boundary conditions

$$\ell(q) = a^1 q + \nabla q \cdot \hat{n} + a^3 = 0 \tag{87a}$$

and an initial condition

$$q(\vec{x},0) = q_0(\vec{x}) \tag{87b}$$

The goal of this analysis is a study of accuracy and solution economy of a factored Jacobian form of the developed Newton iteration-finite element solution algorithm. Select divergence-free rotational and irrotational velocity fields selected for this purpose include

Constant:

$$\vec{U}_1 = U_\infty(\alpha\hat{i} + \beta\hat{j}) \tag{88}$$

Solid Body Rotation:

$$\vec{U}_2 = r\Omega\hat{\theta}, \tag{89}$$

Irrotational Flow About a Cylinder:

$$\vec{U}_3 = U_\infty \nabla \times y\left[1 - \frac{\rho^2}{r^2}\right]\hat{k} \tag{90}$$

Irrotational Cylinder Flow with Circulation:

$$\vec{U}_4 = U_\infty \nabla \times \left[y\left[1 - \frac{\rho^2}{r^2}\right] + \frac{\Gamma}{2\pi} \ln\left[\frac{r}{\rho}\right]\right]\hat{k} \tag{91}$$

In equations (88)-(91), U_∞ is a reference freestream velocity, is the constant angular velocity, the two-dimensional solution spans $0 \leq x \leq a$, $0 \leq y \leq b$, is the circulation, and Γ is the cylinder radius. The initial distribution of $q(x,y,0)$ is established as a "cosine-hill" rotated about its centroidal node as

$$q_0(x,y,0) \equiv 100\left[\sin^2 \frac{\pi r}{\lambda}\right] \tag{92}$$

where $0 \leq r \leq \lambda$ is the local radial coordinate with origin (x_0,y_0), and λ is spanned by M finite elements. Figure 44a illustrates the initial condition given by equation (92) for $M = 8$ and $(x_0,y_0) = (7,7)$ on a 32×32 uniform square mesh of span $0 \leq a,b \leq 80{,}000$ m.

The statement of the finite element solution algorithm for equations (86)-(87), on $\Omega \equiv R^2 \times t$ is, cf. Baker (1978),

$$\underset{e}{S}\left[[B200]\{Q\}_e^{\cdot} + \left(\{U\}_e^T[B3001] + \{V\}_e^T[B3002]\right)\{Q\}_e\right] = \{0\} \tag{93}$$

The Jacobian of the matrix iterative solution of equation (93) is

$$[J] = \underset{e}{S}\left[[B200] + h\theta\left(\{U\}_e^T[B3001] + \{V\}_e^T[B3002]\right)\right] \tag{94}$$

and the iteration vector $\{\delta Q\}$ is solved as

$$[J]\{\delta Q\} = -\{F\} \tag{95}$$

For the factored Newton iteration algorithm, the Jacobian [J] and elements of {F} are reexpressed on two-dimensional space in terms of the tensor matrix product ($\otimes$). The two-dimensional factored Newton iteration algorithm is then written in the form

$$\left[J_2(Q)_{j-\ell}\right] \otimes \left[J_1(Q)_{j-\ell}\right]\{\delta Q\}_{j+1}^{p+1} = -\left\{F_1(\bar{Q})_{j+1}^{p}\right\} \otimes \left\{F_2(Q)_{j+1}^{p}\right\} \tag{96}$$

where $\bar{Q}$ represents an intermediate solution. In hypermatrix form, for a general one-step integration algorithm, equation (96) is written as

$$\begin{aligned}
&\underset{e}{S}\left[\Delta_{e_2}[A200] + h\theta\Delta_{e_2}\{V\}_e^T[A3001]\right] \\
\otimes\ &\underset{e}{S}\left[\Delta_{e_1}[A200] + h\theta\Delta_{e_1}\{U\}_e^T[A3001]\right]\{\delta Q\}_{j+1}^{p+1} \\
= -\ &\underset{e}{S}\left[\Delta_{e_1}[A200]\left(\{\bar{Q}\}_{j+1}^{p} - \{Q\}_j\right) + h\left(\theta\Delta_{e_1}\{U\}_e^T[A3001]\{\bar{Q}\}_{j+1}^{p}\right.\right. \\
&\qquad\left.\left. + (1-\theta)\Delta_{e_1}\{U\}_e^T[A3001]\{Q\}_j\right)\right] \\
\otimes\ &\underset{e}{S}\left[\Delta_{e_2}[A200]\left(\{Q\}_{j+1}^{p} - \{\bar{Q}\}_{j+1}\right) + h\left(\theta\Delta_{e_2}\{V\}_e^T[A3001]\{Q\}_{j+1}^{p}\right.\right. \\
&\qquad\left.\left. + (1-\theta)\Delta_{e_2}\{V\}_e^T[A3001]\{\bar{Q}\}_{j+1}\right)\right]
\end{aligned} \tag{97}$$

The comparisons between the factored Jacobian iteration algorithm, equation (96), and the conventional multi-dimensional algorithm, equations (93)-(94), are obtained for the velocity fields given in equations (88)-(89). Figure 44a shows the initial distribution of the wave packet on a 32×32 uniform grid for velocity field u_1. Figure 44 b presents the conventional multi-dimensional bilinear finite element algorithm solution after 150 time steps with $\Delta t = 125$ s. Figure 44c illustrates the final solution obtained by the multi-dimensional algorithm, but with the initial-value matrix diagonalized. Figure 44d shows the final solution obtained with the factored Newton iteration algorithm, equation (96). It is virtually identical to the conventional results, and was obtained at approximately one-fourth expenditure of computer CPU and one-fifth the computer core requirement. These differences are essentially direct reflections of matrix bandwidth of [J], hence become progressively more favorable as the mesh is refined. Table 8 summarizes a comparison between the factored algorithm 'A', and the conventional multi-dimensional algorithm 'B' for different values of the Courant number, $u\Delta t/\Delta_e$, and two initial-value matrix structures. The CPU times for 'B' are five to seven times larger than for 'A'. The finite element algorithm ($S = 0$) retains the peak better and has smaller trailing wakes than the diagonalized algorithm ($S = 2$). Numerical diffusion and dispersion error is also less for 'A' than for 'B' for largest value of Courant number.

Corresponding accuracy, CPU and storage trends were obtained for velocity field u_2; hence, only the factored algorithm results are presented. The solid-body rotation flowfield $\vec{U}_2$ is considerably more demanding, and provides a quantization of dispersion error. The solution parameters (q_0, a, b, U_∞, Δt, M) remain identical, the diagonalized algorithm is relegated to history, and Figure 45 illustrates the solution obtained at the quarter,

TABLE 8

COMPARISON BETWEEN THE FACTORED NEWTON ITERATION ALGORITHM AND THE MULTI-DIMENSIONAL BILINEAR ALGORITHM

Courant Number	CPU*		Peak Value (% of Original)				Maximum Wake (% of Original Peak)			
			A		B		A		B	
	A	B	S = 0	S = 2	S = 0	S = 2	S = 0	S = 2	S = 0	S = 2
0.1	4.26	19.52	102.	66. (88.)**	102.	62. (86.)	3.	-20.	3.	-19.
0.5	1.00	4.58	102.	63. (87.)	99.	60. (84.)	-5.	-21.	-5.	-23.
1.0	0.52	3.67	90. (92.)	56. (82.)	78. (94.)	53. (82.)	-10.	-21.	-19.	-30.

*Normalized on FE factored solution for C = 0.5.

**Maximum observed value.

ORIGINAL PAGE IS OF POOR QUALITY

three-quarter and full 360° rotation of the concentration packet. The initial-distribution would appear identical to Figure 44a, moved to the 9 o'clock position, and the exact solution would be Lagrangian advection of the initial distribution without distortion. The factored algorithm is again essentially free of numerical diffusion (the peak level remains intact). The ripple structure in the ground plane is dispersion error, and while modest in comparison to other solution algoriths, cf. Long and Pepper (1976), is borderline on acceptability. Filters can be constructed to annihilate short period waves, e.g. Raymond and Garder (1976), and Figure 44d illustrates the substantial imporvement accrued at the three-quarter turn of the filtered factored algorithm. Filtering can induce numerical diffusion, and the peak value has been reduced by 2%; a somewhat modified immediate trailing wake remains identifiable. For the multi-dimensional bilinear algorithm on a 32×32 uniform grid, the storage required for the Jacobian was 67×1089 locations compared to $2 \times 3 \times 1089$ locations for the factored algorithm. CPU for the bilinear algorithm was ten times larger than for the factored algorithm, and there was essentially no difference between the two solution accuracies.

The assessment of numerical preservation of symmetries and skew-symmetries by the factored algorithm was obtained using the irrotational velocity fields $\vec{U}_3$ and $\vec{U}_4$. Both correspond to flow about a cylinder of diameter $8\Delta_e$ and centered at the grid centroid. Two concentrations were symmetrically palced about the stagnation streamline, and all other solution parameters remain identical (q_0, a, b, U_∞, Δt, M). The computed filtered factored solution using $\vec{U}_3$ is shown in Figure 46 for select time steps. The far-downstream peak values are within 2% of the initial level, and dispersion error extrema are approximately ±4%. Exact symmetry of the two concentration cases throughout the advection was retained by the factored algorithm.

Figure 47 illustrates select results obtained by the factored algorithm, for the irrotational velocity field $\vec{U}_4$ with circulation. Very large gradients are illustrated supported with acceptable dispersion error and negligible loss of peak value.

LIST OF REFERENCES

AFOSR-IFP-Stanford Conference on Computation of Turbulent Boundary Layers (1968) Vol. I, Eds. S. J. Kline, G. Sovran, M. V. Morkovan, D. J. Cockrell, Vol. II, Eds. D. A. Coles, E. A. Hirst, published by Thermosciences Division, Department of Mechanical Engineering, Stanford University, 1969.

Baker, A. J. (1977) Finite Element Computational Fluid Mechanics. University of Tennessee, manuscript.

Baker, A. J., and Manhardt, P. D. (1977a) Finite Element Analysis of Low Speed Viscous and Inviscid Aerodynamic Flows. NASA CR-2908.

Baker, A. J., and Manhardt, P. D. (1977b) Finite Element Analysis of Aeroacoustic Jet-Flap Flows. NASA CR-2931.

Baker, A. J., and Manhardt, P. D. (1978) An Interaction Solution Algorithm for Viscous Aerodynamic Performance Prediction. AIAA Paper No. 78-153.

Baker, A. J., and Soliman, M. O. (1977) On the Accuracy and Convergence of Implicit Numerical Integration of Finite Element Generated Ordinary Differential Equations. Proceedings, International Symposium on Simulation, Software and Numerical Methods for Differential Equations, IMACS, pp. 1-8.

Baker, A. J., and Soliman, M. O. (1978) Accuracy, Convergence, and Utility of Finite Element Generated Solution Algorithms for Initial Value Problems. J. Comp. Phys., under revision.

Cebeci, T., and Smith, A. M. O. (1974) Analysis of Turbulent Boundary Layers, Academic Press, New York.

Hanjalic , K., and Launder, B. E. (1972) A Reynolds Stress Model of Turbulence and its Application to Thin Shear Flows. J. Flu. Mech., Vol. 52, pp. 609-638.

Long, P. E., and Pepper, D. W. (1976) A Comparison of Six Numerical Schemes for Calculating the Advection of Atmospheric Pollution. Proceedings of Third Symposium on Atmospheric Turbulence, Diffusion and Air Quality, Raleigh, North Carolina.

Popinski, Z., and Baker, A. J. (1976) An Implicit Finite Element Algorithm for the Boundary Layer Equations. J. Comp. Phys., 21, No. 1, pp. 55-84.

Raymond, W. H., and Garder, A. (1976) Selective Damping in a Galerkin Method for Solving Wave Problems with Variable Grids. Monthly Weather Review, Vol. 104, pp. 1583-1590.

Roache, P. J. (1972) Computational Fluid Mechanics, Hermosa Publishers, Albuquerque, New Mexico.

Schlichting, H. (1968) Boundary Layer Theory, McGraw-Hill, New York.

Strang, G., and Fix, G. J. (1973) An Analysis of the Finite Element Method, Prentice Hall, New Jersey.

Tennekes, H., and Lumley, J. L. (1974) A First Course in Turbulence, The MIT Press, Cambridge, Massachusetts.

Soliman, M. O. (1978) Accuracy and Convergence of a Finite Element Algorithm for Computational Fluid Dynamics. Ph.D. Dissertation, University of Tennessee, Knoxville.

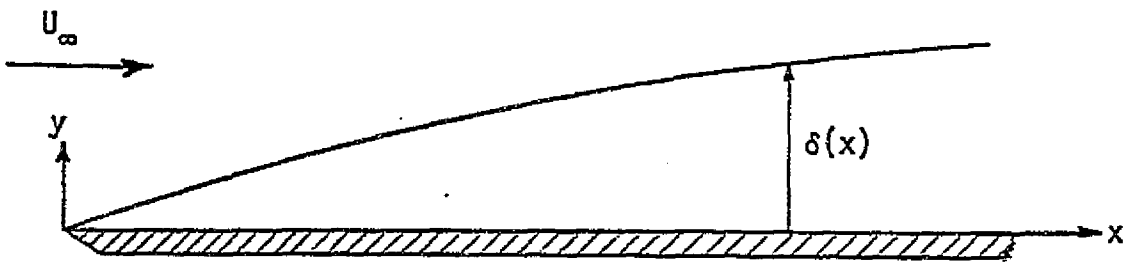

Figure 1. The Boundary Layer Flow Solution Domain

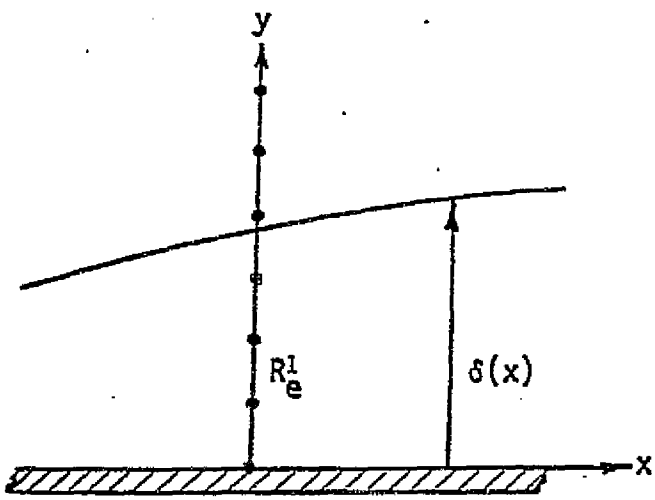

Figure 2. Finite Element Discretization of the Boundary Layer Region

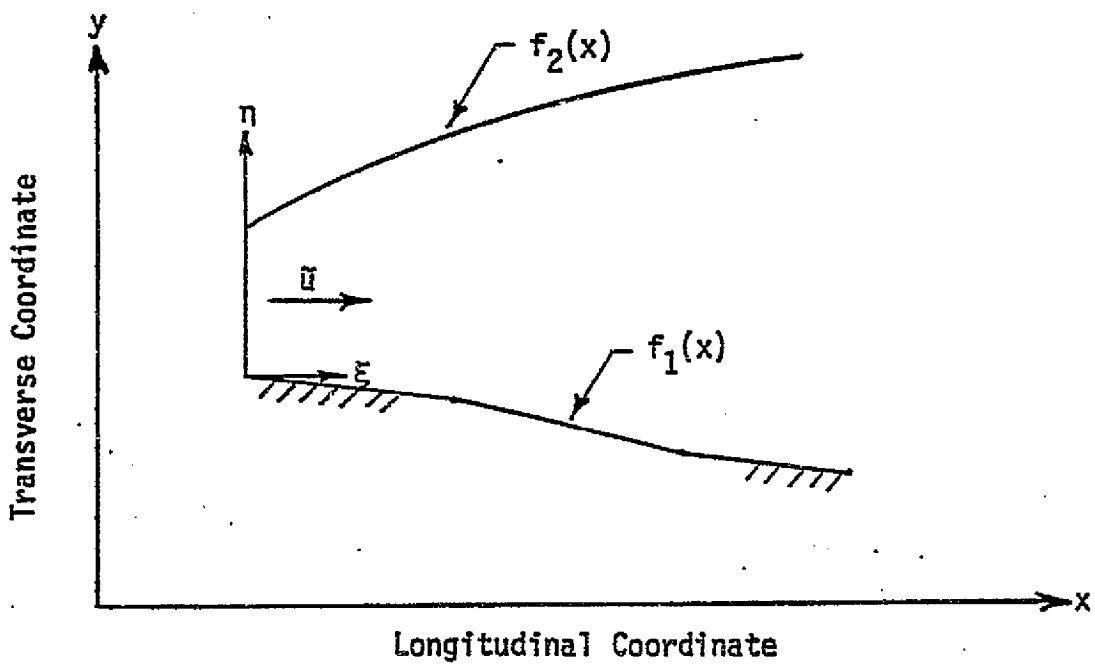

Figure 3. Transformed Coordinate System

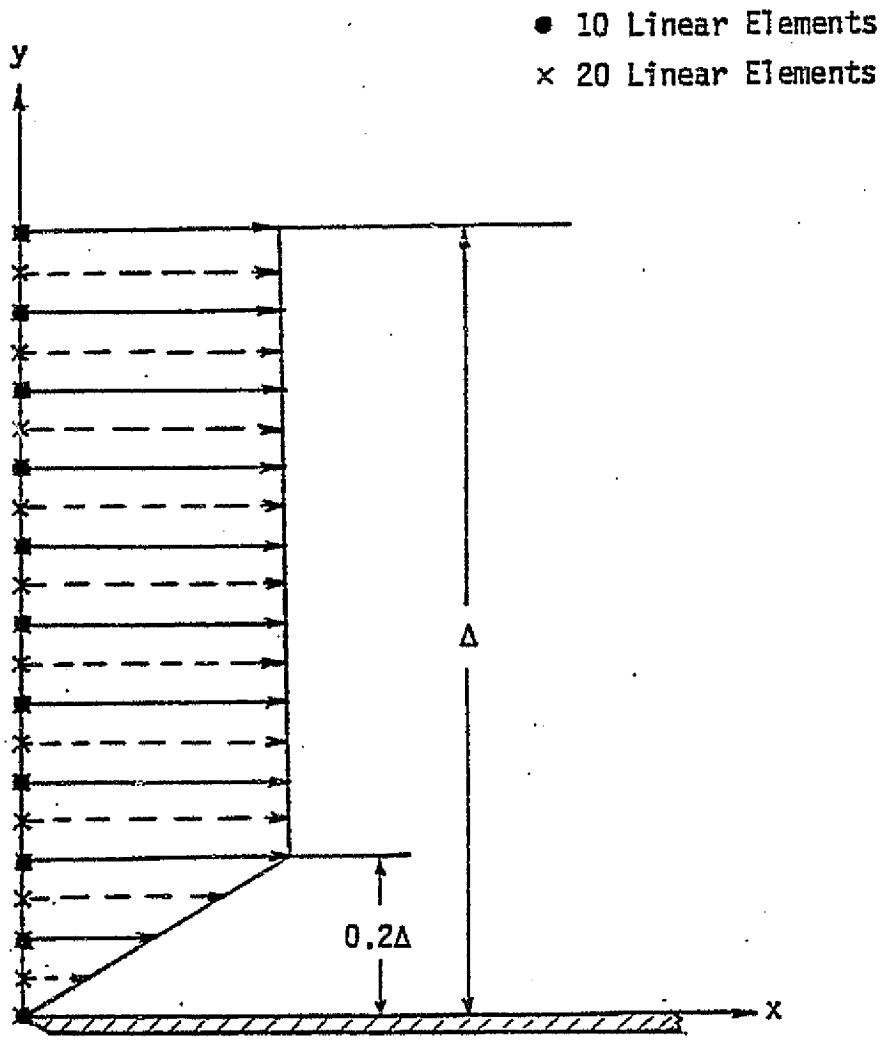

Figure 4. Slug Profile Used as Initial Condition for the Streamwise Velocity

ORIGINAL PAGE IS
OF POOR QUALITY

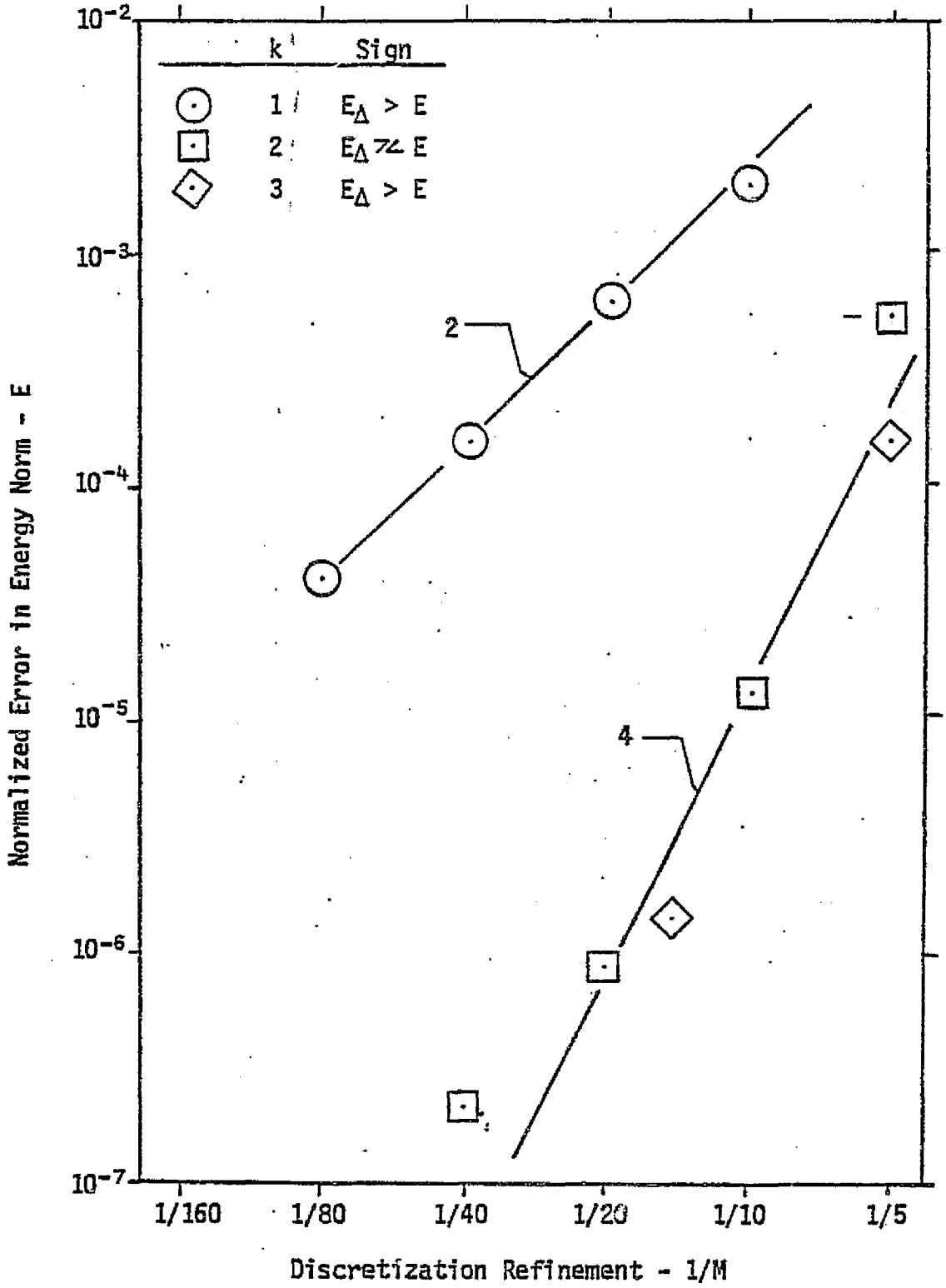

Figure 5. Accuracy and Convergence with Discretization Refinement in Energy Norm for a Parabolic Laminar Flow, Linear, Quadratic and Cubic Finite Elements

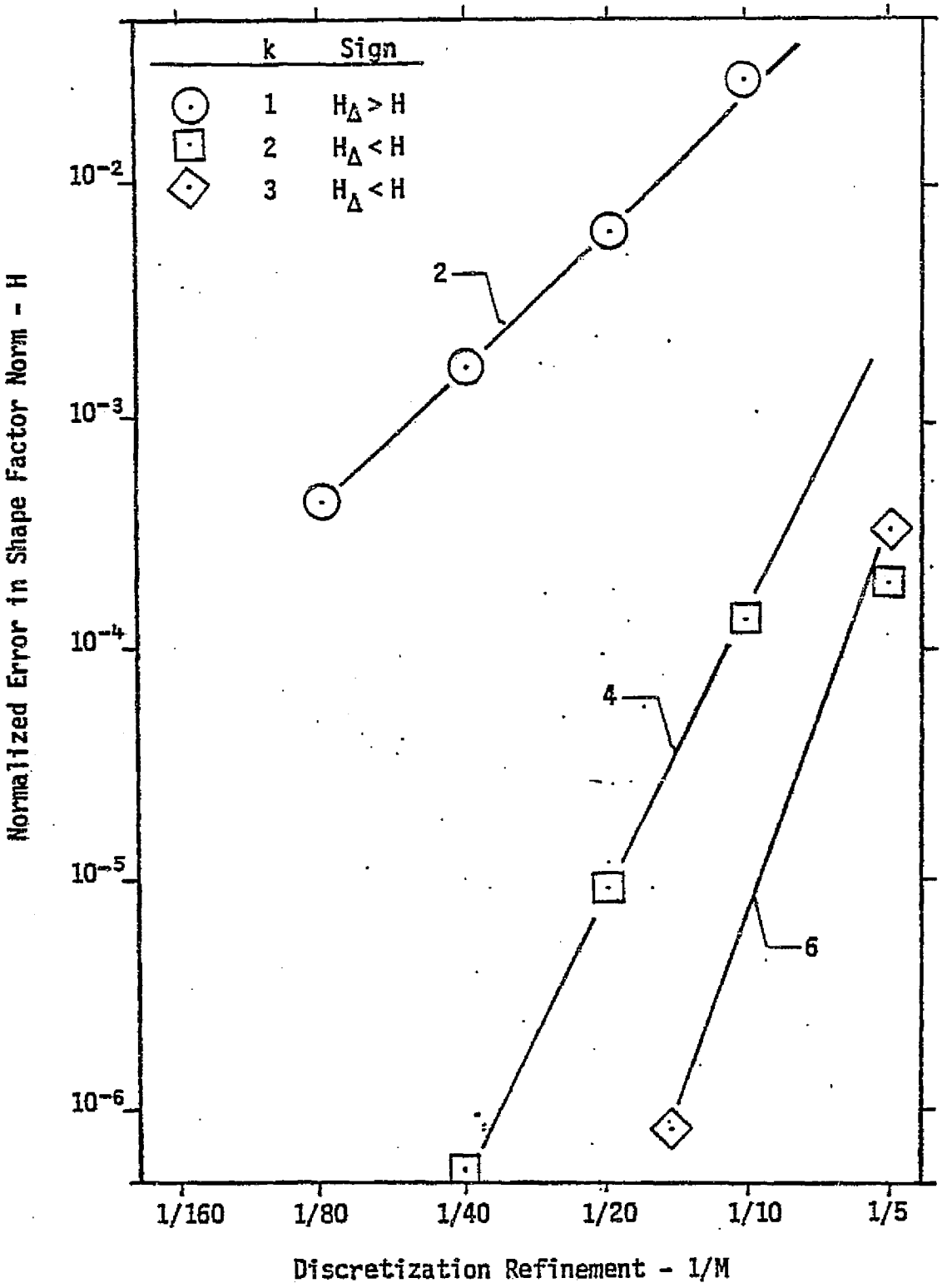

Figure 6. Accuracy and Convergence with Discretization Refinement in Shape Factor Norm for a Parabolic Laminar Flow, Linear, Quadratic and Cubic Finite Elements

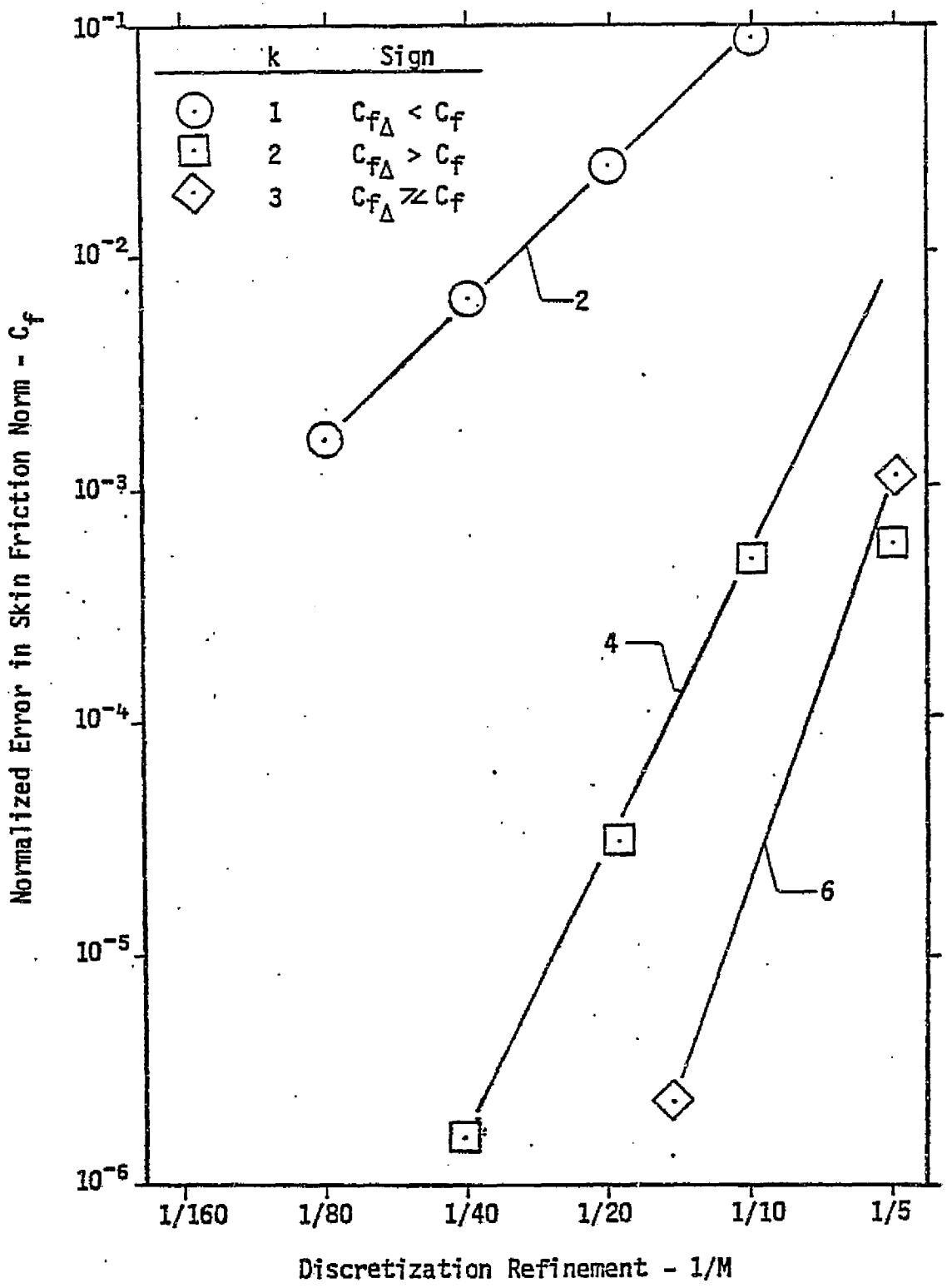

Figure 7. Accuracy and Convergence with Discretization Refinement in Skin Friction Norm for a Parabolic Laminar Flow, Linear, Quadratic and Cubic Finite Elements

ORIGINAL PAGE IS
OF POOR QUALITY

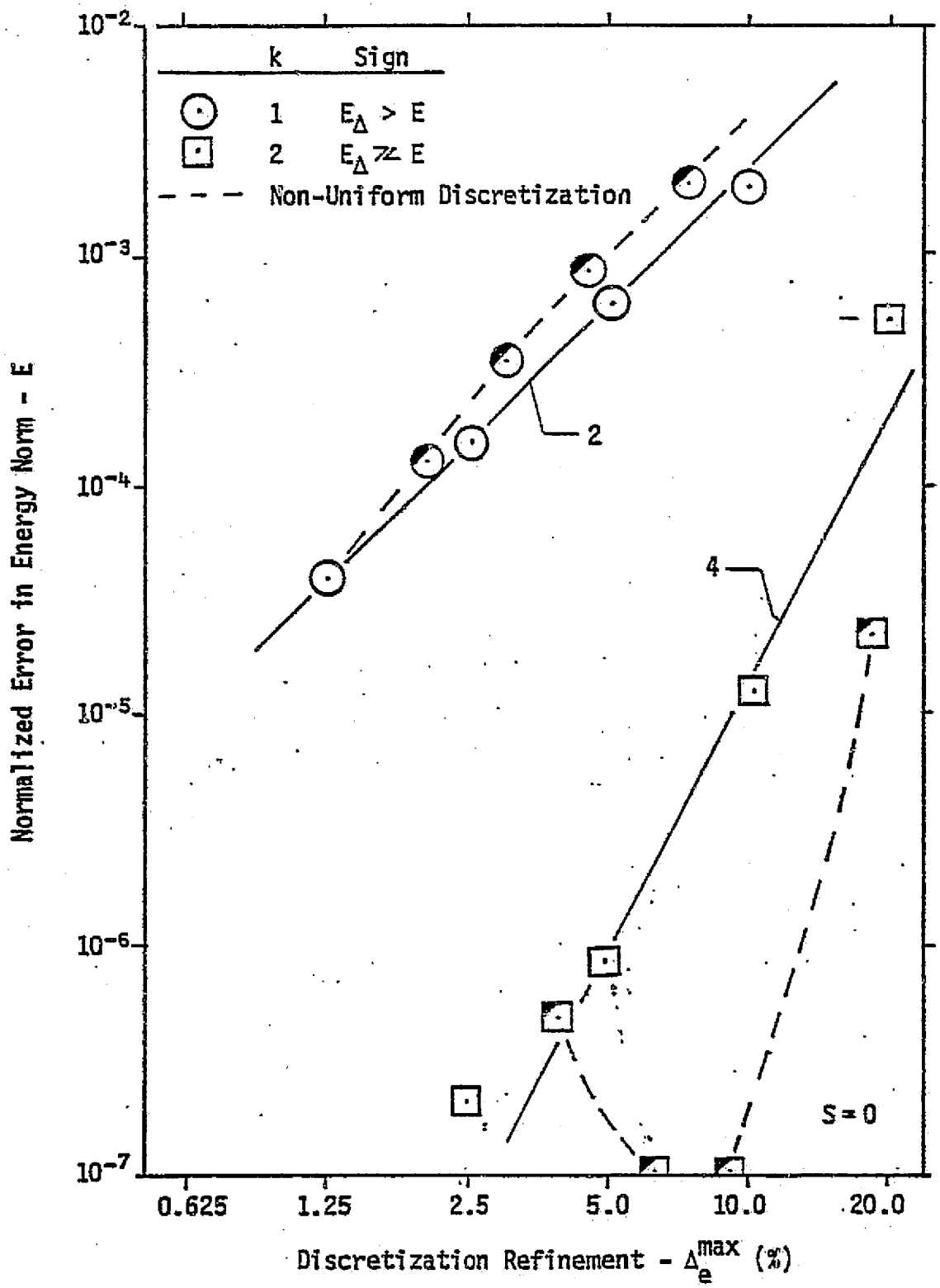

Figure 8. Accuracy and Convergence with Discretization Refinement in Energy Norm for a Parabolic Laminar Flow, Linear and Quadratic Finite Elements, Uniform and Non-Uniform Discretizations

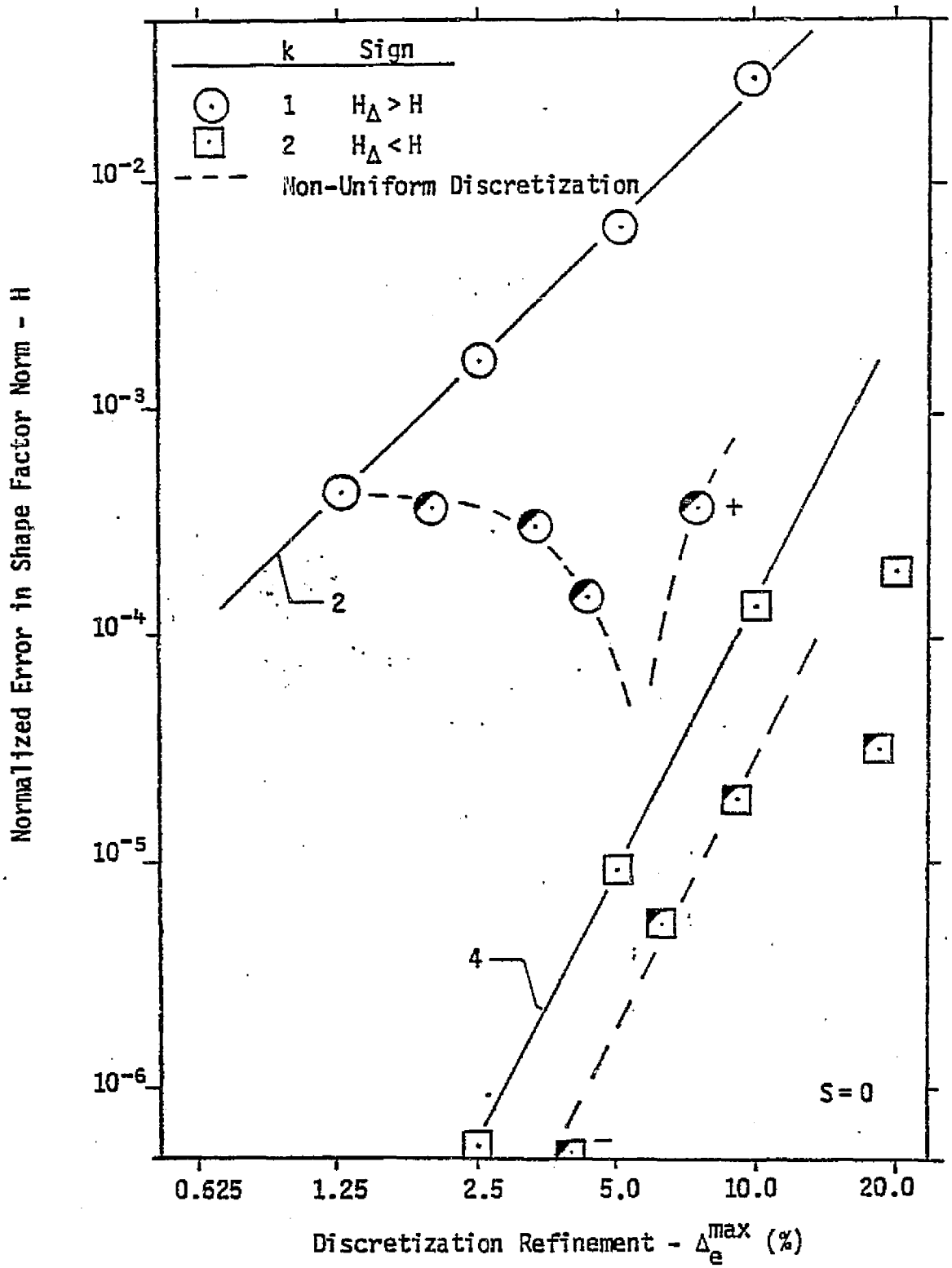

Figure 9. Accuracy and Convergence with Discretization Refinement in Shape Factor Norm for a Parabolic Laminar Flow, Linear and Quadratic Finite Elements, Uniform and Non-Uniform Discretizations

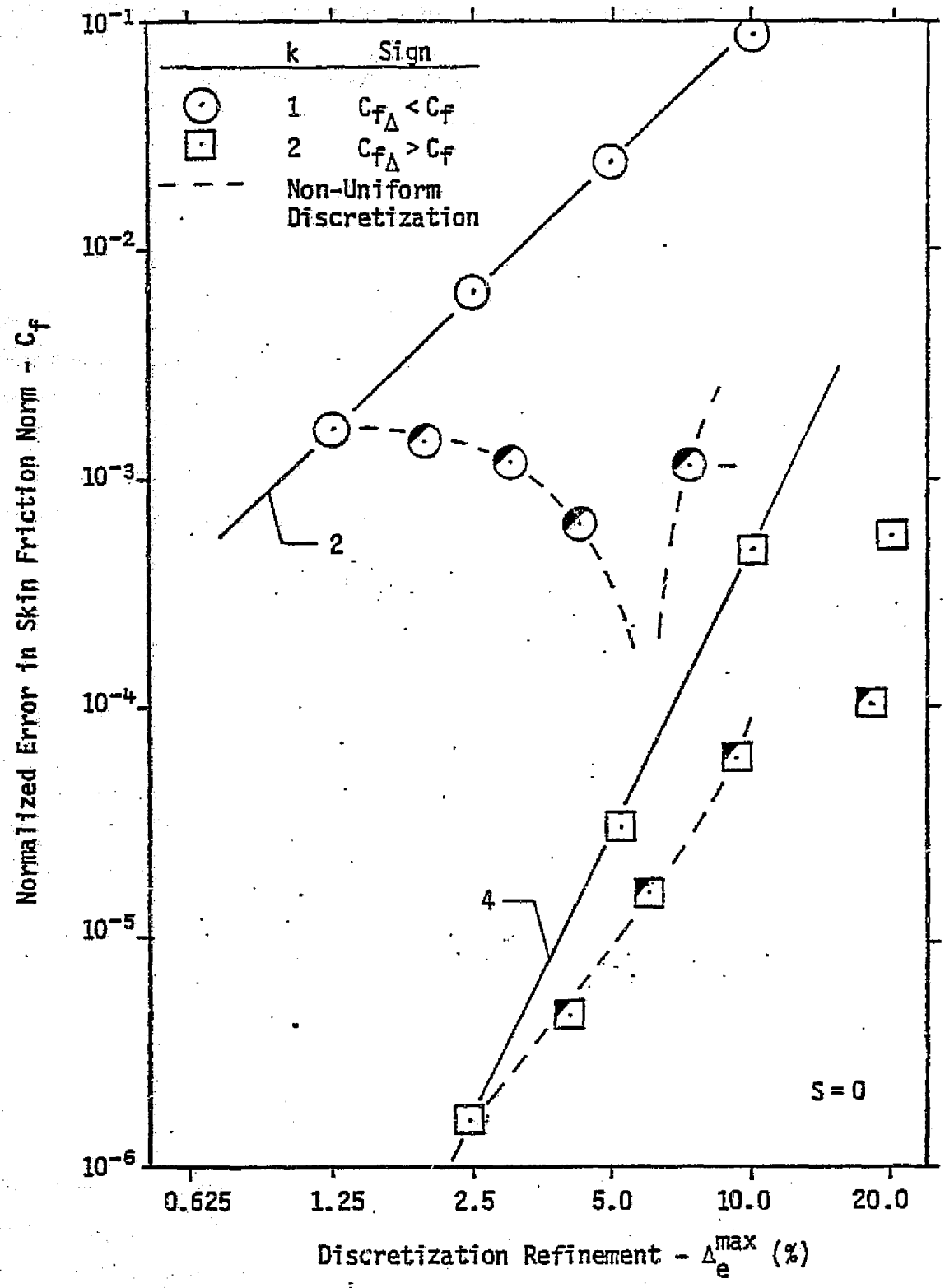

Figure 10. Accuracy and Convergence with Discretization Refinement in Skin Friction Norm for a Parabolic Laminar Flow, Linear and Quadratic Finite Elements, Uniform and Non-Uniform Discretizations

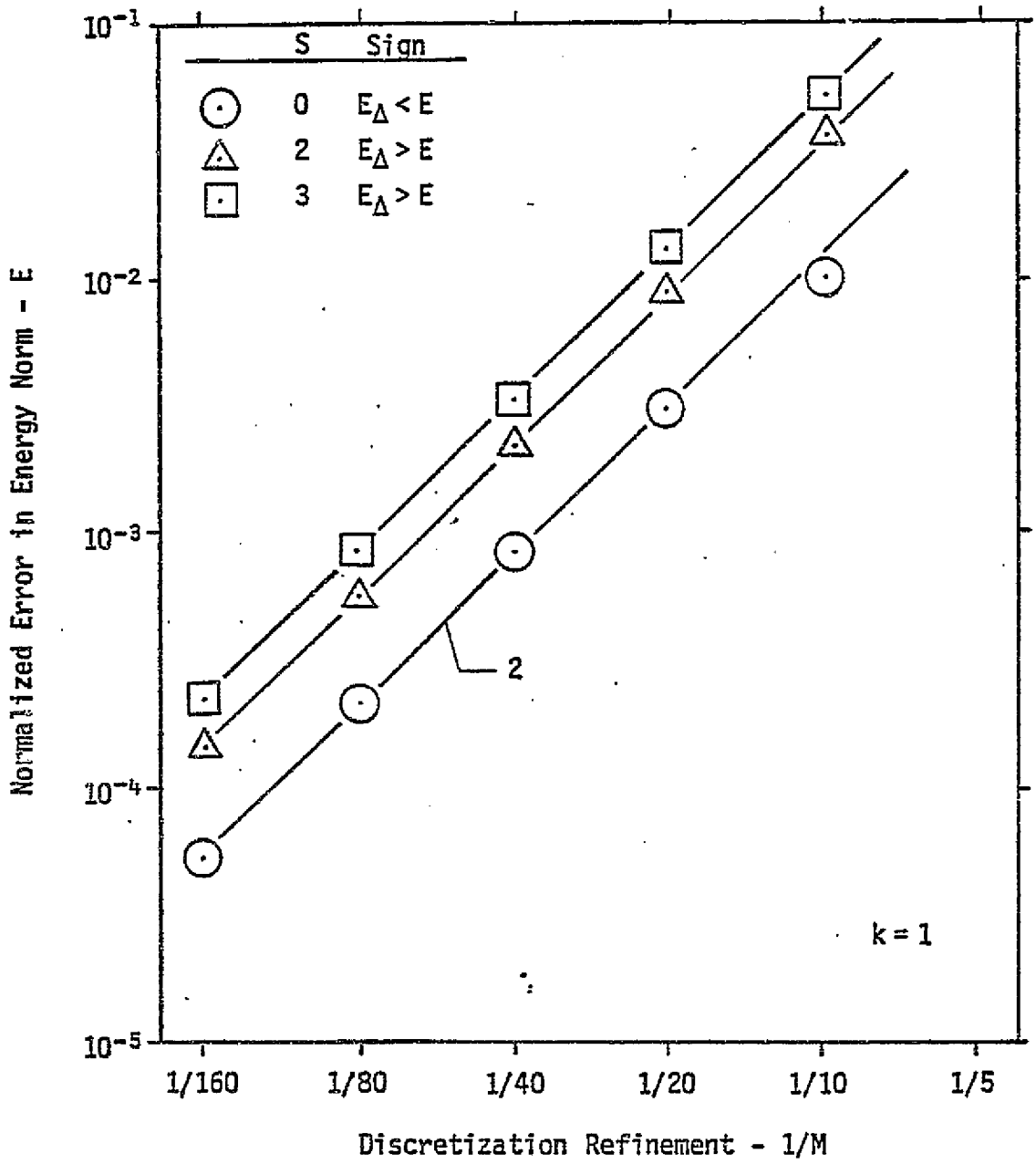

Figure 11. Accuracy and Convergence with Discretization Refinement in Energy Norm, Laminar Boundary Layer, Linear Elements

ORIGINAL PAGE IS
OF POOR QUALITY

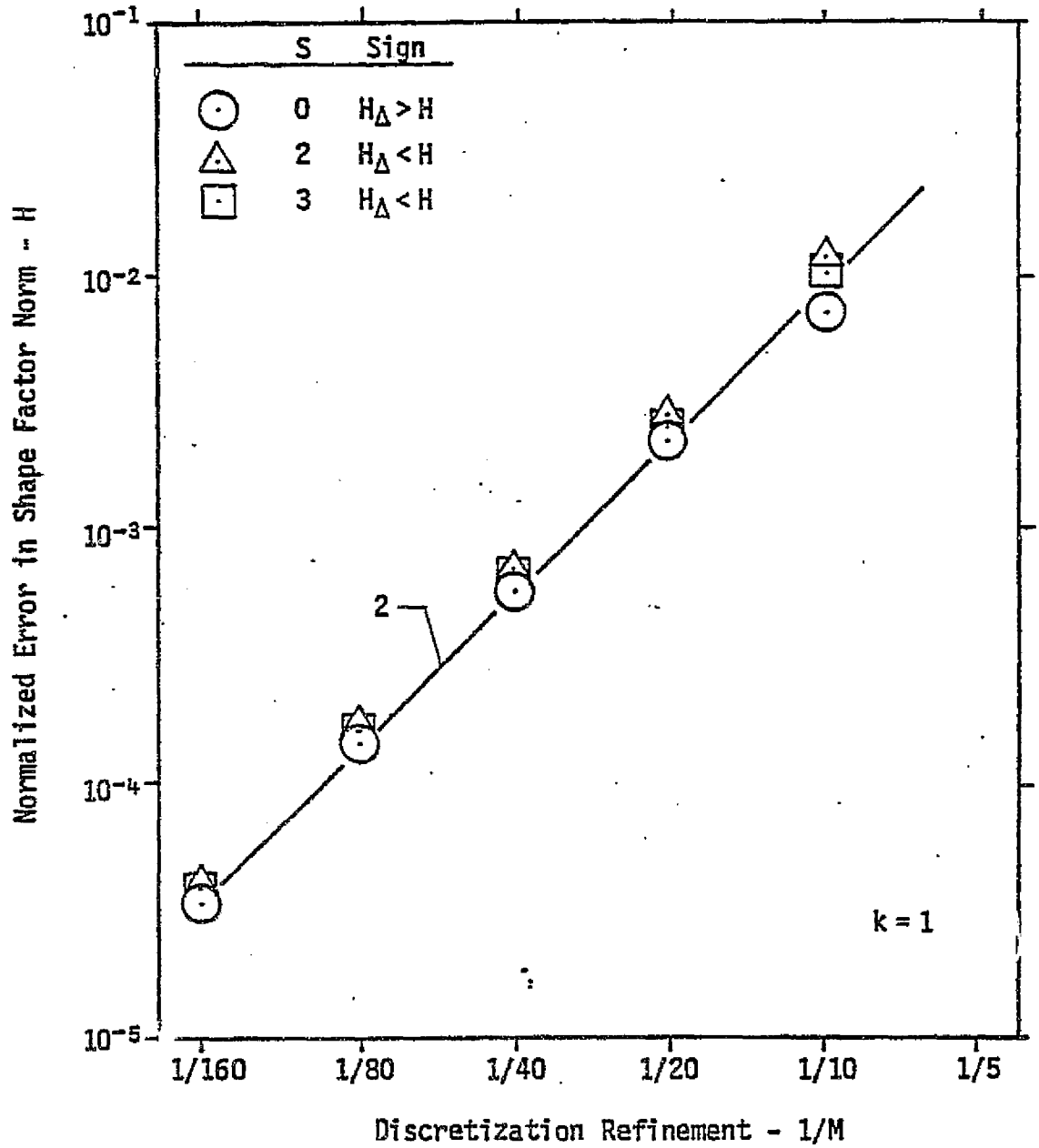

Figure 12. Accuracy and Convergence with Discretization Refinement in Shape Factor Norm, Laminar Boundary Layer, Linear Elements

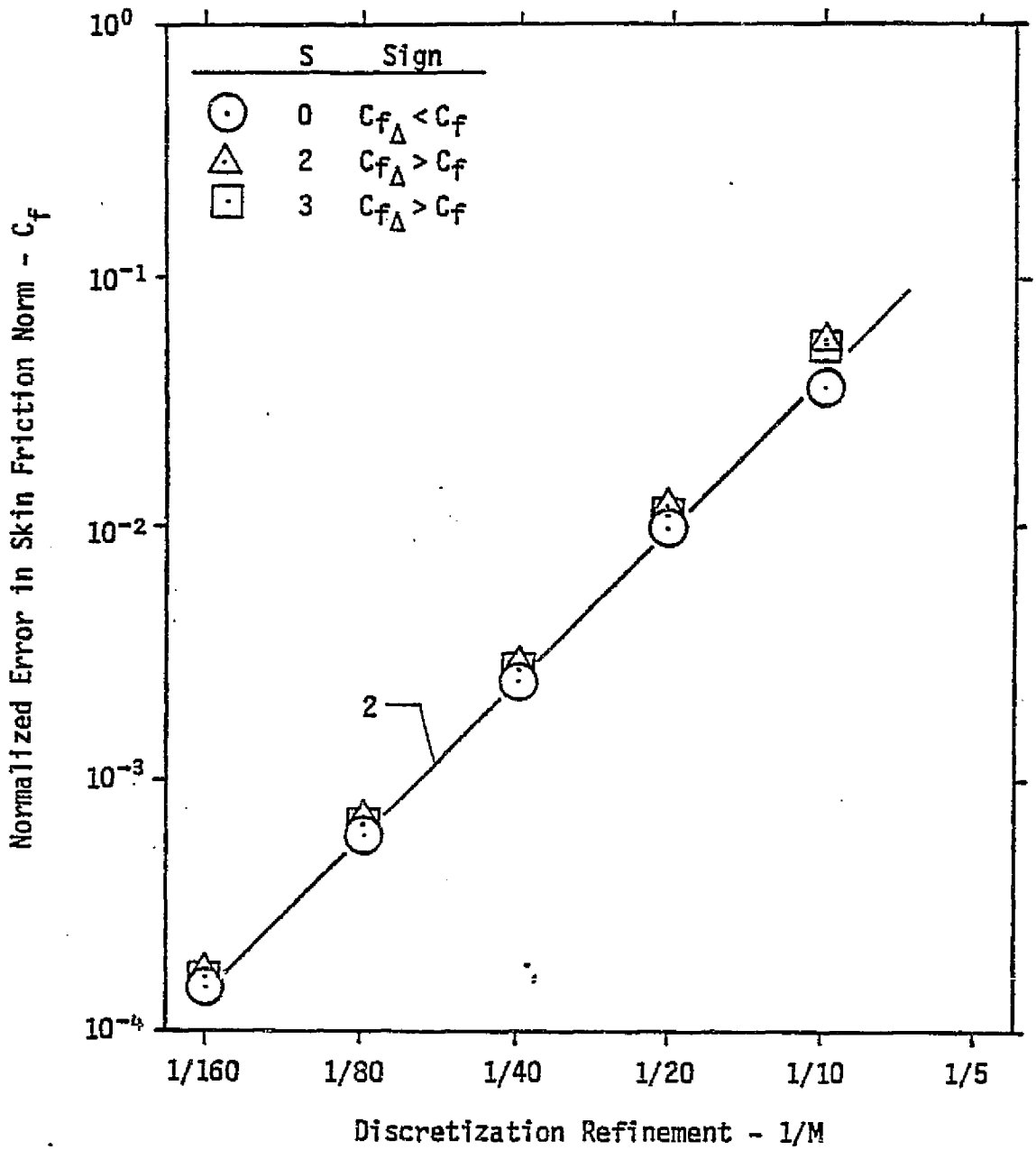

Figure 13. Accuracy and Convergence with Discretization Refinement in Skin Friction Norm, Laminar Boundary Layer, Linear Elements

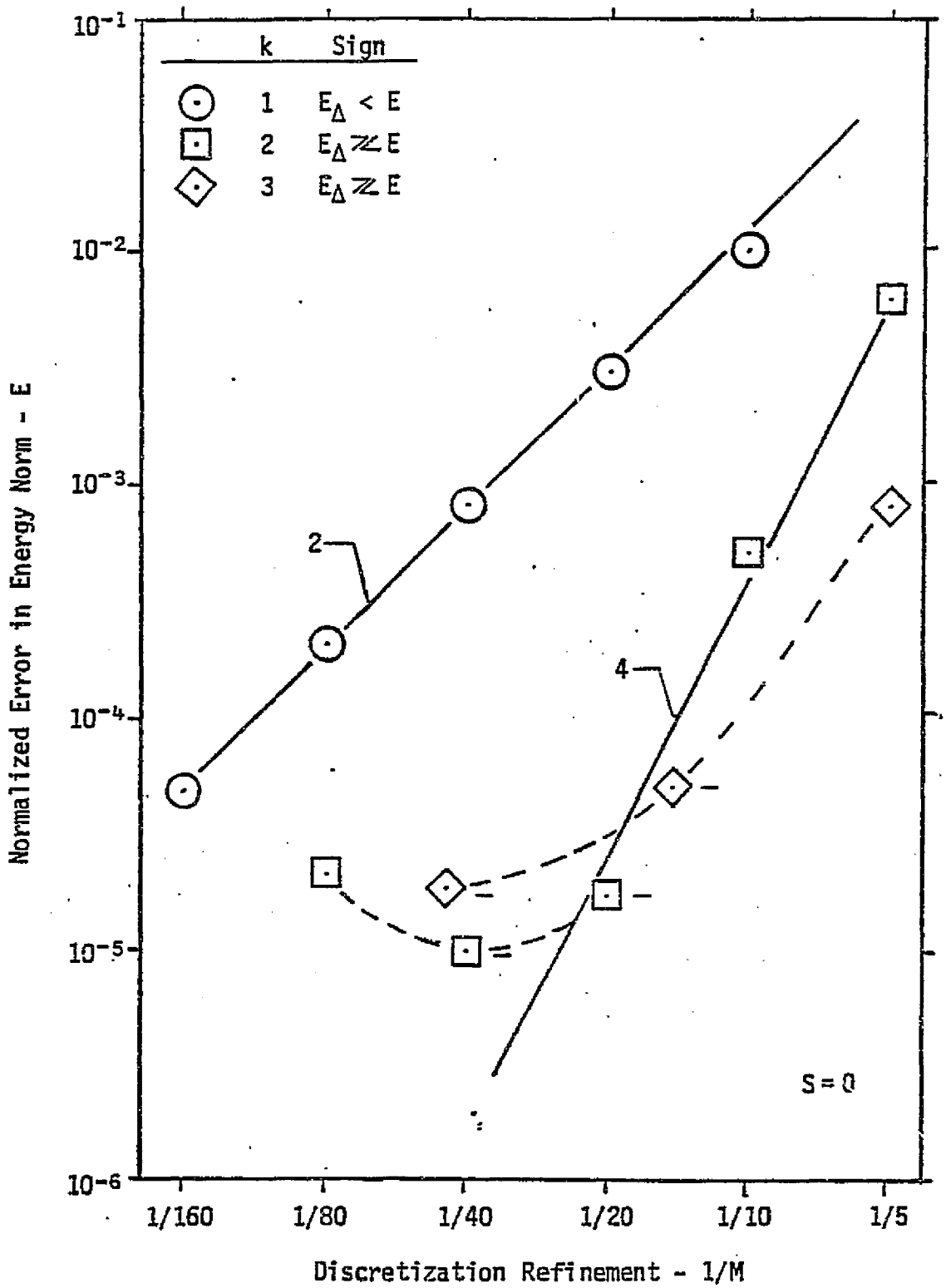

Figure 14. Accuracy and Convergence with Discretization Refinement in Energy Norm, Laminar Boundary Layer, Linear, Quadratic and Cubic Finite Elements

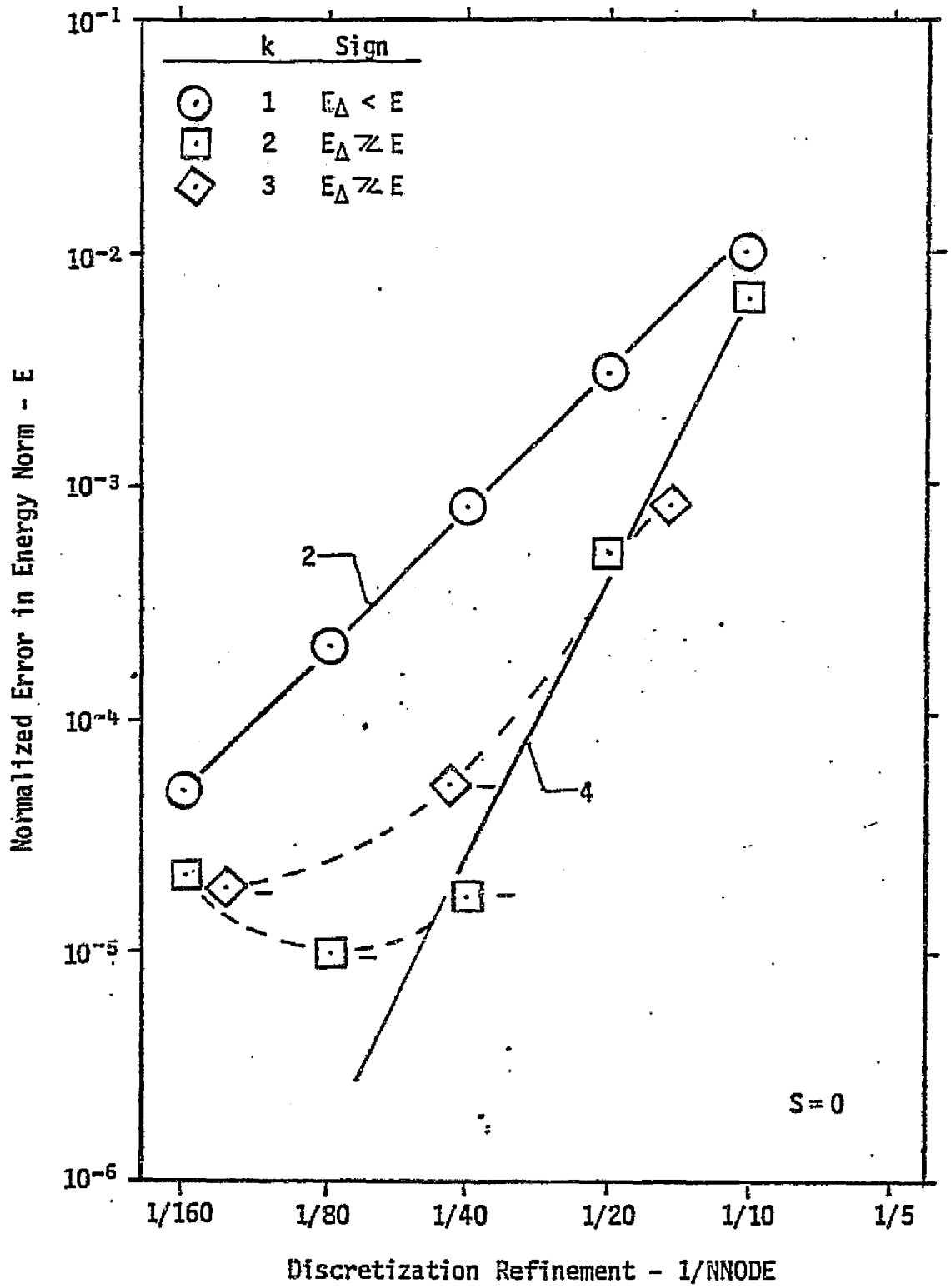

Figure 15. Accuracy and Convergence with Discretization Refinement (Number of Nodes) in Energy Norm, Laminar Boundary Layer, Linear, Quadratic and Cubic Finite Elements

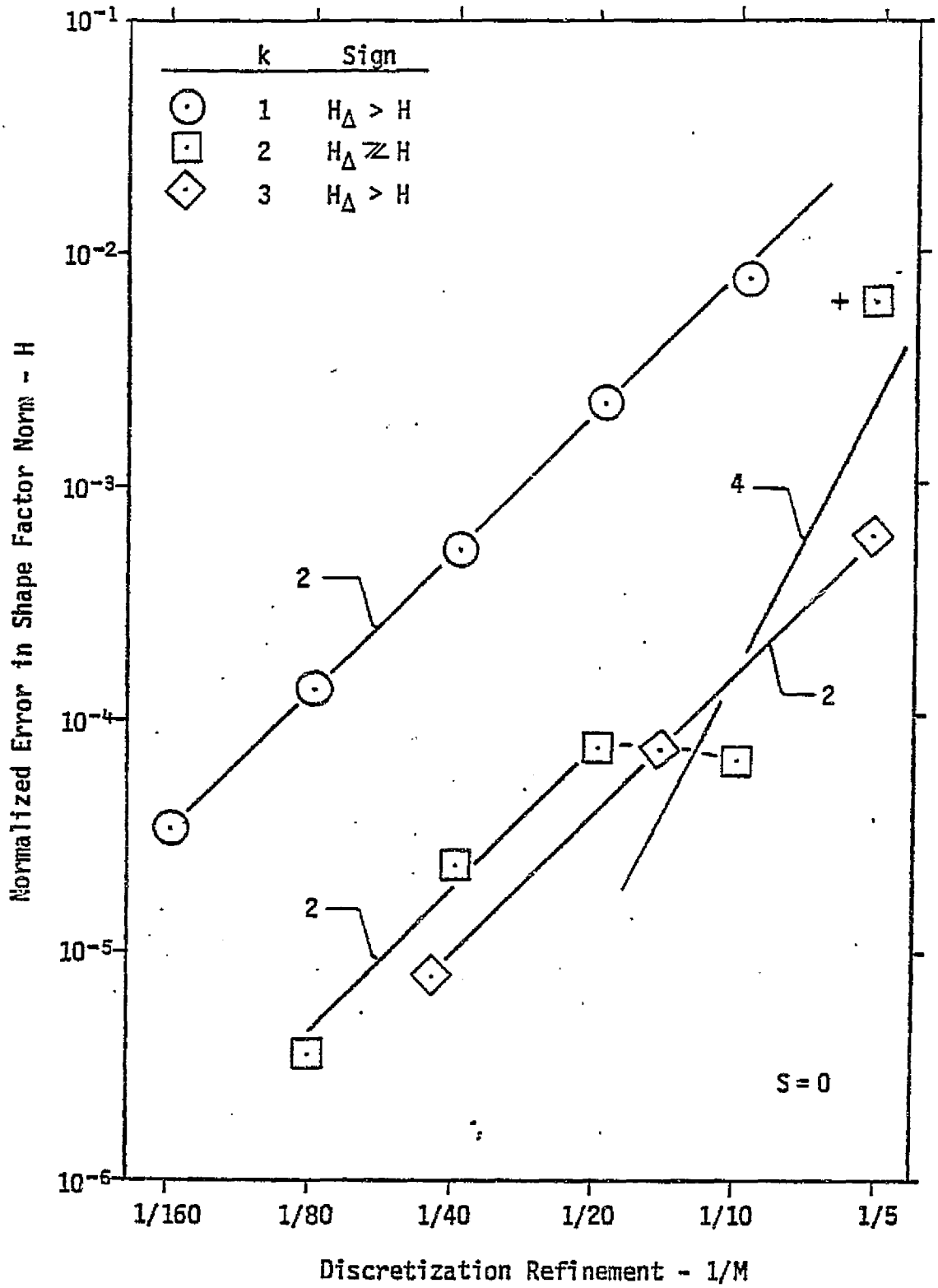

Figure 16. Accuracy and Convergence with Discretization Refinement in Shape Factor Norm, Laminar Boundary Layer, Linear, Quadratic and Cubic Finite Elements

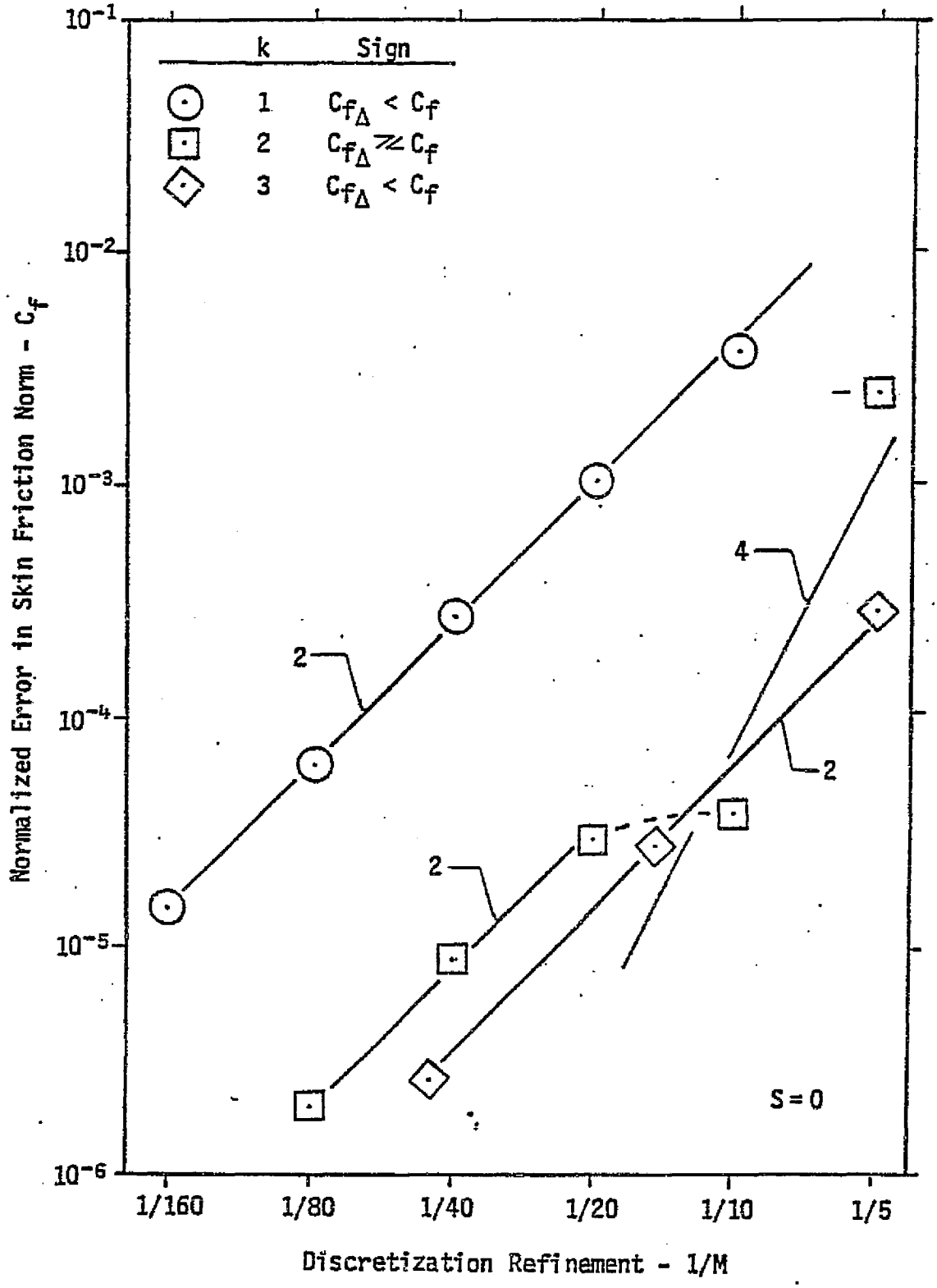

Figure 17. Accuracy and Convergence with Discretization Refinement in Skin Friction Norm, Laminar Boundary Layer, Linear, Quadratic and Cubic Finite Elements

ORIGINAL PAGE IS
OF POOR QUALITY

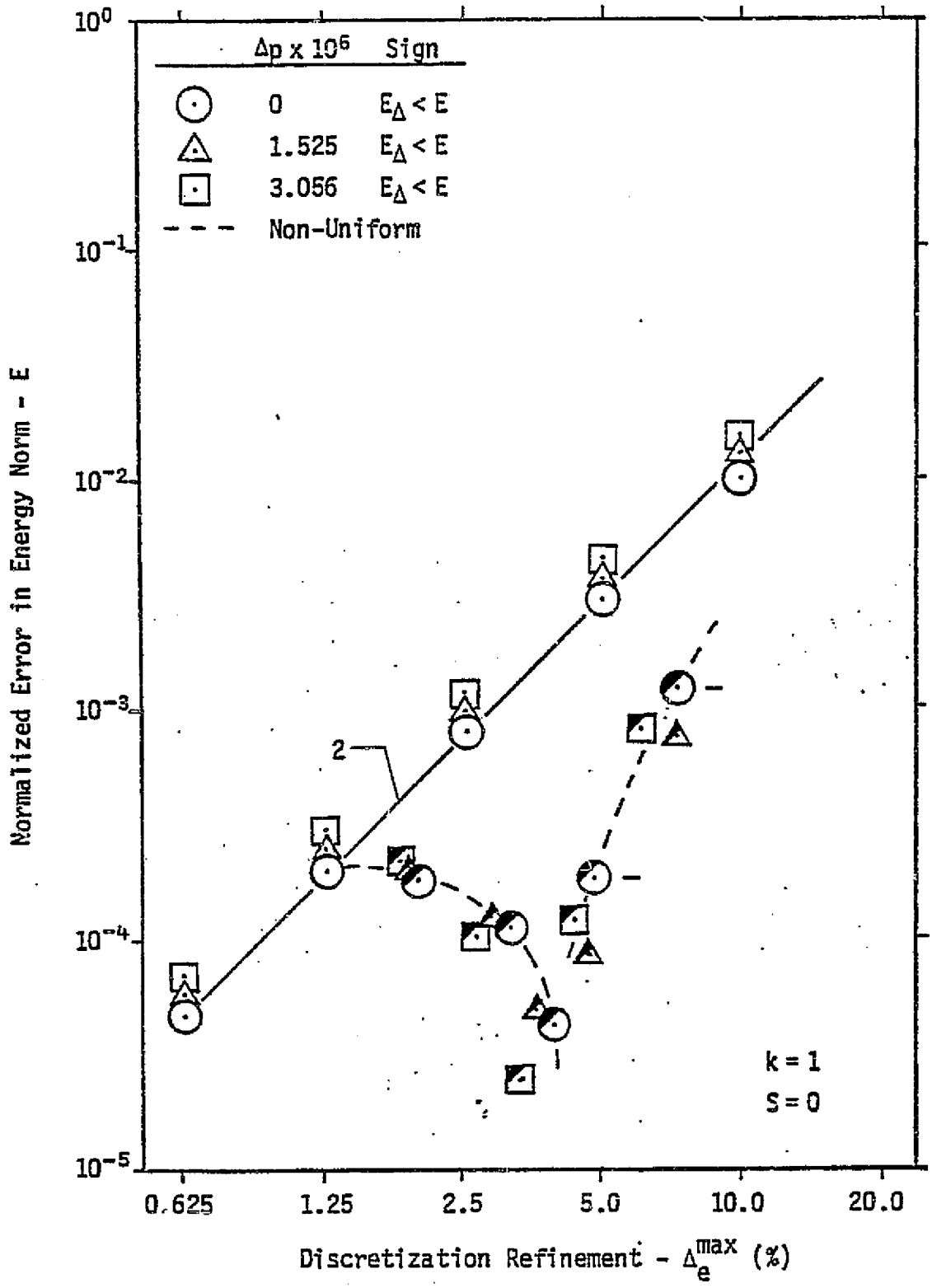

Figure 18. Accuracy and Convergence with Discretization Refinement in Energy Norm, Laminar Boundary Layer, with Pressure Gradient, Linear Finite Elements, Consistent Assembly

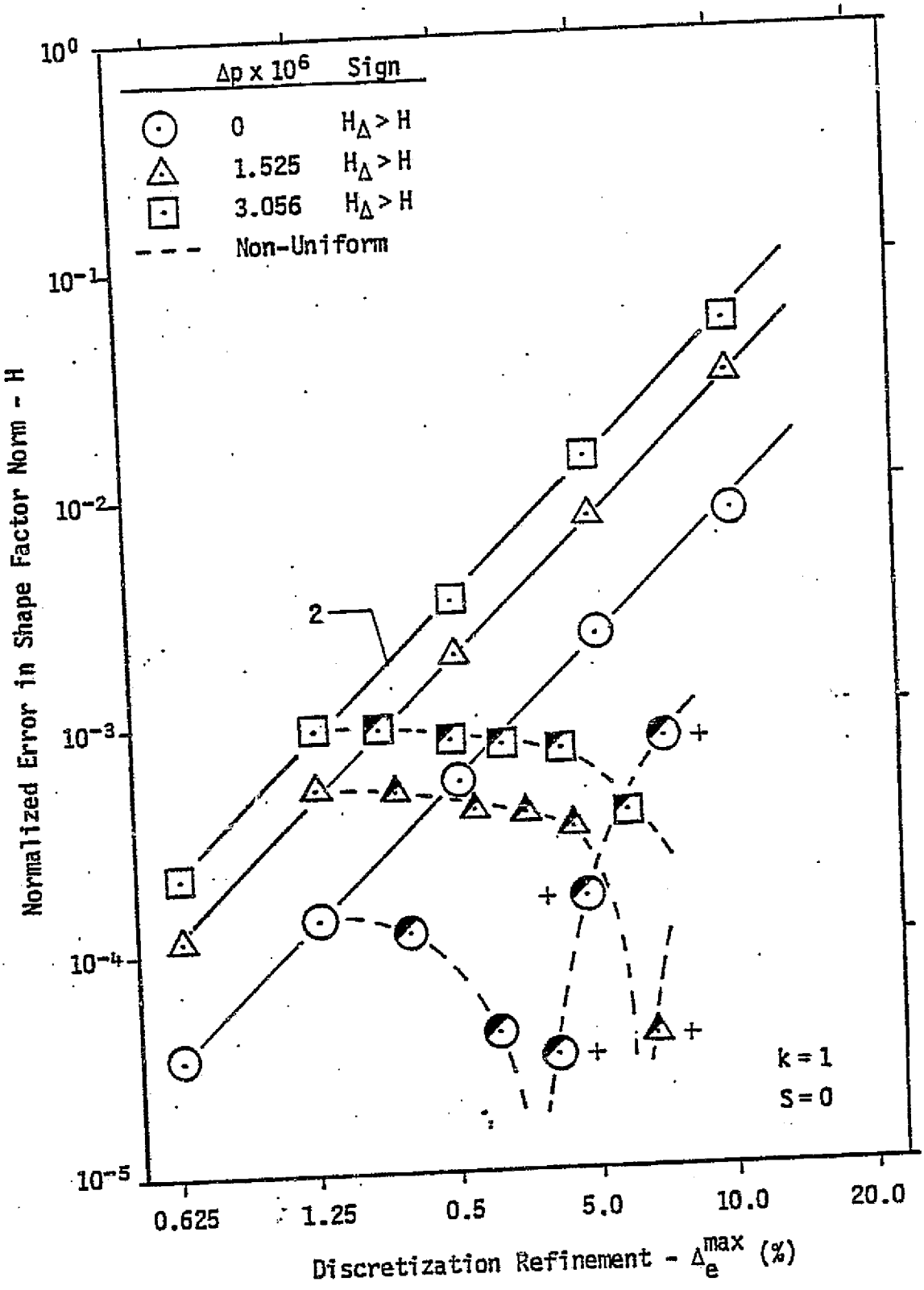

Figure 19. Accuracy and Convergence with Discretization Refinement in Shape Factor Norm, Laminar Boundary Layer, with Pressure Gradient, Linear Finite Elements, Consistent Assembly

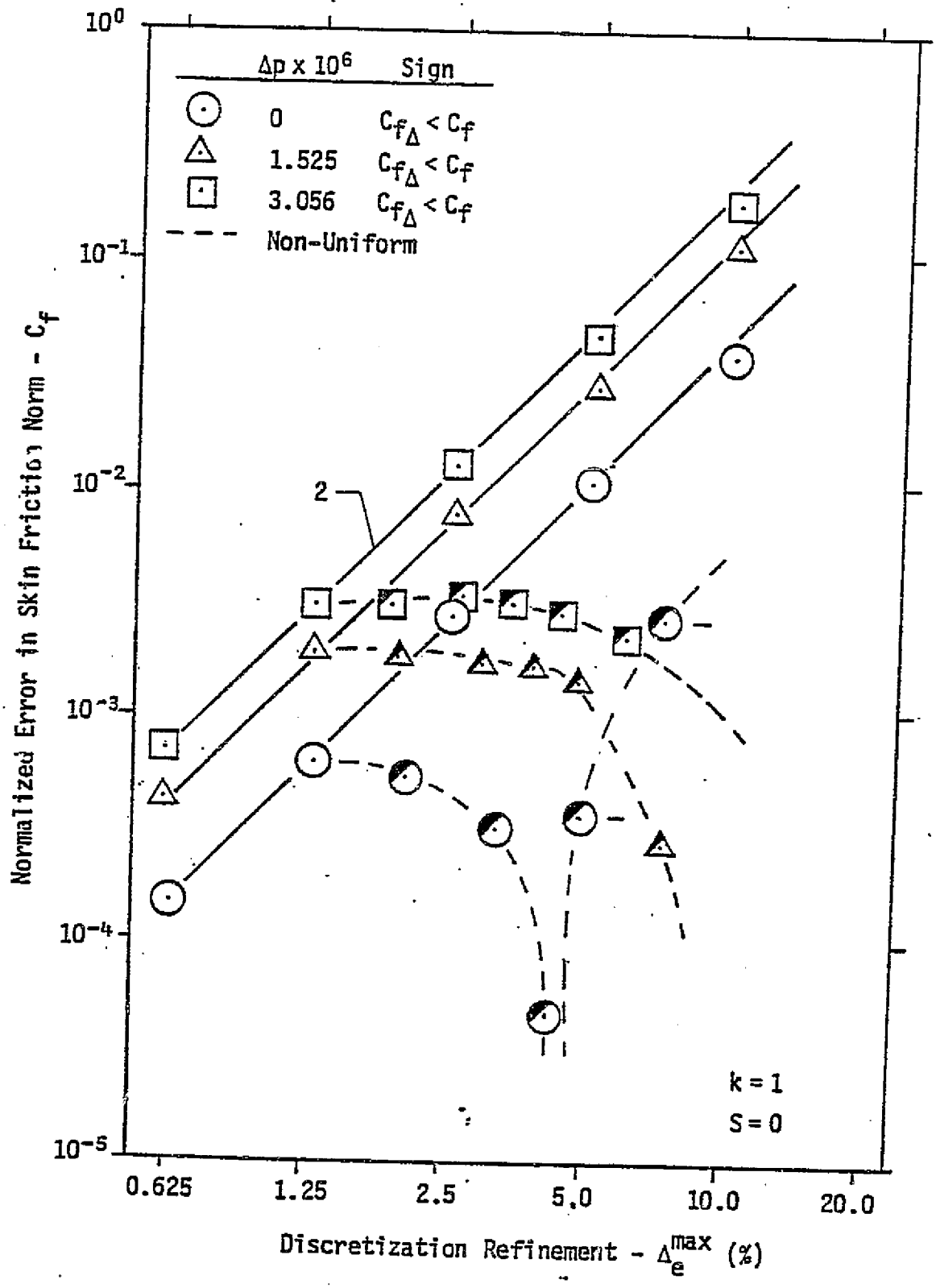

Figure 20. Accuracy and Convergence with Discretization Refinement in Skin Friction Norm, Laminar Boundary Layer with Pressure Gradient, Linear Finite Elements, Consistent Assembly

ORIGINAL PAGE IS
OF POOR QUALITY

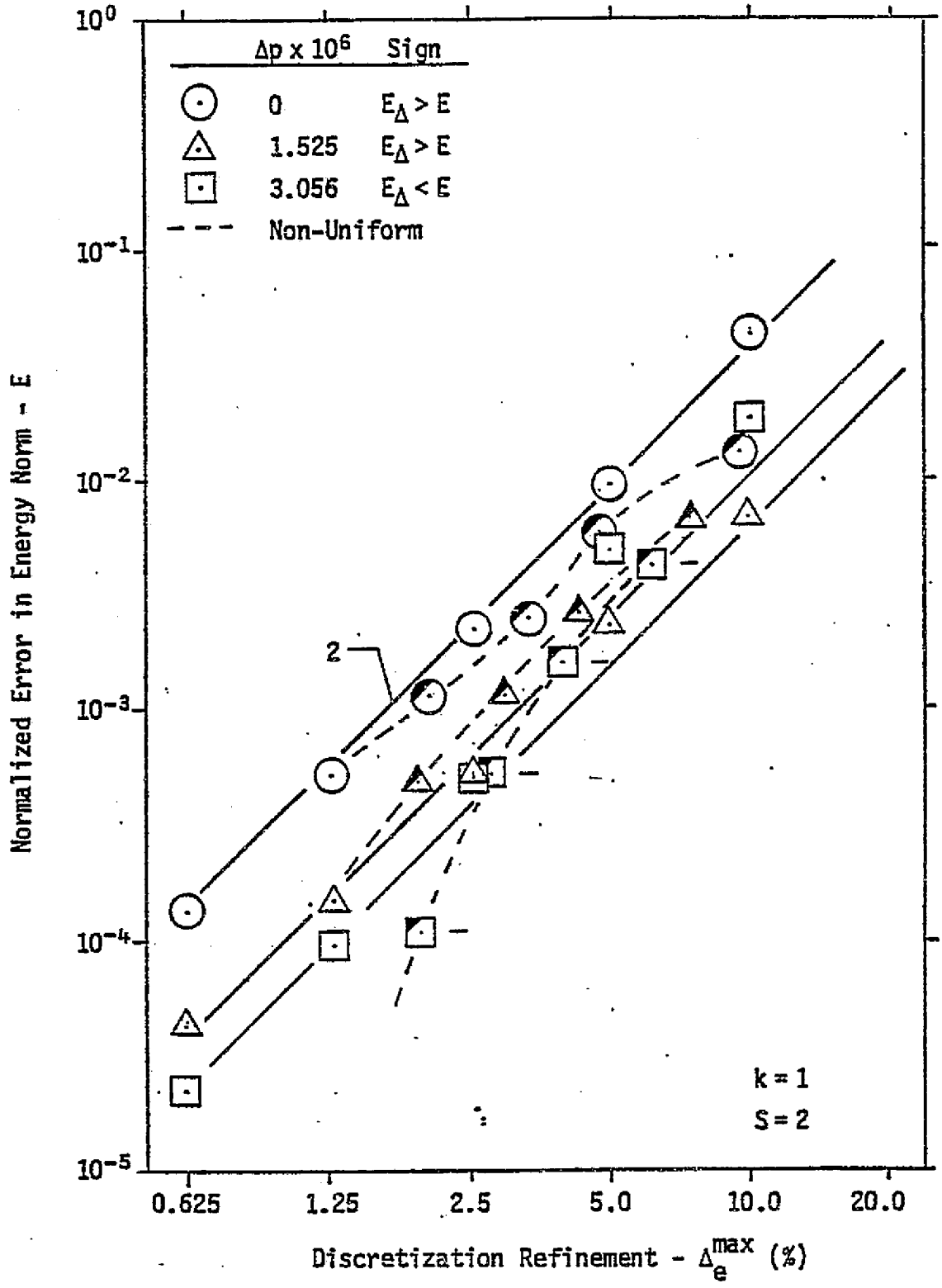

Figure 21. Accuracy and Convergence with Discretization Refinement in Energy Norm, Laminar Boundary Layer with Pressure Gradient, Linear Elements, Diagonalized Initial-Value Matrix

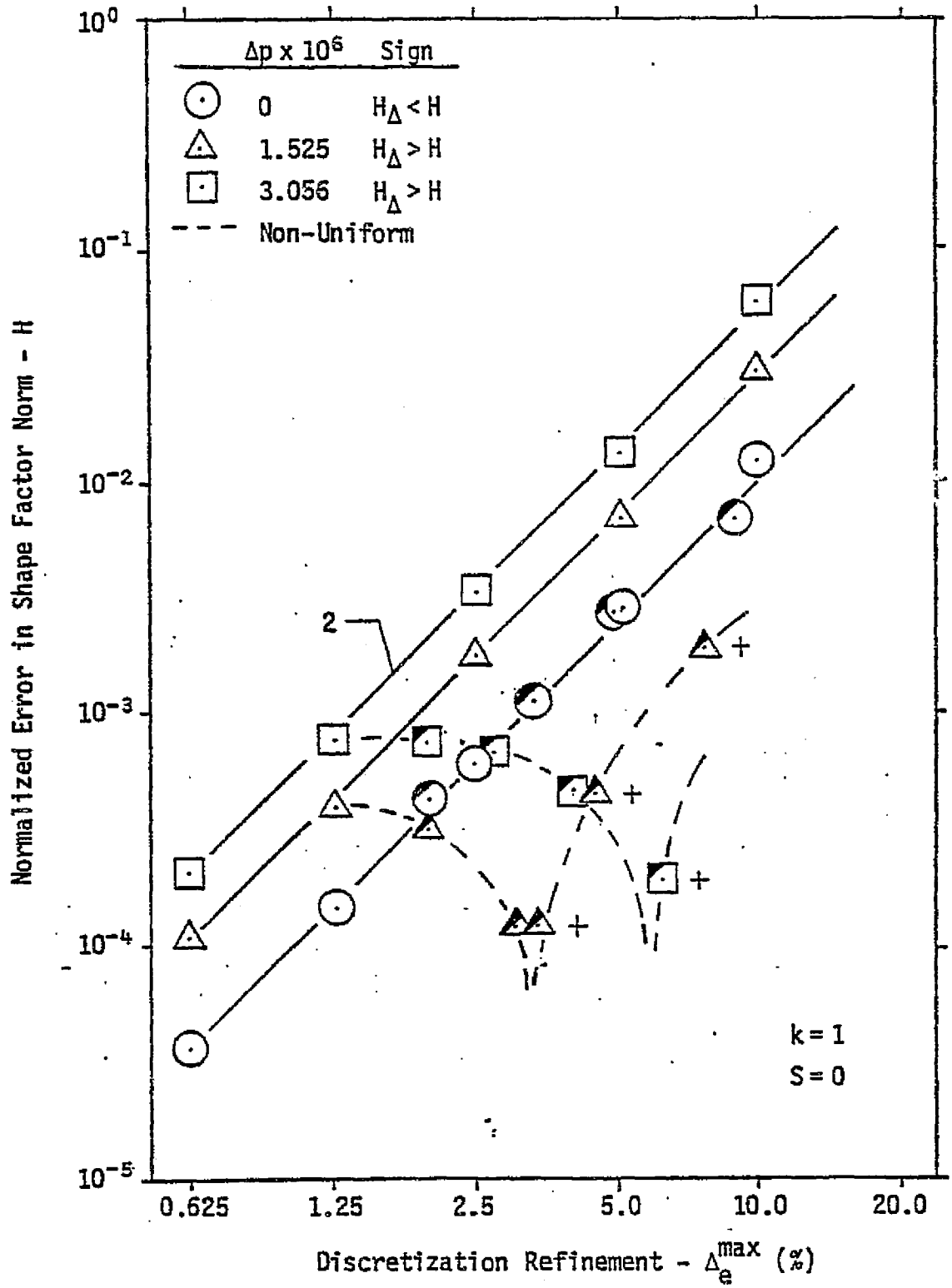

Figure 22. Accuracy and Convergence with Discretization Refinement in Shape Factor Norm, Laminar Boundary Layer with Pressure Gradient, Linear Elements, Diagonalized Initial-Value Matrix

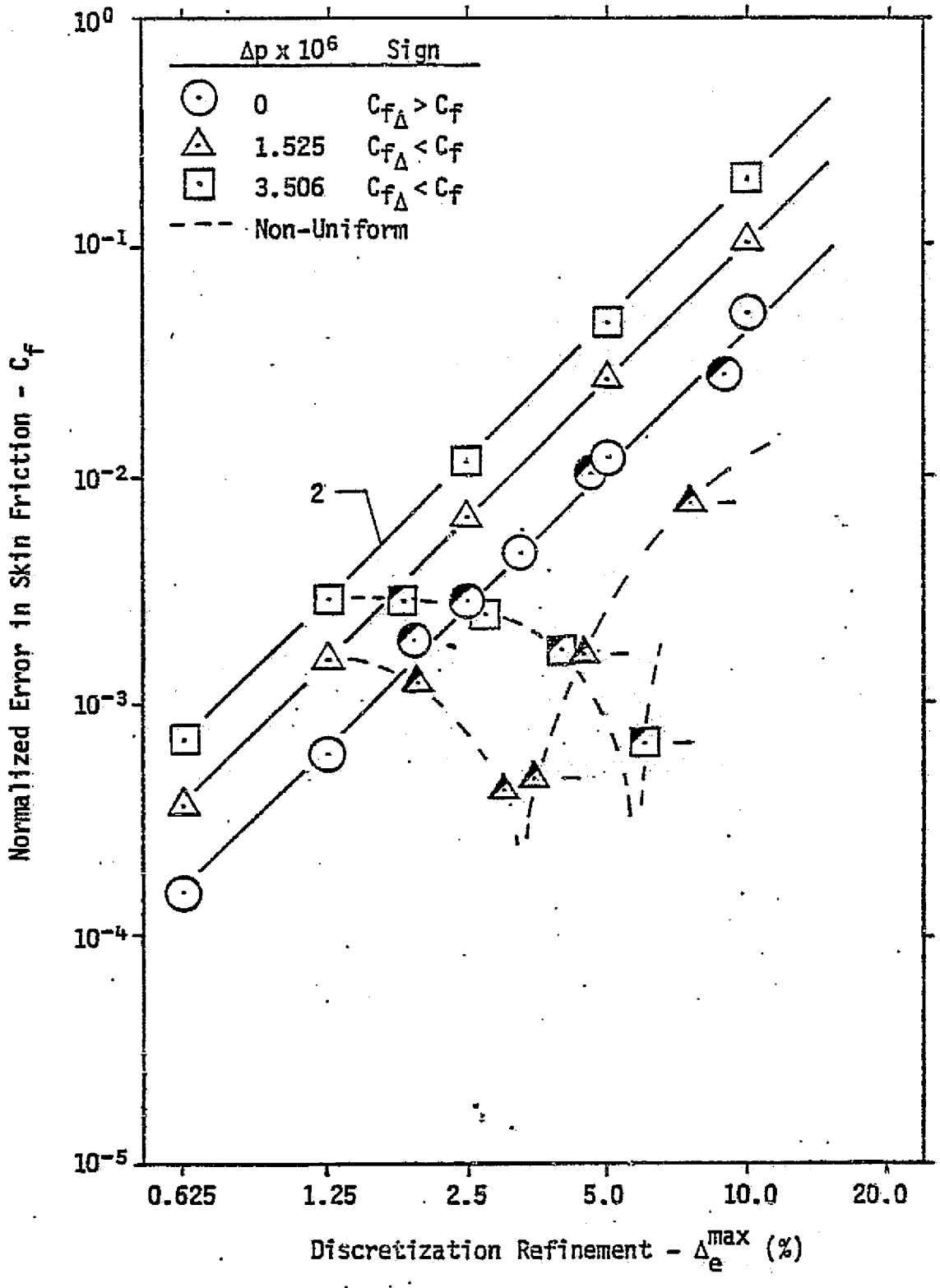

Figure 23. Accuracy and Convergence with Discretization Refinement in Skin Friction Norm, Laminar Boundary Layer with Pressure Gradient, Linear Elements, Diagonalized Initial-Value Matrix

ORIGINAL PAGE IS
OF POOR QUALITY

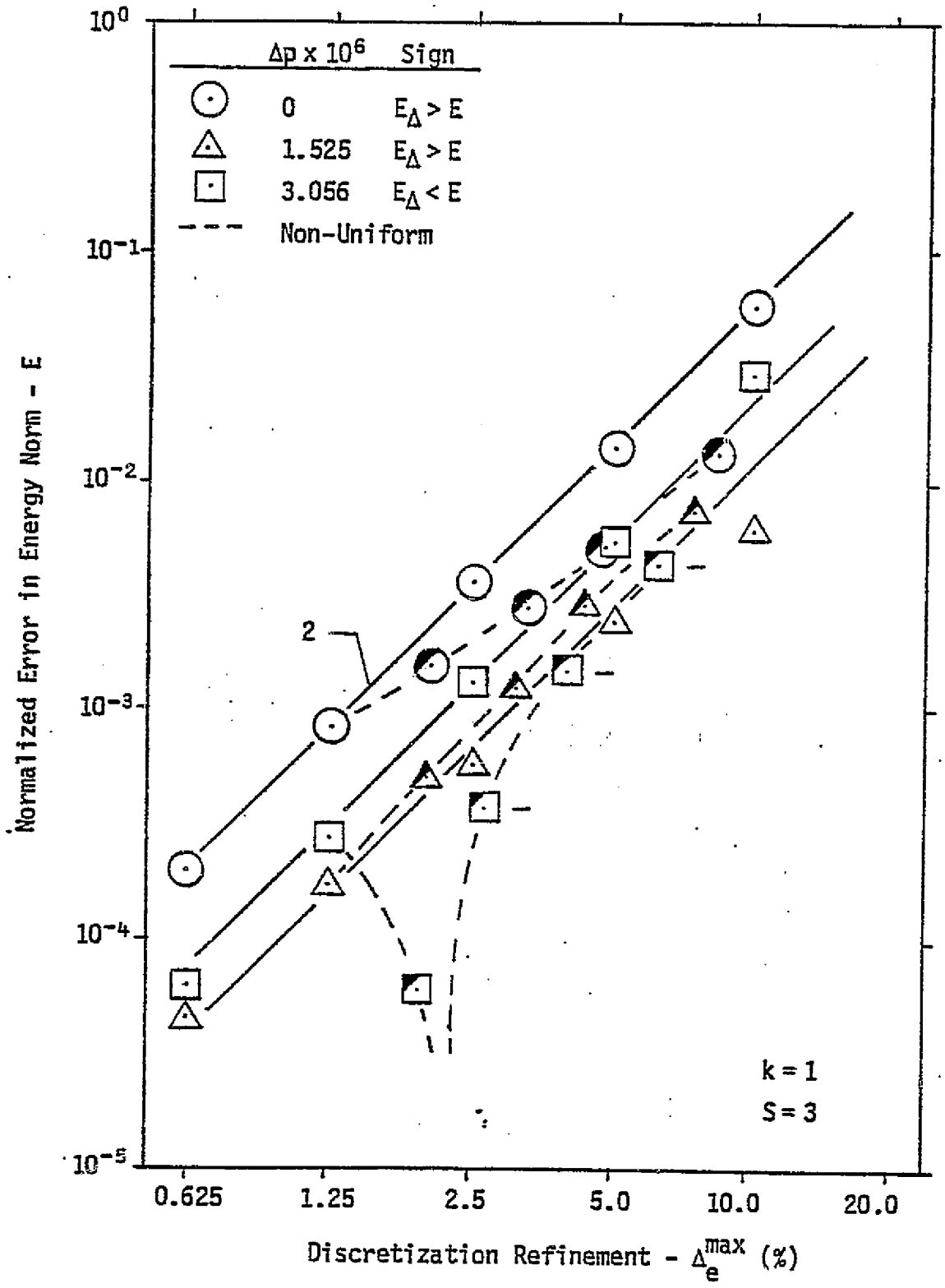

Figure 24. Accuracy and Convergence with Discretization Refinement in Energy Norm, Laminar Boundary Layer with Pressure Gradient, Linear Elements, Finite Difference Initial-Value Matrix

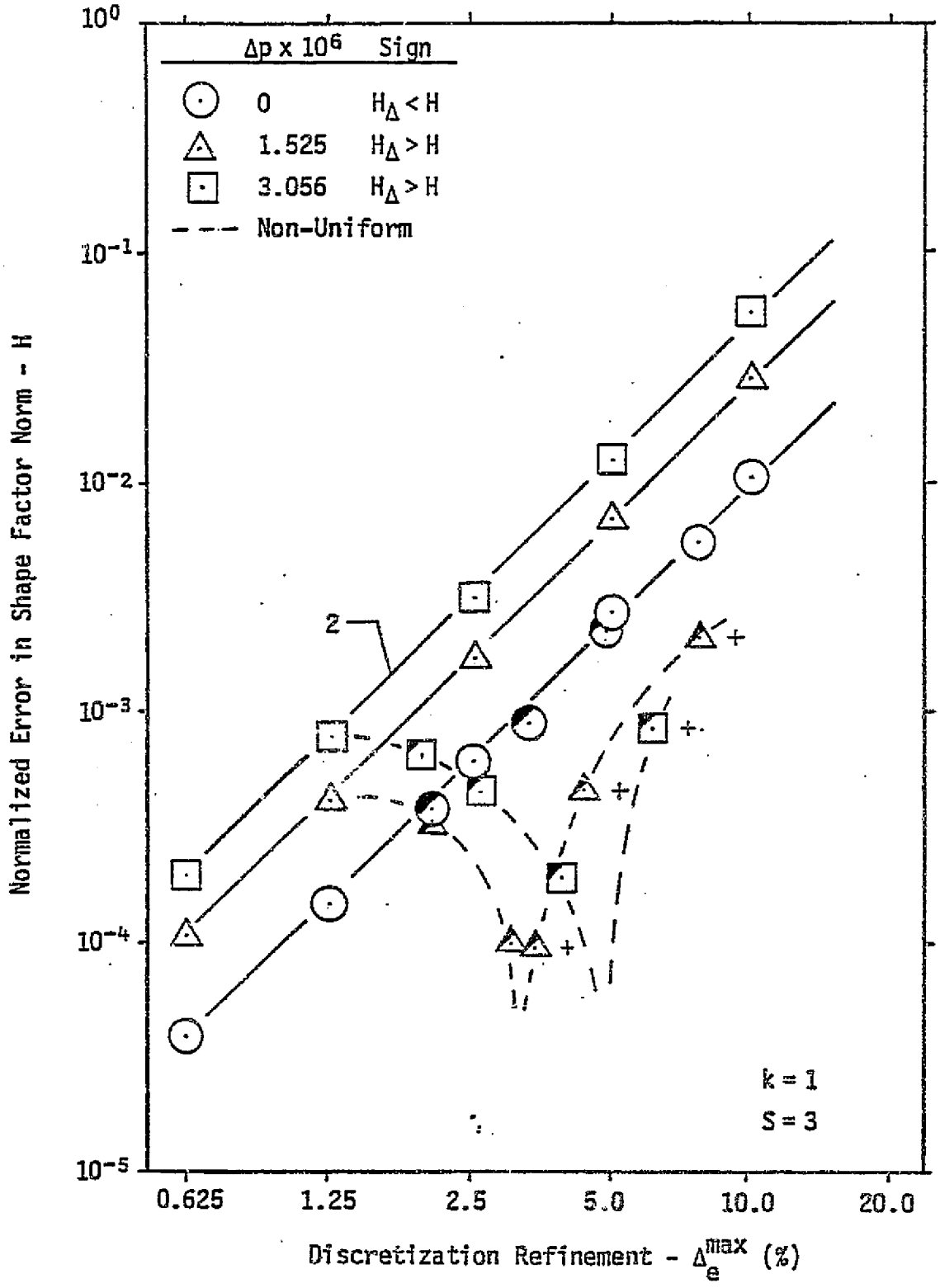

Figure 25. Accuracy and Convergence with Discretization Refinement in Shape Factor Norm, Laminar Boundary Layer with Pressure Gradient, Linear Elements, Finite Difference Initial-Value Matrix

ORIGINAL PAGE IS
OF POOR QUALITY

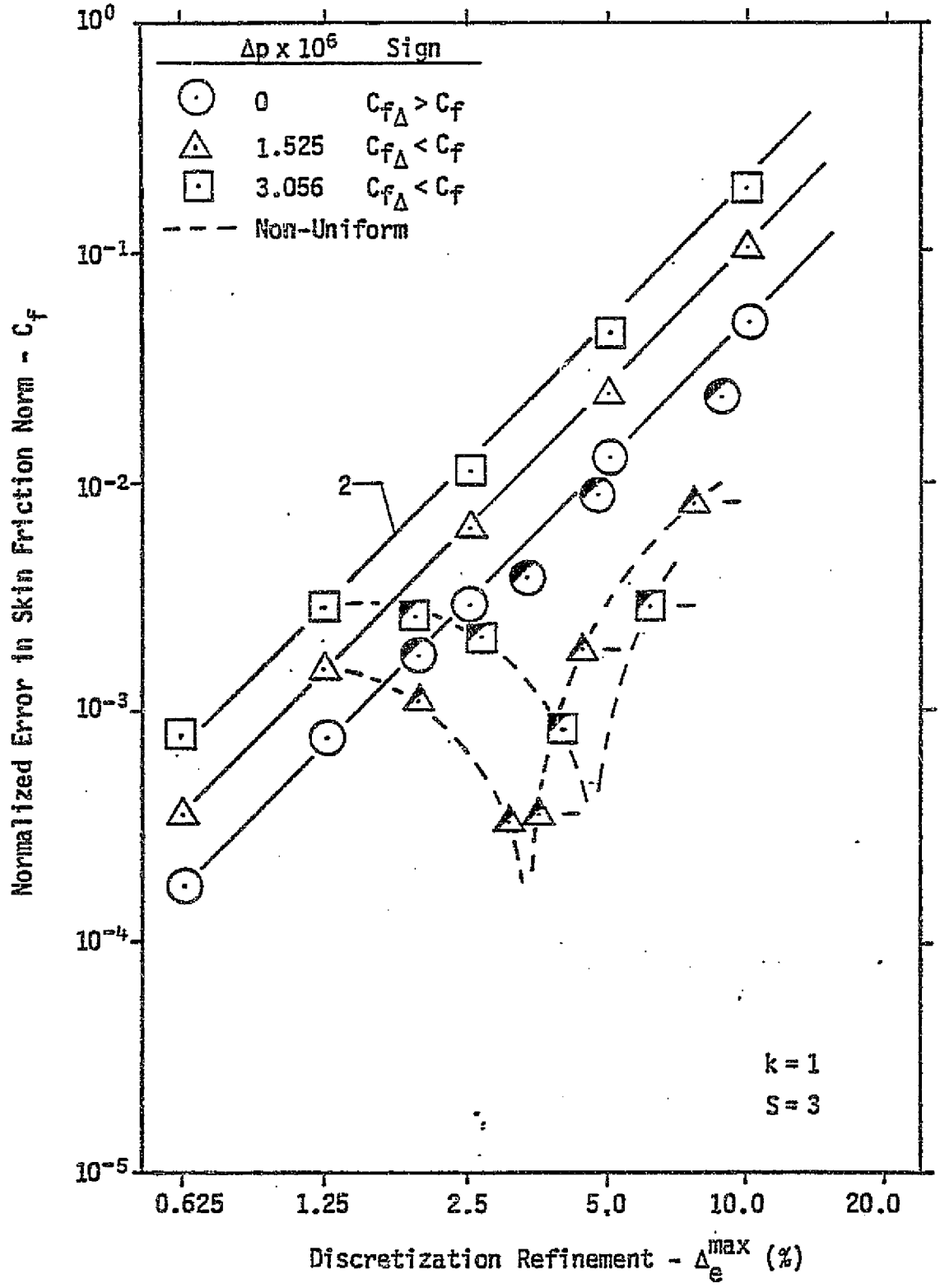

Figure 26. Accuracy and Convergence with Discretization Refinement in Skin Friction Norm, Laminar Boundary Layer with Pressure Gradient, Linear Elements, Finite Difference Initial-Value Matrix

ORIGINAL PAGE IS
OF POOR QUALITY

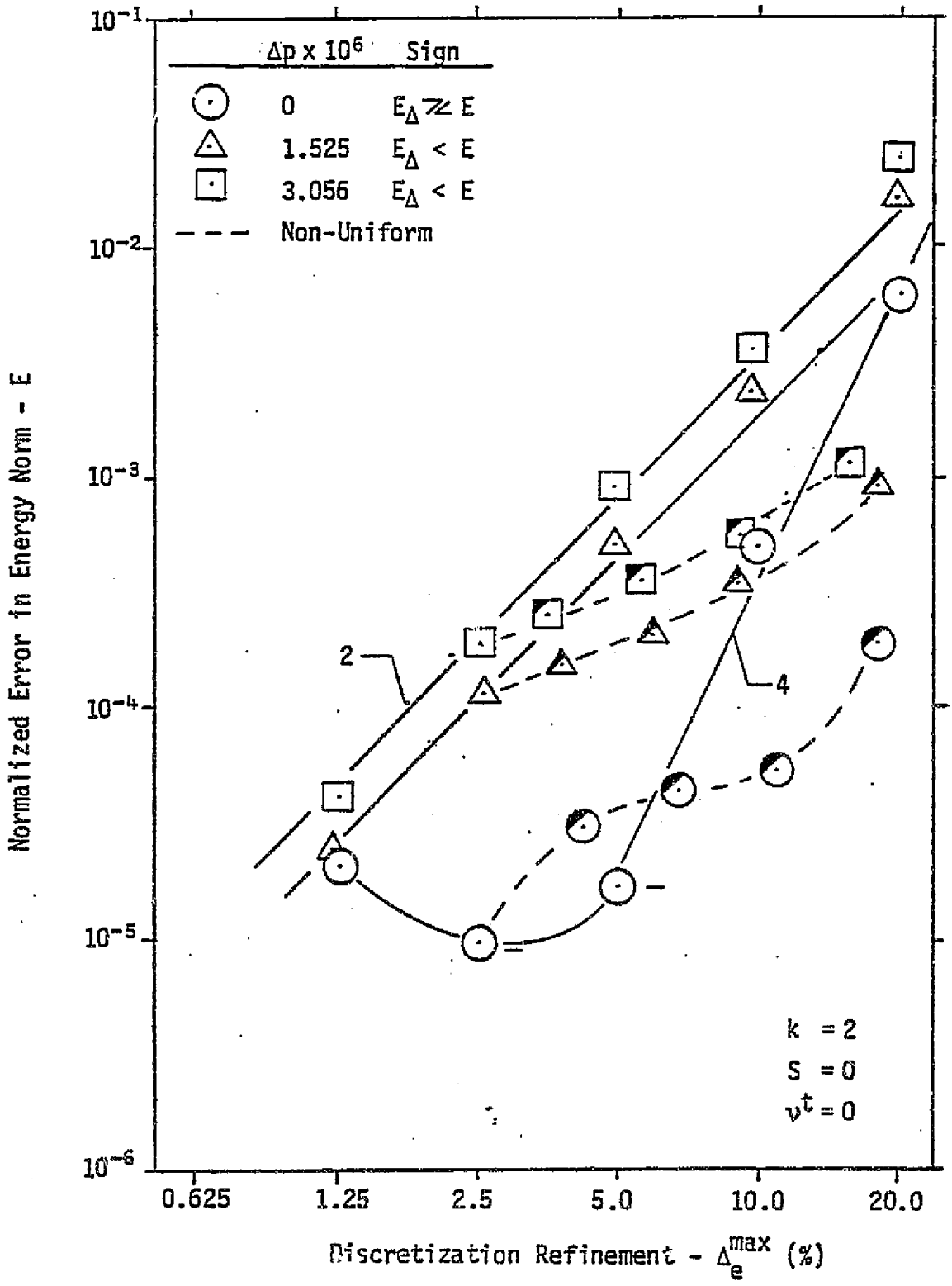

Figure 27. Accuracy and Convergence with Discretization Refinement in Energy Norm, Laminar Boundary Layer with Pressure Gradient, Quadratic Finite Elements

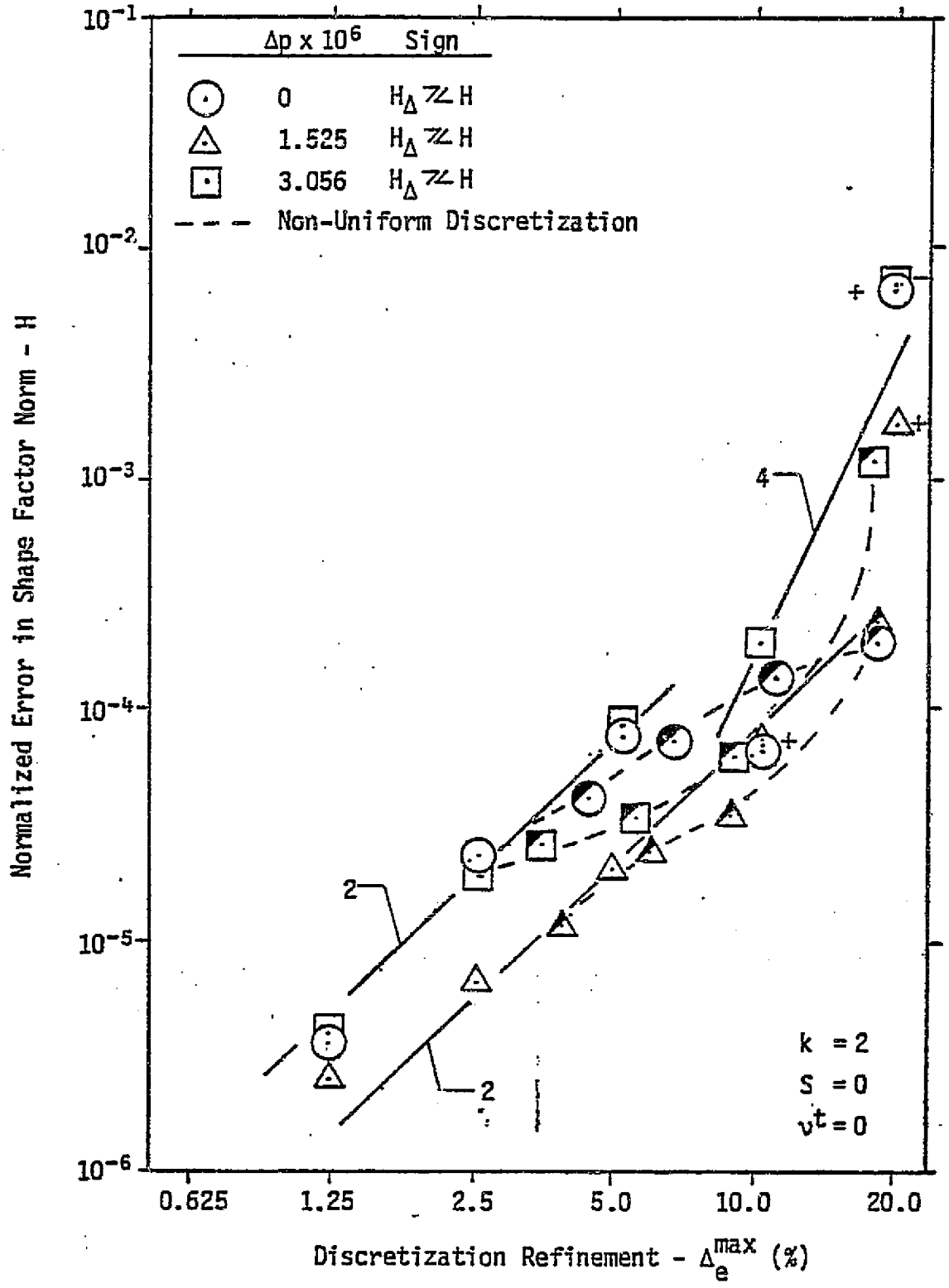

Figure 28. Accuracy and Convergence with Discretization Refinement in Shape Factor Norm, Laminar Boundary Layer with Pressure Gradient, Quadratic Finite Elements

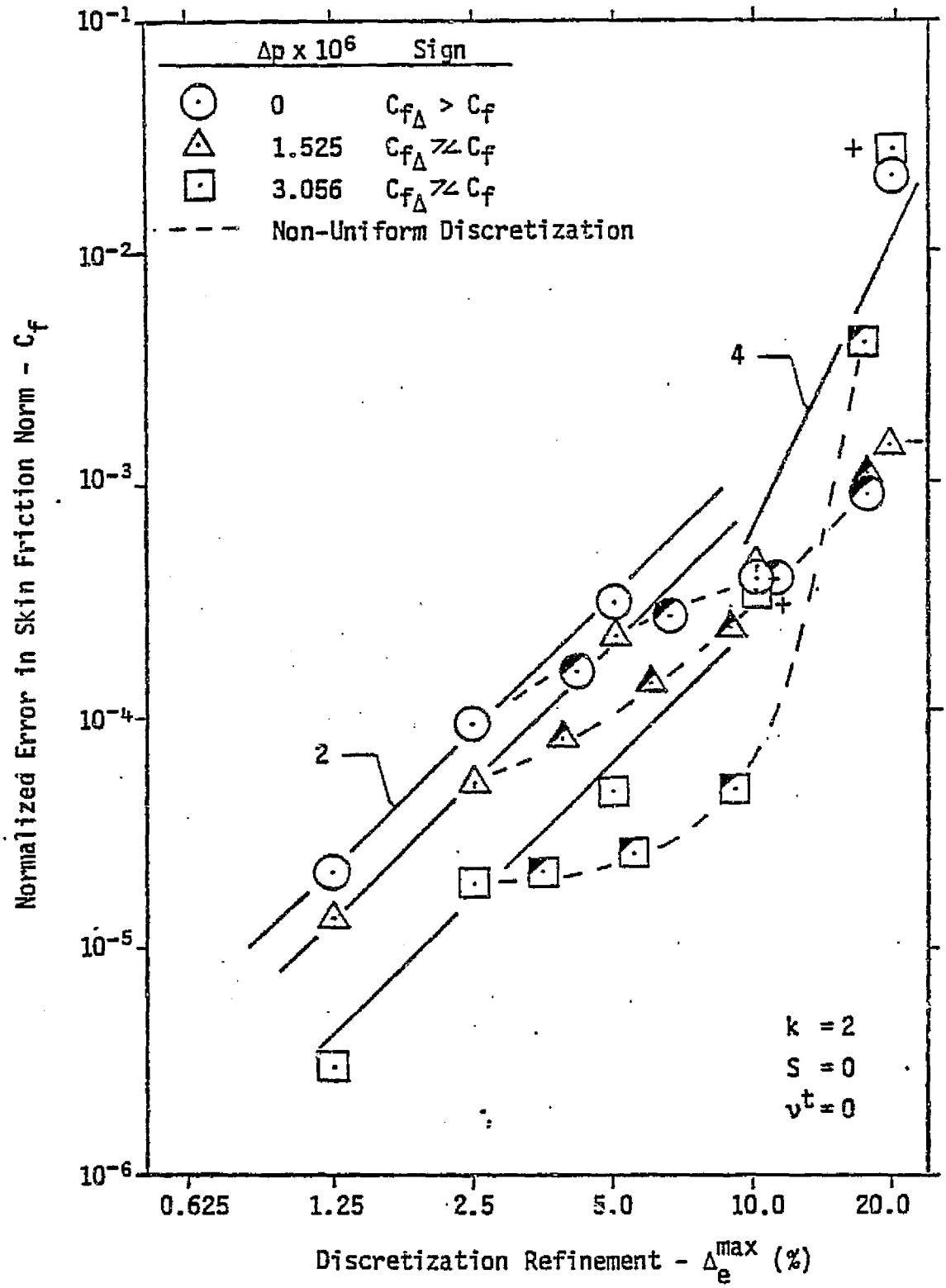

Figure 29. Accuracy and Convergence with Discretization Refinement in Skin Friction Norm, Laminar Boundary Layer with Pressure Gradient, Quadratic Finite Elements

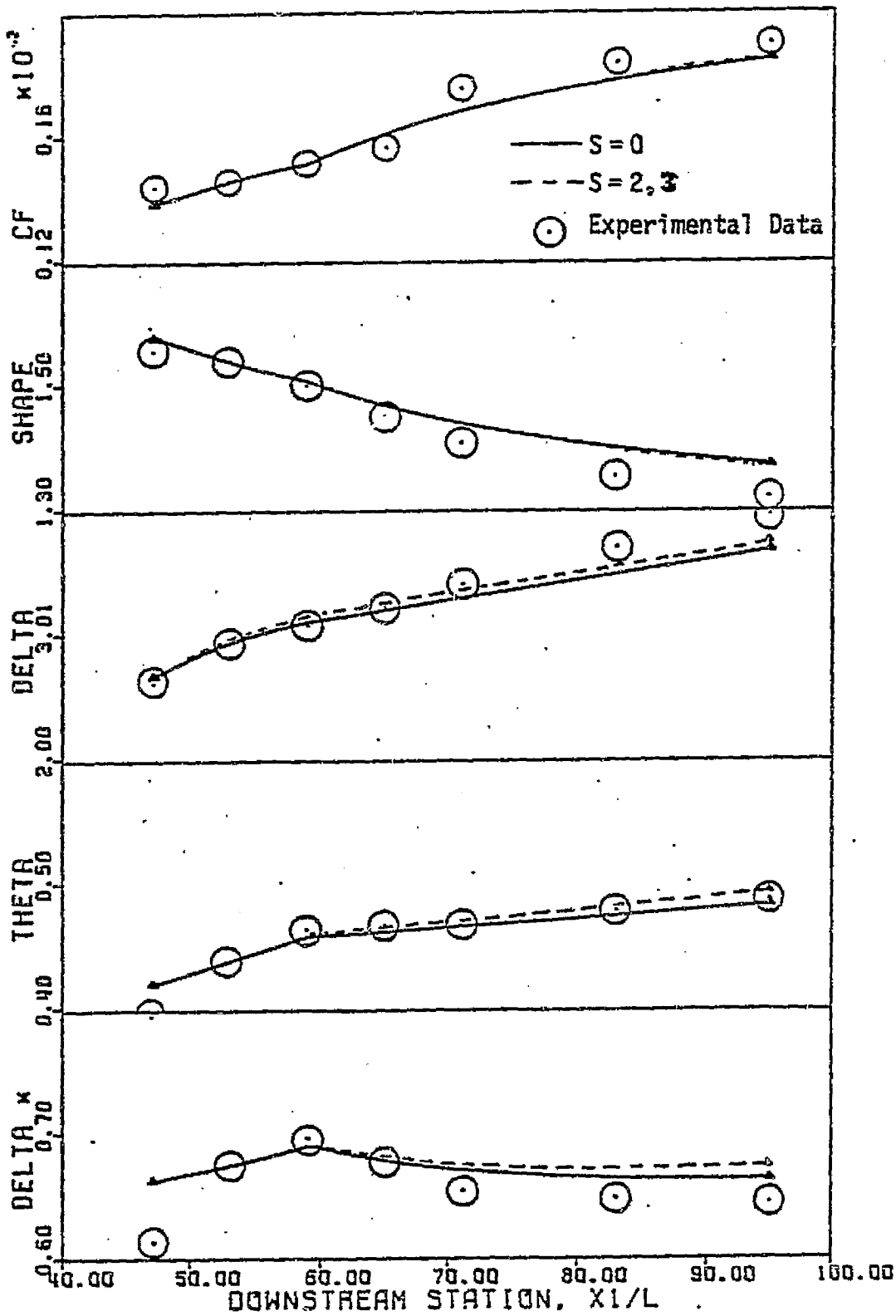

Figure 30. Computed and Experimental Boundary Layer Parameters, Bradshaw Relaxing Flow, Linear Elements, MLT Closure

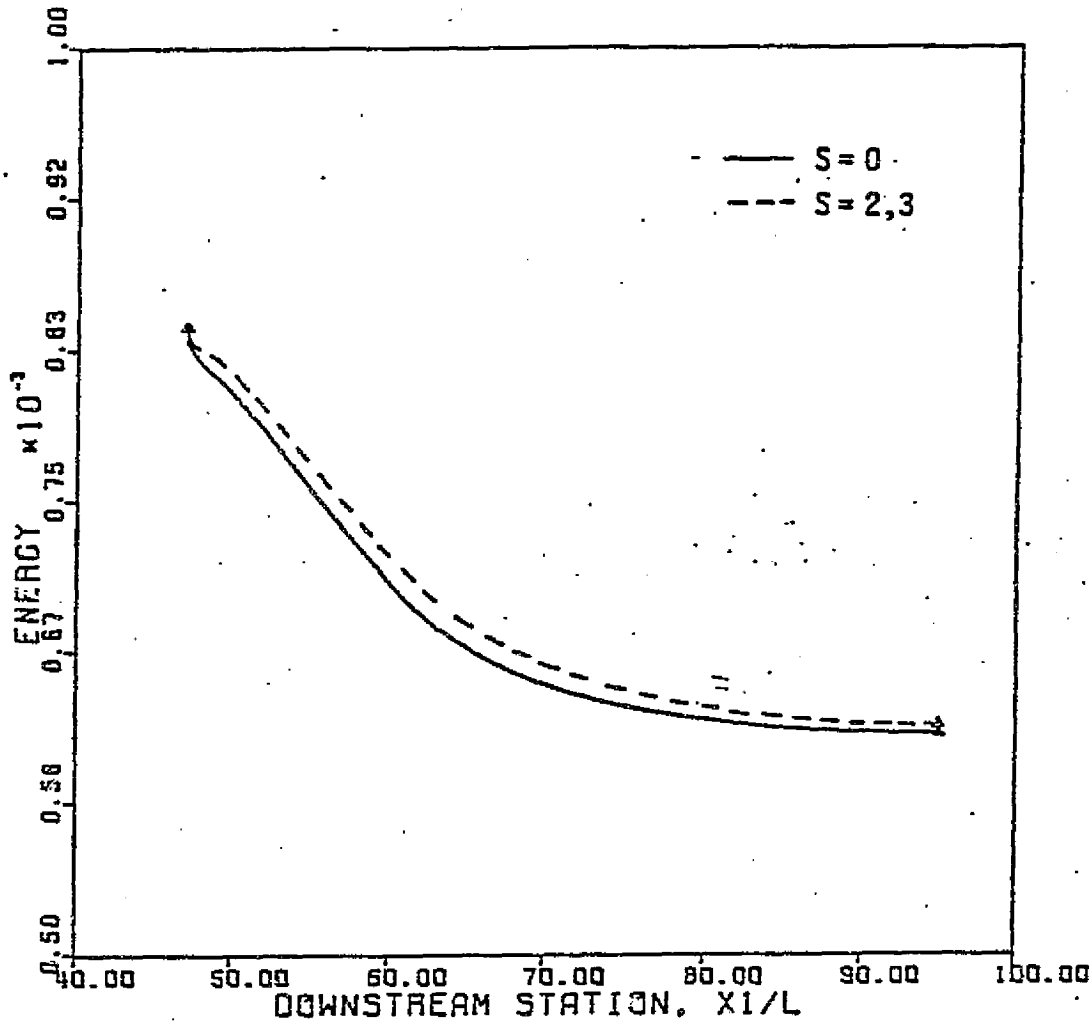

Figure 31. Finite Element Solution Energy, Bradshaw Relaxing Flow, Linear Elements, MLT Closure

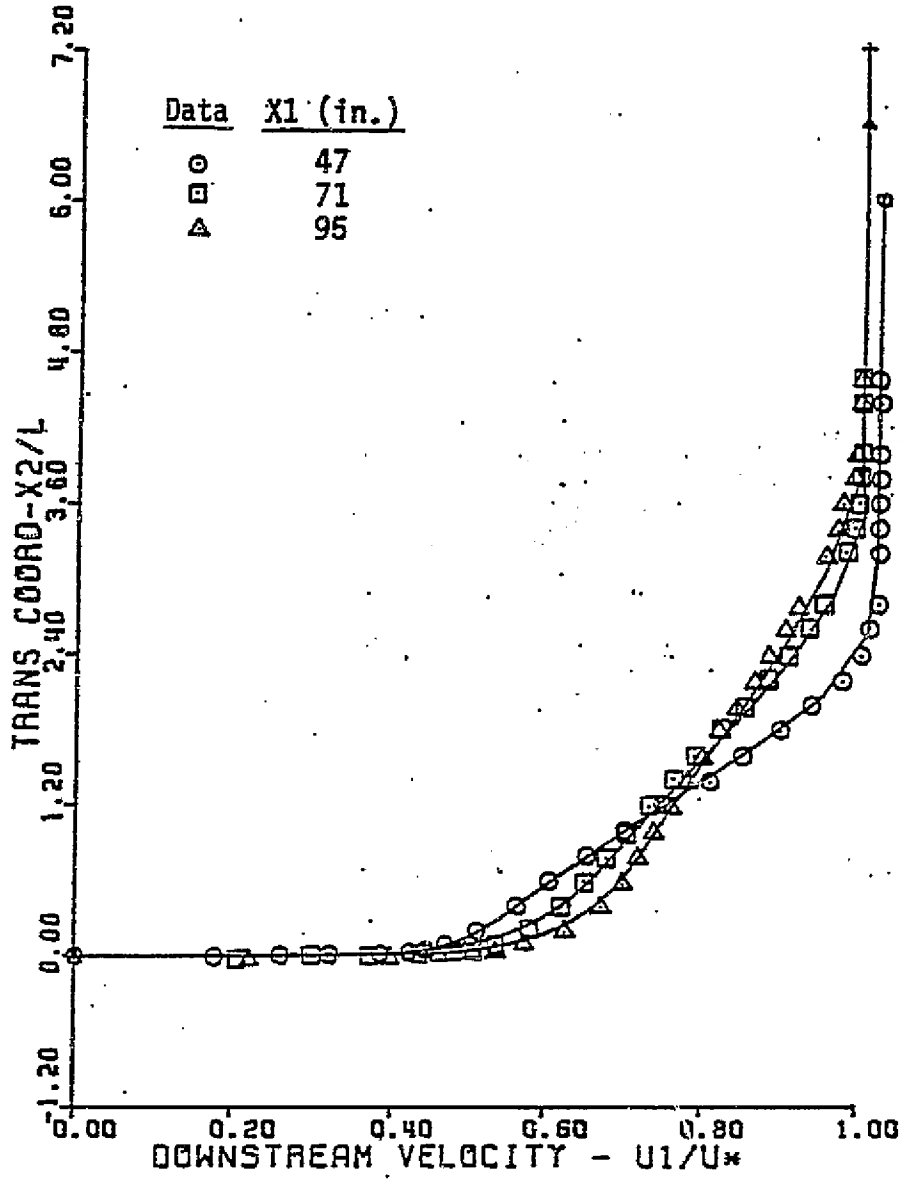

Figure 32. Longitudinal Velocity Profiles, Bradshaw Relaxing Flow, Linear Finite Elements, MLT

ORIGINAL PAGE IS
OF POOR QUALITY

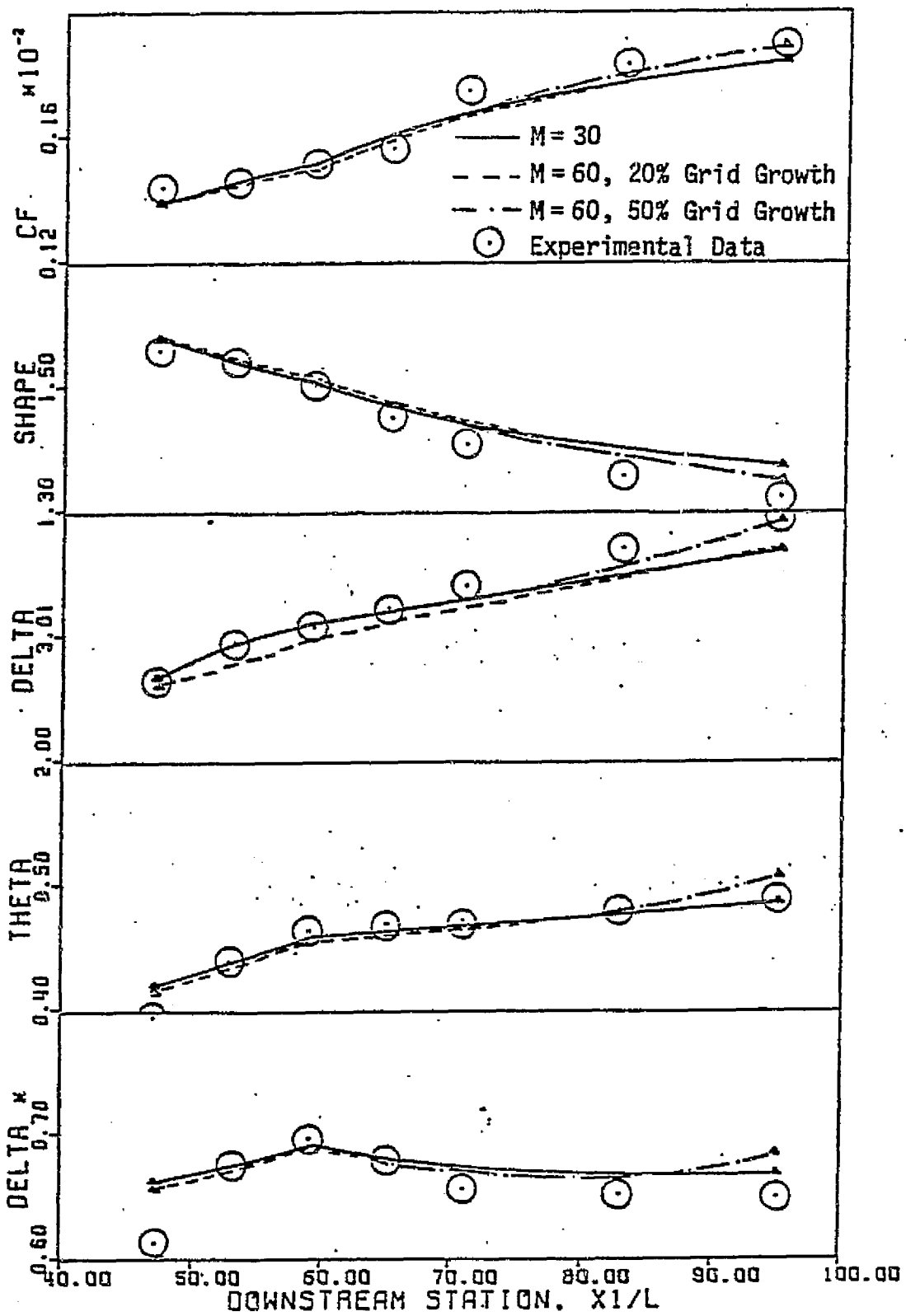

Figure 33. Boundary Layer Parameters, Bradshaw Relaxing Flow, Linear Elements, Consistent Assembly, MLT Closure

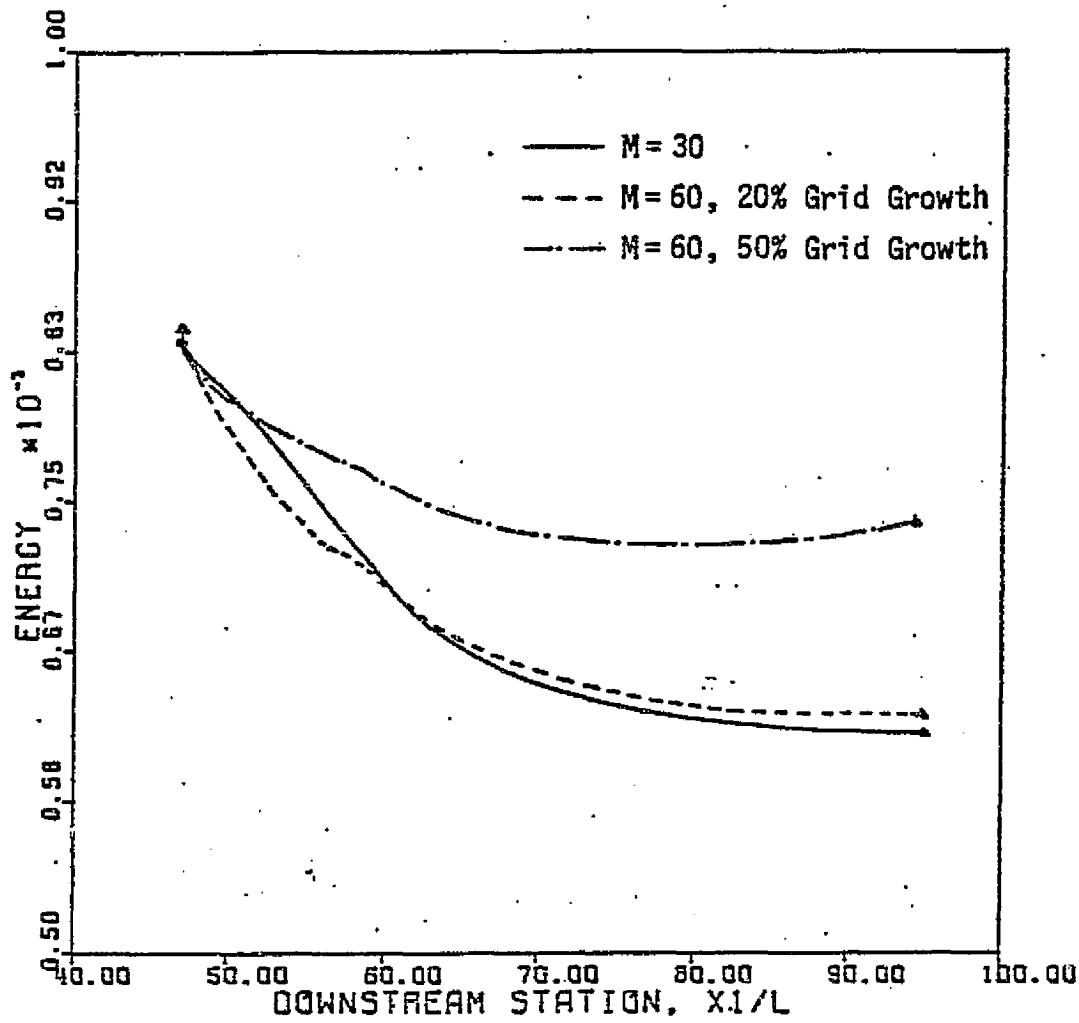

Figure 34. Finite Element Solution Energy, Bradshaw Relaxing Flow, Linear Elements, Consistent Assembly, MLT Closure

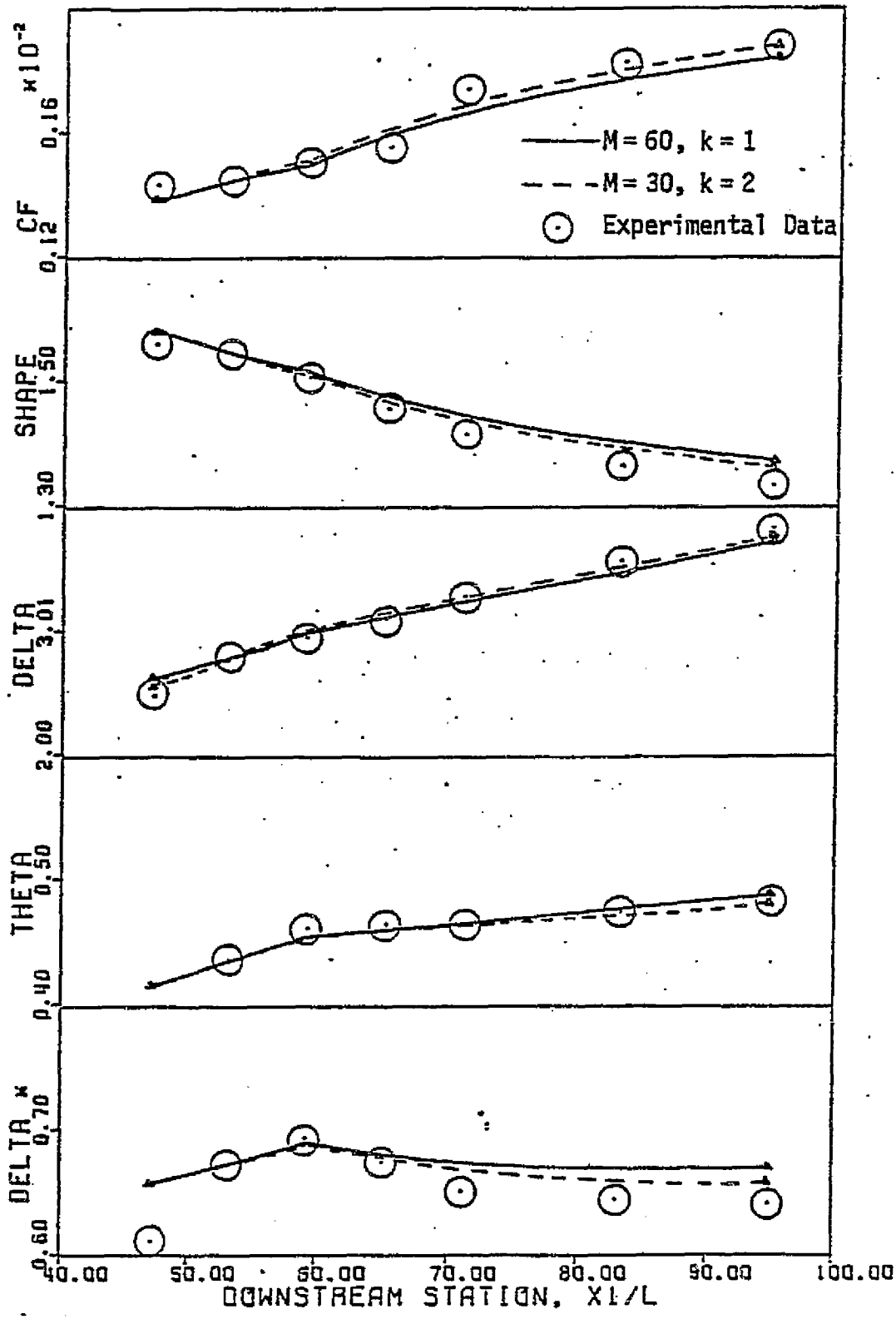

Figure 35. Boundary Layer Parameters, Bradshaw Relaxing Flow, Linear and Quadratic Elements, Consistent Assembly, MLT Closure

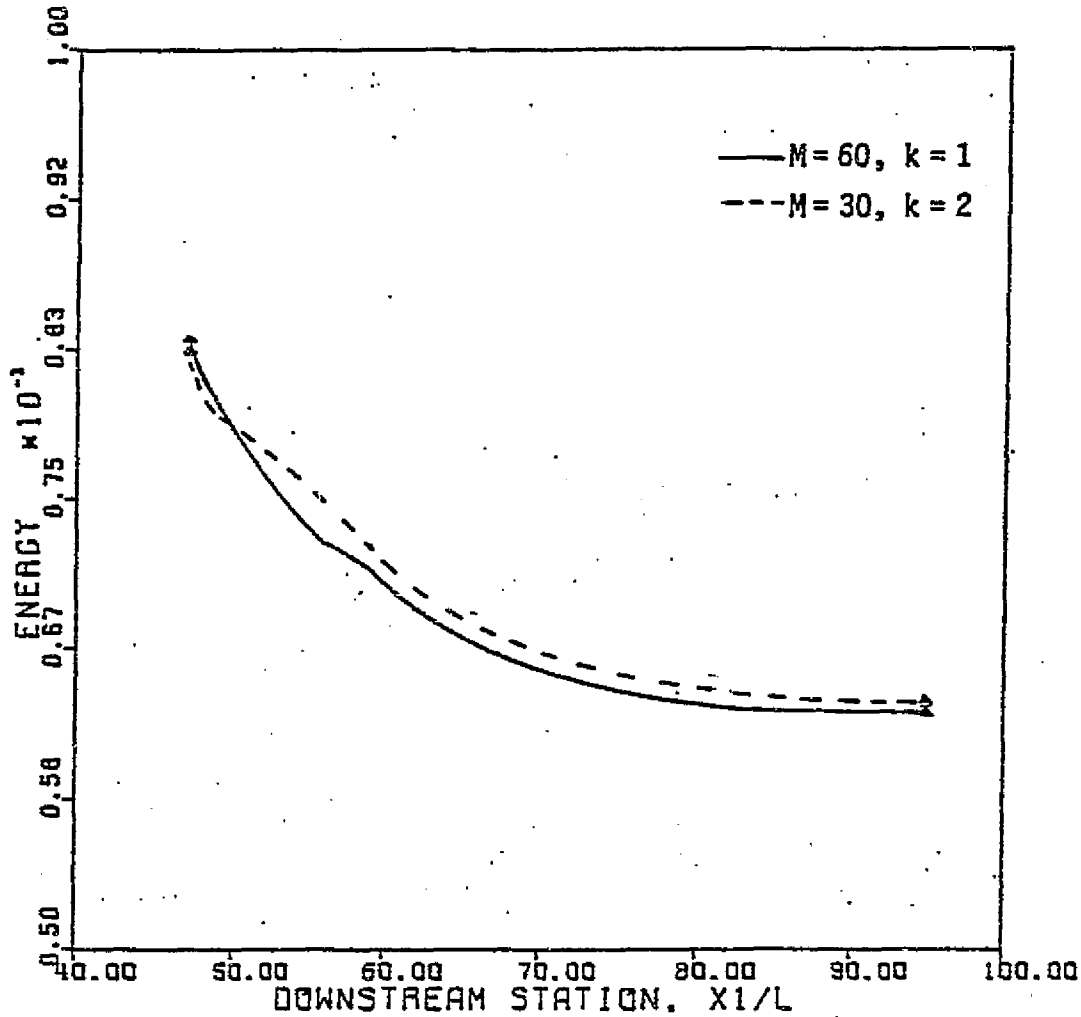

Figure 36. Finite Element Solution Energy, Bradshaw Relaxing Flow, Linear and Quadratic Elements, Consistent Assembly, MLT Closure

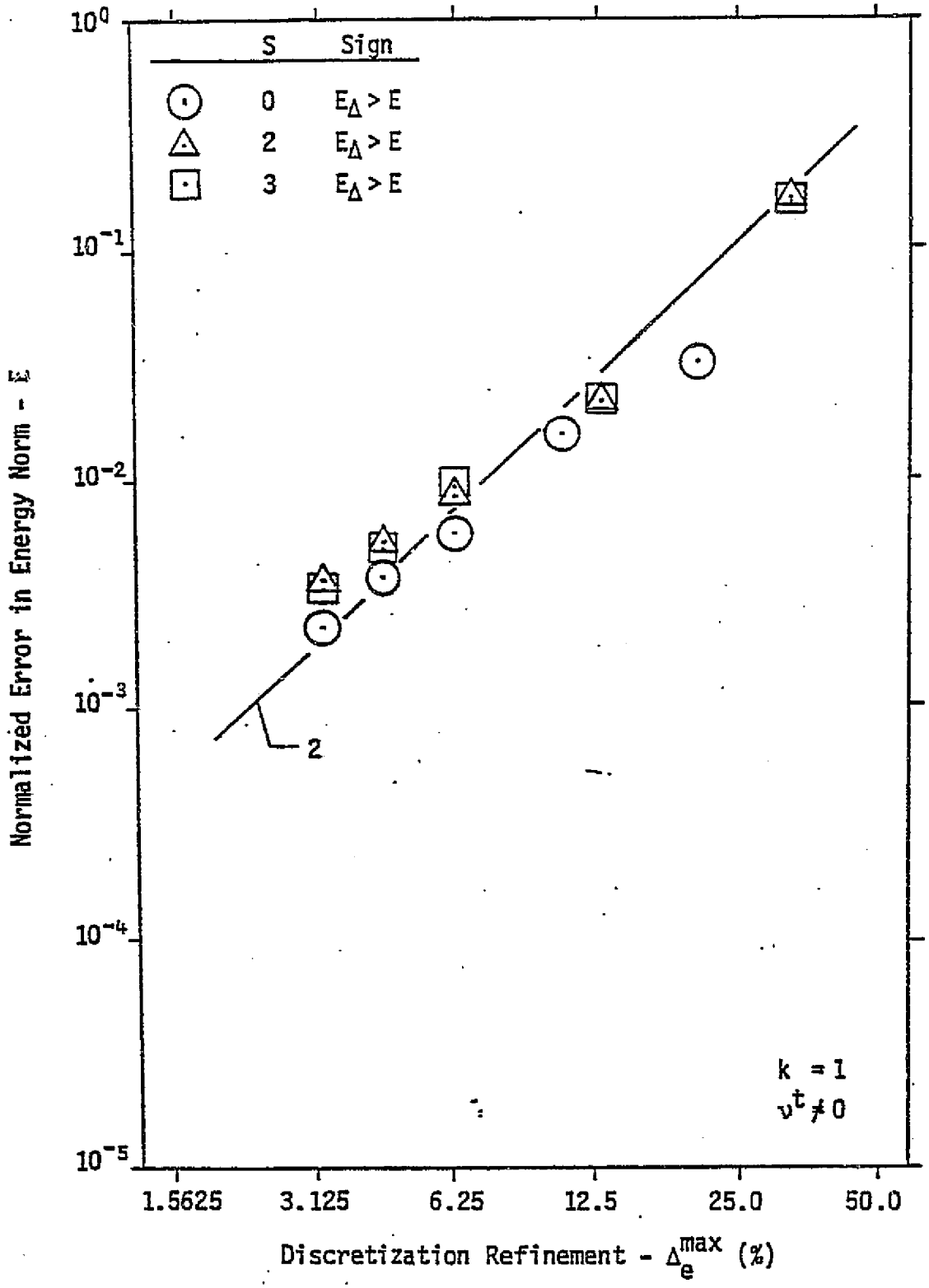

Figure 37. Accuracy and Convergence with Discretization Refinement in Energy Norm, Wieghardt Flat Plate Flow, Linear Elements, MLT Closure

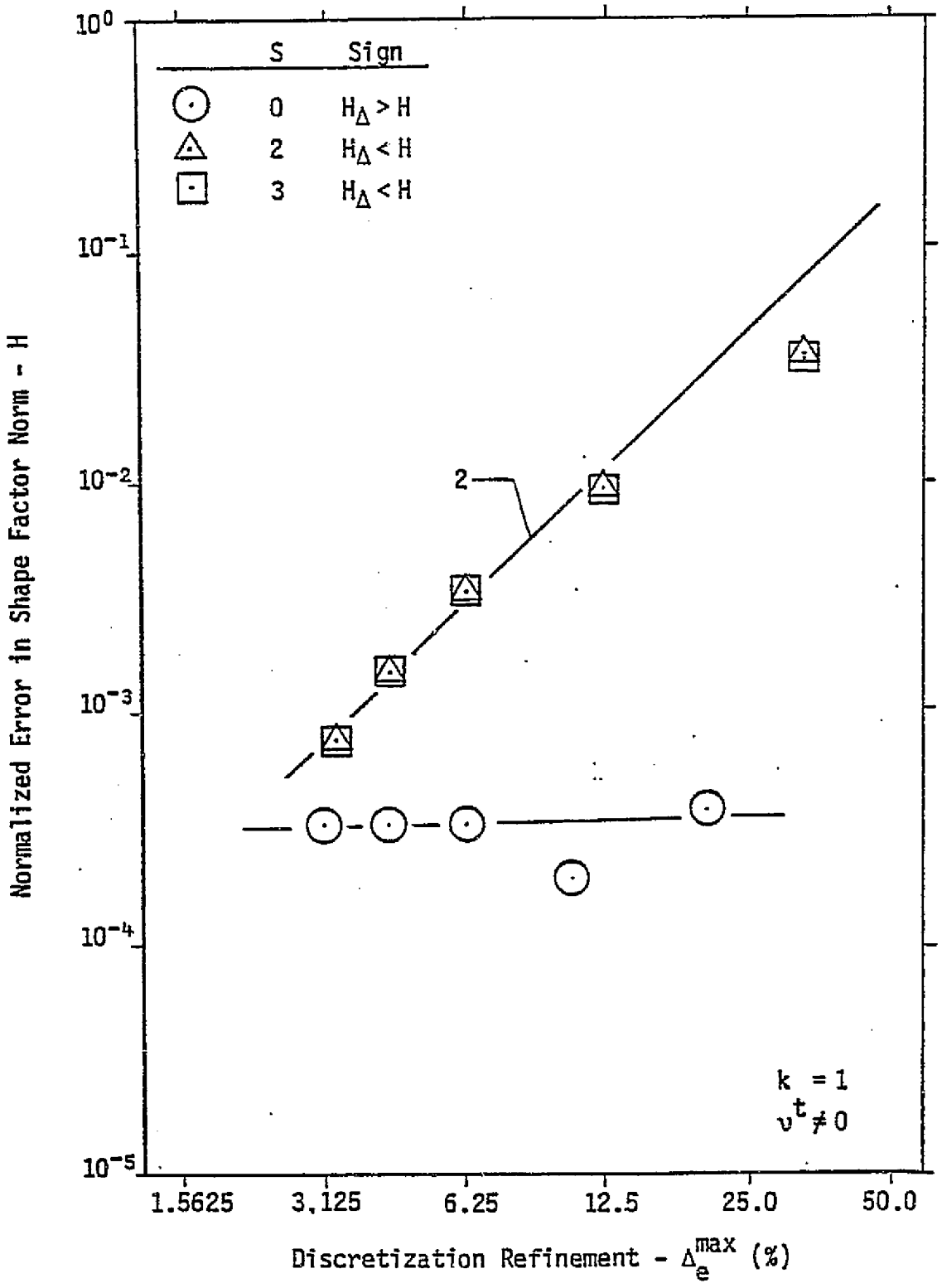

Figure 38. Accuracy and Convergence with Discretization Refinement in Shape Factor Norm, Wieghardt Flat Plate Flow, Linear Elements, MLT Closure

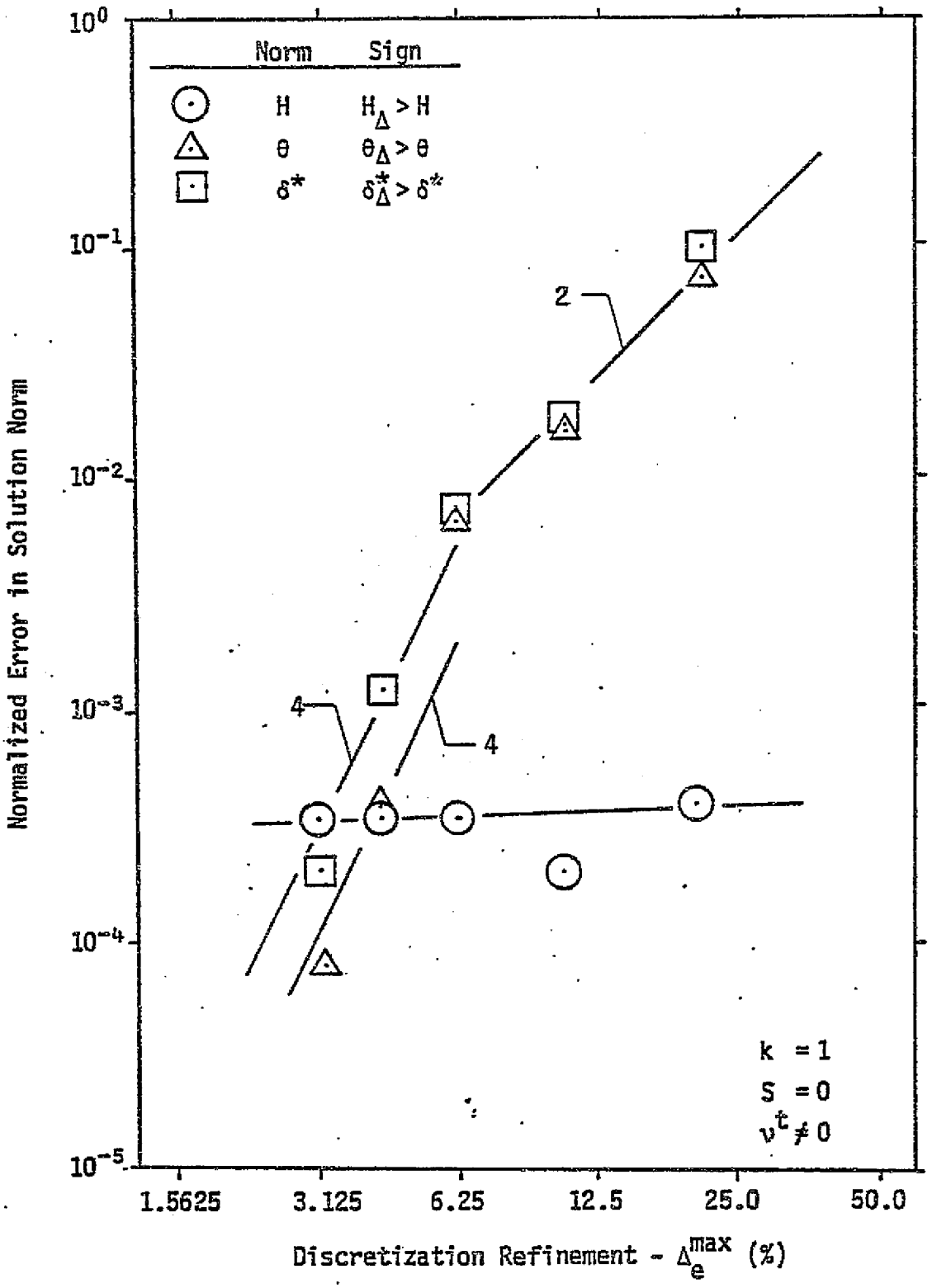

Figure 39. Accuracy and Convergence with Discretization Refinement in Shape Factor, Momentum Thickness and Displacement Thickness Norms, Wieghardt Flat Plate Flow, Linear Elements, MLT Closure

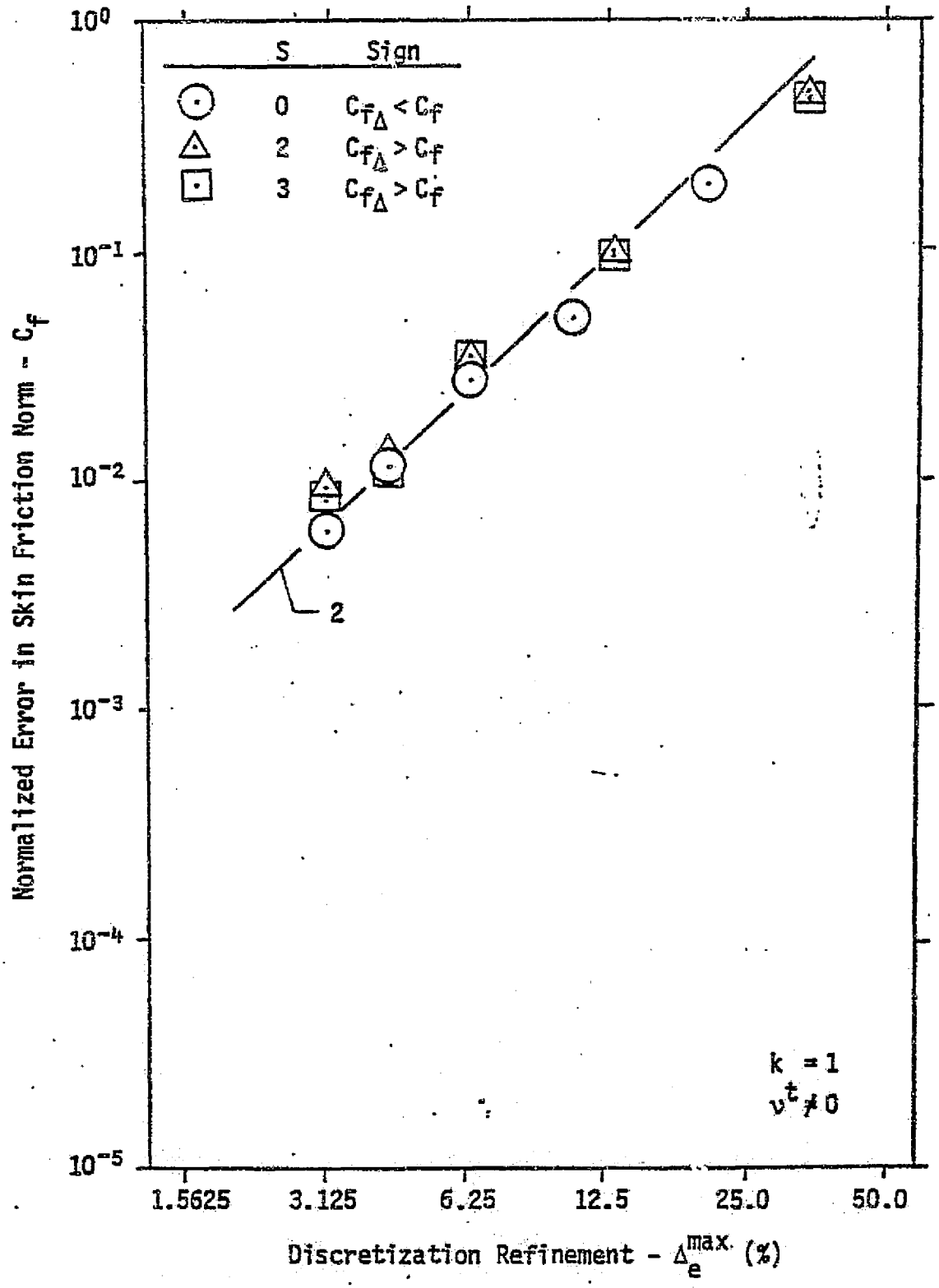

Figure 40. Accuracy and Convergence with Discretization Refinement in the Skin Friction Norm, Wieghardt Flat Plate Flow, Linear Elements, MLT Closure

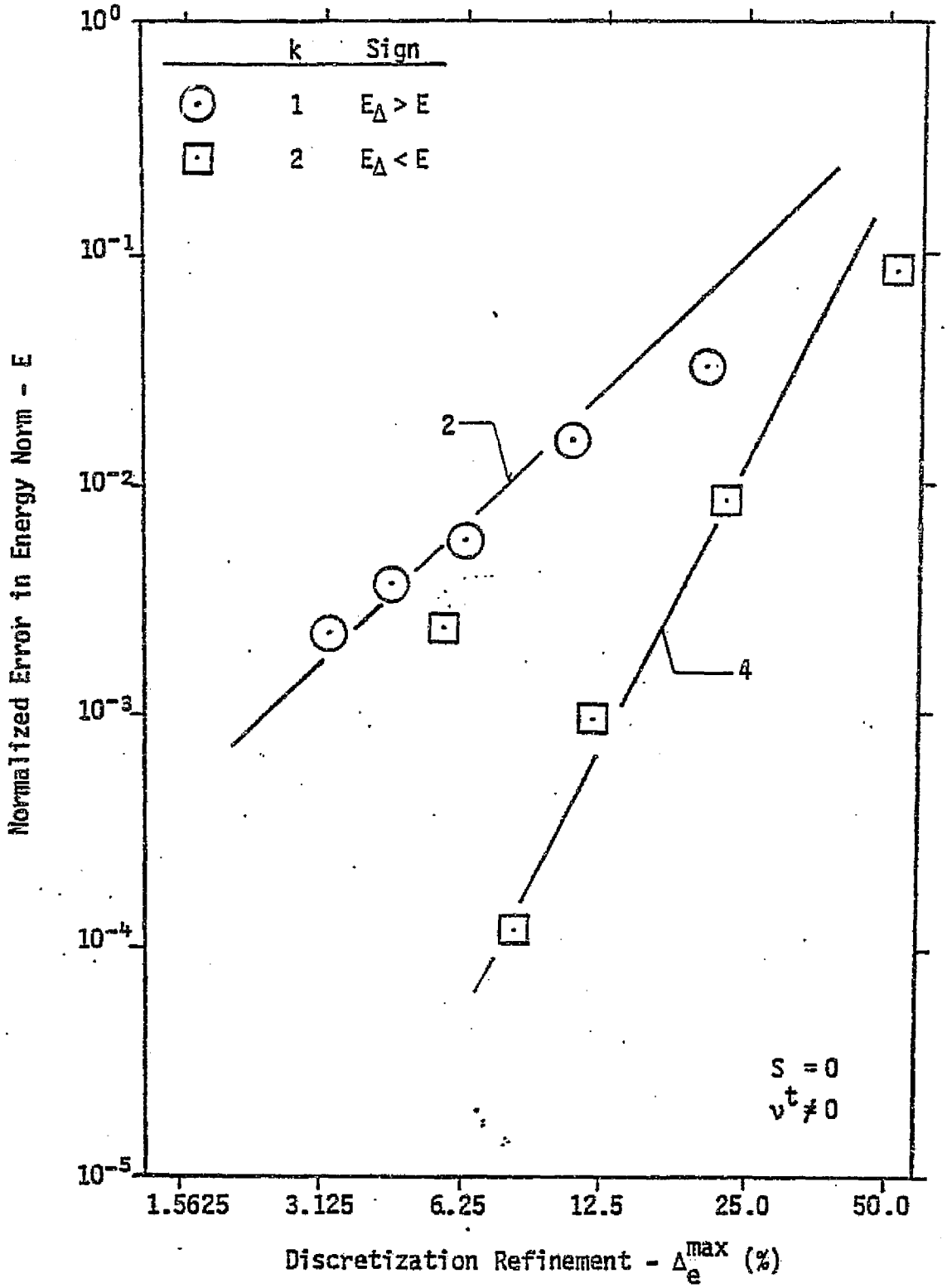

Figure 41. Accuracy and Convergence with Discretization Refinement in Energy Norm, Wieghardt Flat Plate Flow, Linear and Quadratic Elements, Consistent Assembly, MLT Closure

ORIGINAL PAGE IS
OF POOR QUALITY

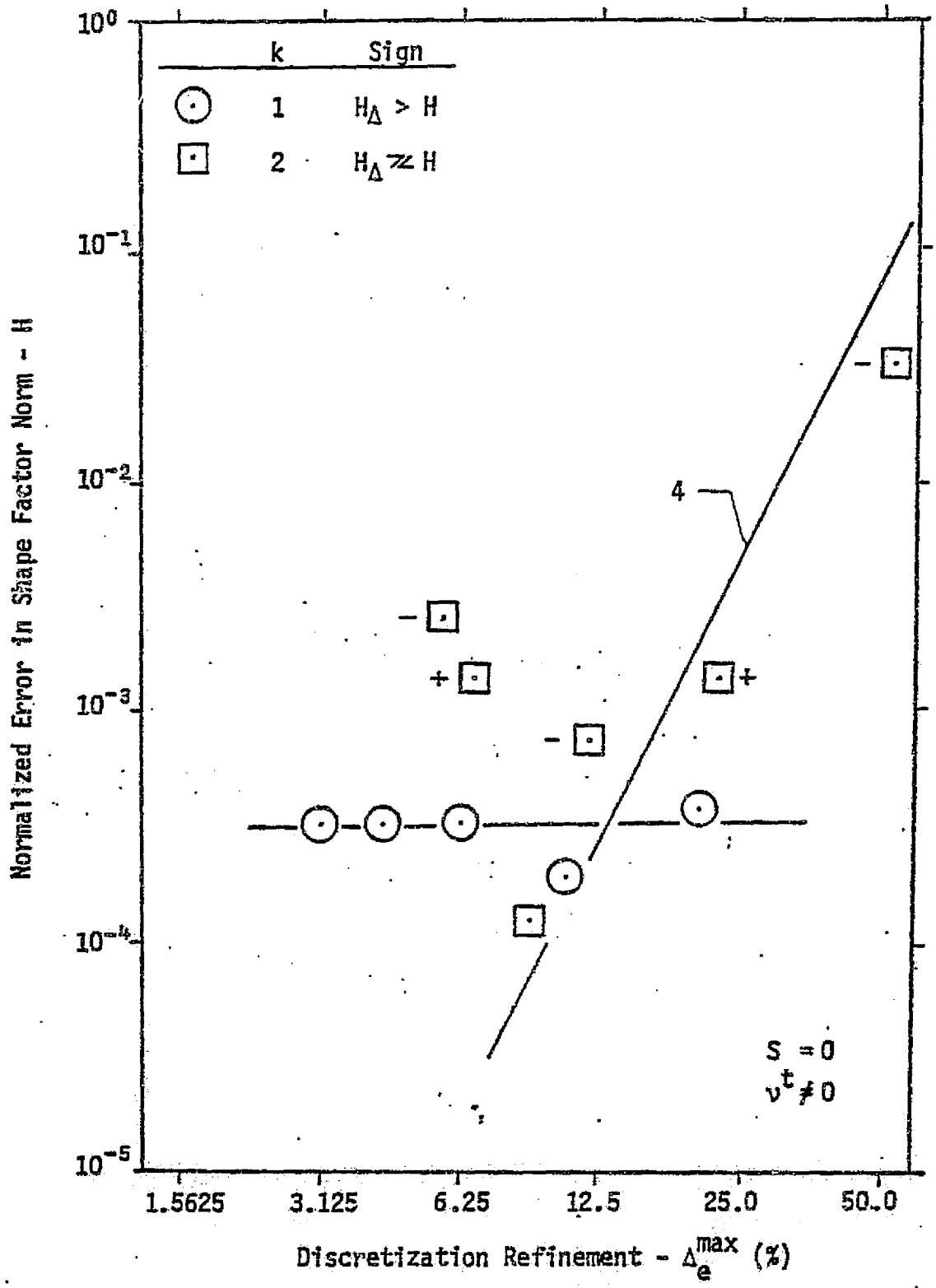

Figure 42. Accuracy and Convergence with Discretization Refinement in Shape Factor Norm, Wieghardt Flat Plate Flow, Linear and Quadratic Elements, Consistent Assembly, MLT Closure

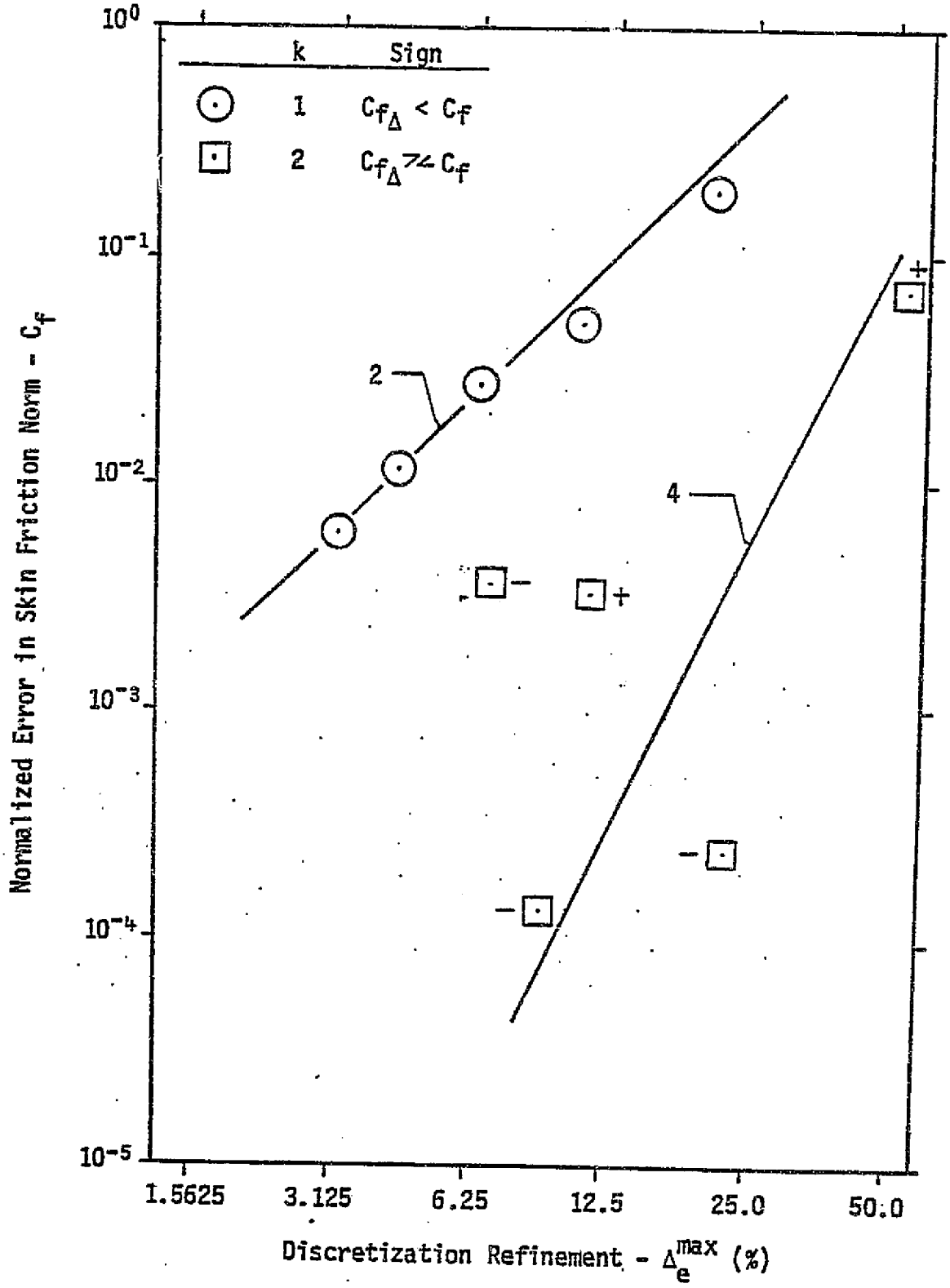

Figure 43. Accuracy and Convergence with Discretization Refinement in the Skin Friction Norm, Wieghardt Flat Plate Flow, Linear and Quadratic Elements, MLT Closure

ORIGINAL PAGE IS
OF POOR QUALITY

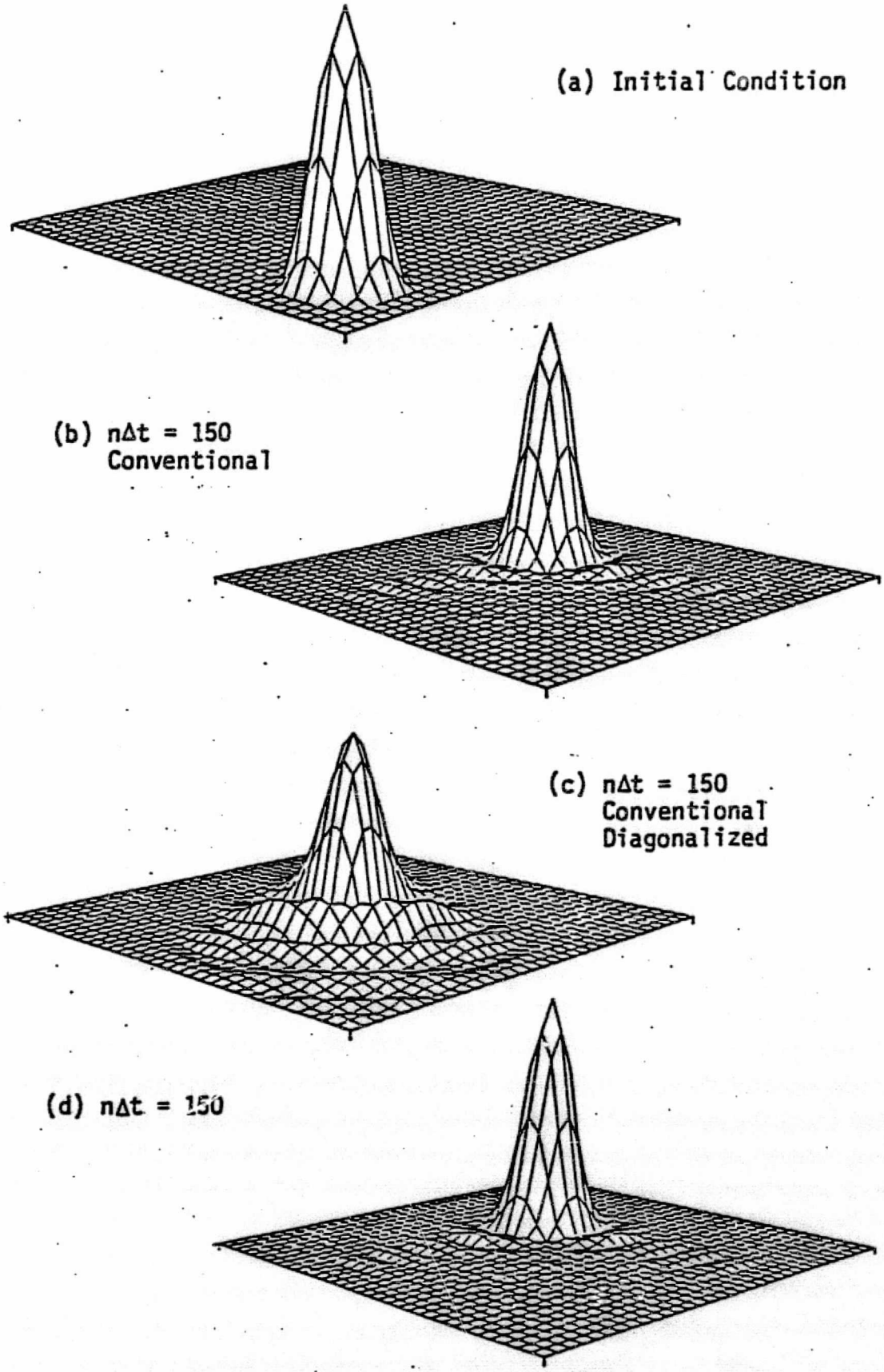

Figure 44. Advection of a Concentration Packet in Constant Velocity Field $\vec{U}_1$, C = 0.1

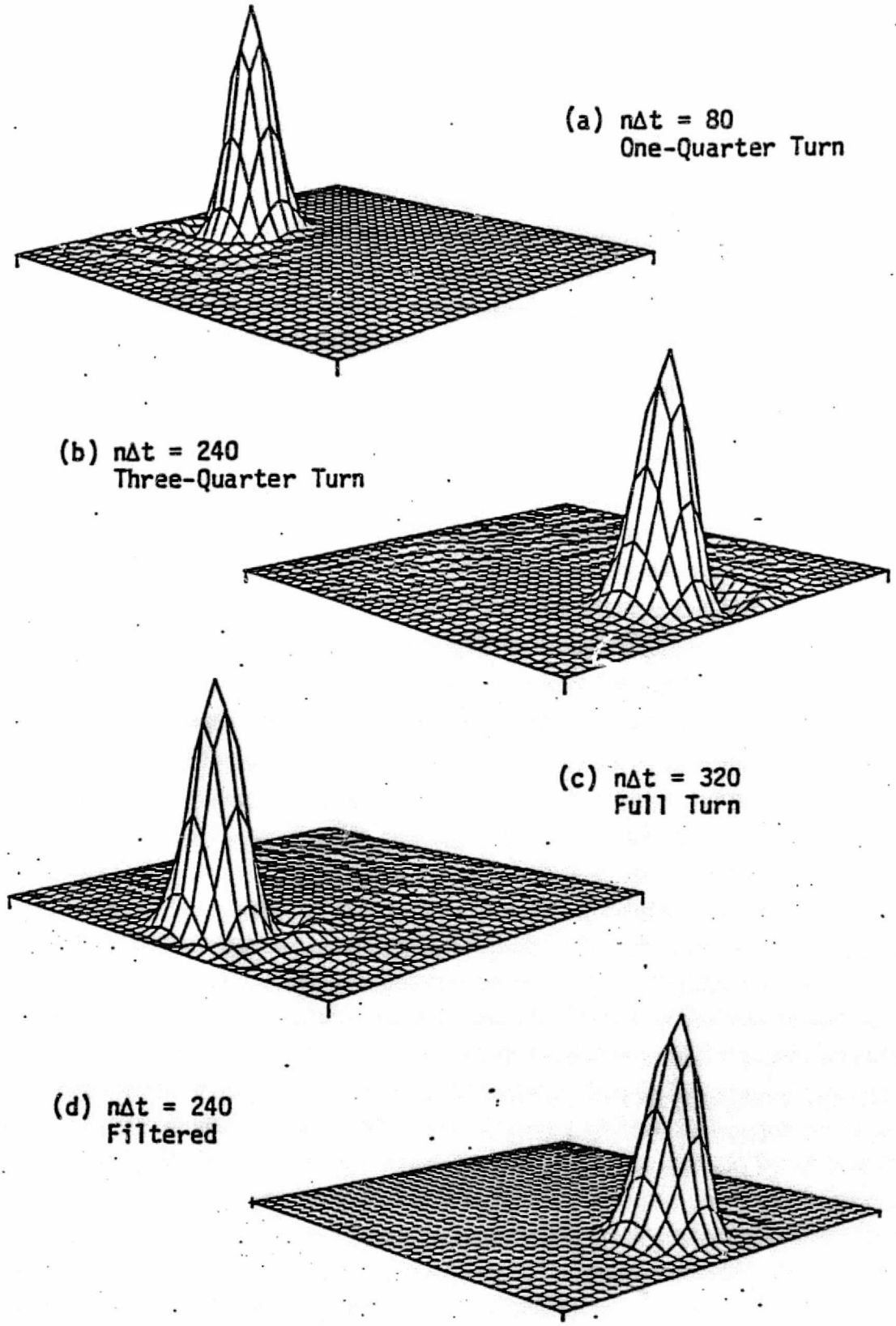

Figure 45. Advection of a Concentration Packet in Solid-Body Rotation Velocity Field $\vec{U}_2$, C = 0.1

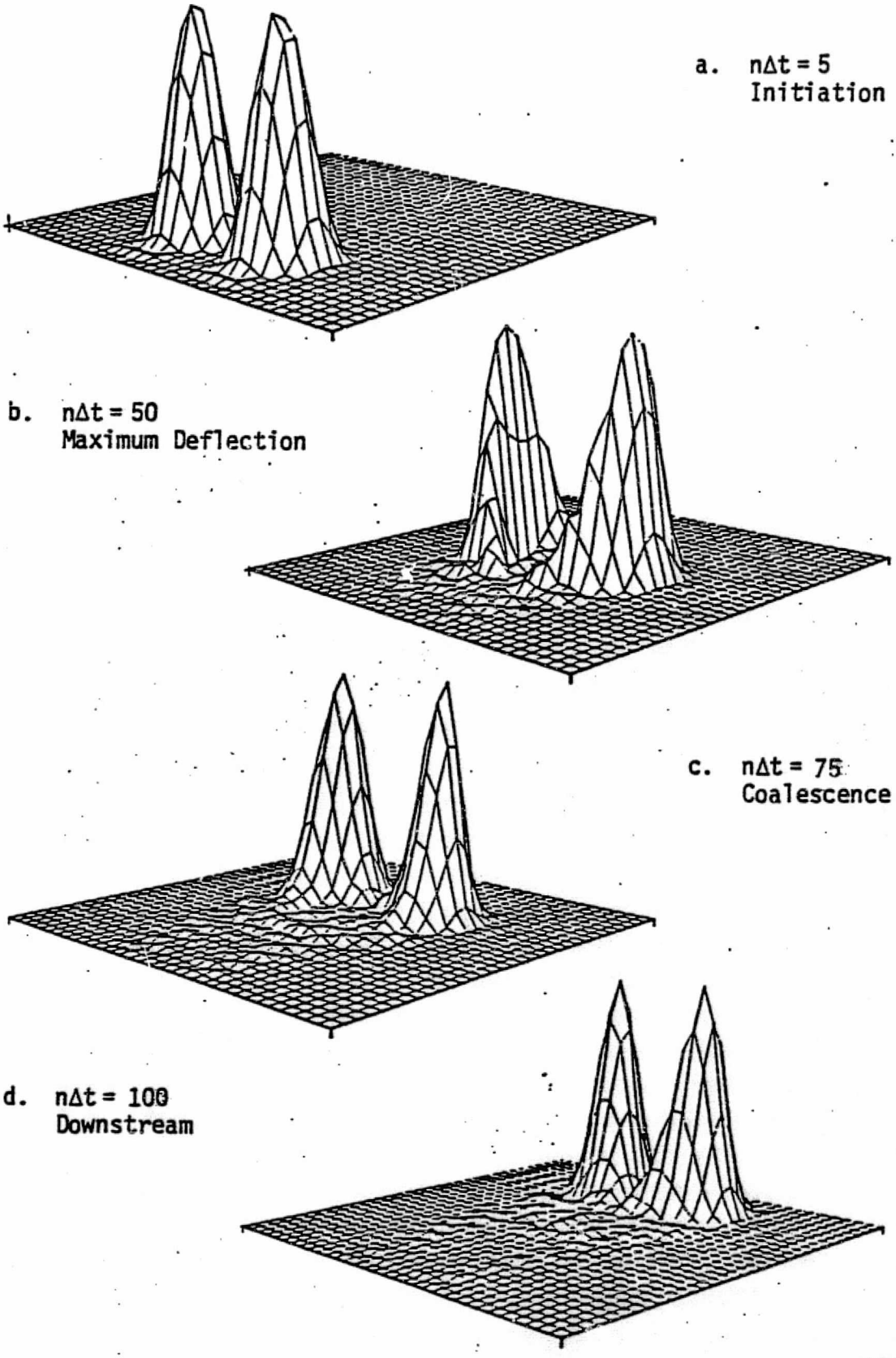

Figure 46. Advection of a Concentration Packet Pair in Irrotational Velocity Field $\bar{U}_3$, C = 0.1

ORIGINAL PAGE IS
OF POOR QUALITY

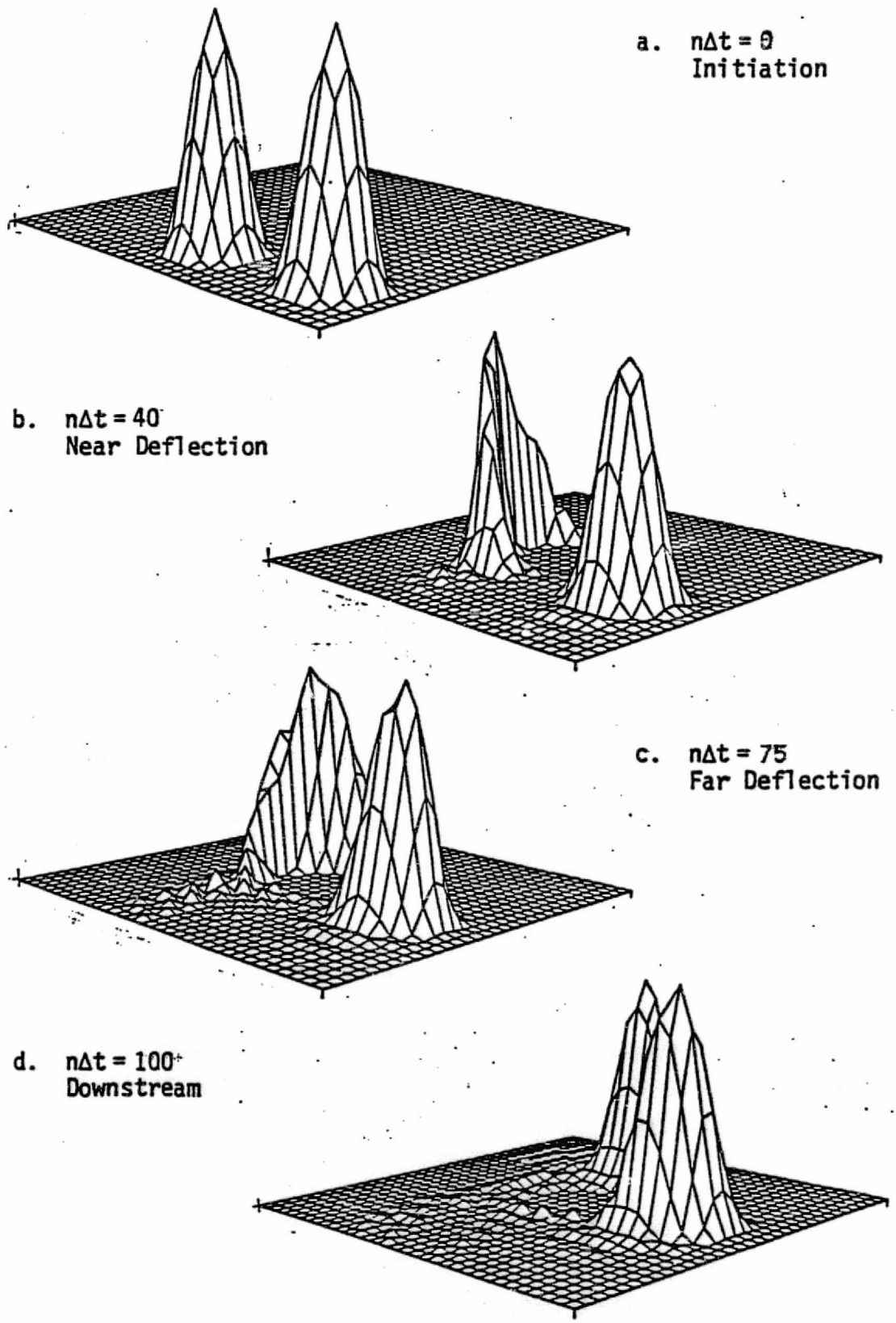

Figure 47. Advection of a Concentration Packet Pair in Irrotational Velocity Field $\vec{U}_4$ with Circulation, C = 0.1